

Colloidal Rods in Confinement

Kira E. Klop

Christ Church College
University of Oxford

Supervisors: Professor Dirk G. A. L. Aarts and
Professor Julia M. Yeomans

A thesis submitted for the degree of
Doctor of Philosophy

Trinity Term 2016

Abstract

We study colloidal rods in confinement and under flow on the single particle level using optical microscopy and laser scanning confocal microscopy. First, we investigate liquid crystals in confinement. A mathematical method for calculating distortion energies is developed and illustrated by applying it to both artificial data and experimental results. Next, we study an isotropic phase in strong confinement, and observe a capillary nematisation transition. This is the first observation of capillary nematisation in a colloidal liquid crystal. The results are compared to the Zwanzig model and a DFT model for semi-flexible rods, and we find good agreement with both. The DFT model, in which rod orientations are unrestricted and rod flexibility is taken into account, was found to have a better quantitative agreement with the experiments. In the second half of this thesis, we study single colloidal rods flowing in a plane Poiseuille flow. For the most simple case of non-magnetic Brownian rods in water, we observe aperiodic kayaking and xy-tumbling behaviour. The results are compared to Jeffery theory for non-Brownian rods in a simple shear flow and to multi-particle collision dynamics simulations. The experimental results were found to undergo the same type of behaviour as predicted by Jeffery's theory, but without periodicity, and particles were seen to switch from one type of behaviour to another. We find qualitative agreement between the experiment and simulations, which indicates that the presence of Brownian motion can explain the differences between theory and experiment. Following on, we investigate further deviations from Jeffery theory by studying the effect of an external magnetic field and of a non-Newtonian fluid on the orientational behaviour of rods. We find that a magnetic field shows somewhat similar behaviour as the kayaking and tumbling found in the non-magnetic system, but suppressed towards a plane perpendicular to the magnetic field. Rods flowing through a non-Newtonian fluid are found to be aligned in the direction of flow, and do not undergo any tumbling behaviour. The absence of tumbling can be explained by the depletion interaction between rods and the wall. It is unclear why the preferred orientation for rods is along the direction of flow.

Declaration

This thesis is submitted for the degree of Doctor of Philosophy in Physical and Theoretical Chemistry at the University of Oxford. No part of this thesis has been accepted or is currently being submitted for any degree, diploma, certificate or other qualification in this University or elsewhere. This thesis is wholly my own work, except where indicated.

Contents

Abstract **i**

Declaration **iii**

1 General introduction **1**

1.1 Colloids 1

1.2 Liquid Crystals 2

1.2.1 Isotropic-Nematic phase transition 3

1.2.2 Nematic liquid crystals 6

1.3 Confinement 8

1.4 Flow in confinement 10

1.5 Thesis outline 12

2 System and experimental methods **13**

2.1 Colloidal rods 14

2.1.1 *fd*-virus 14

2.1.2 Silica rods 15

2.2 Soft lithography 15

2.2.1 Polydimethylsiloxane (PDMS) 18

2.2.2 UV-glue 18

2.3 Microscopy 19

2.3.1 Resolution 20

2.4 Magnetic set-up 22
2.5 Image Analysis 24
2.5.1 Particle detection 24
2.5.2 Particle tracking 25
2.5.3 Orientations 26
2.6 Conclusion 27

3 Direct calculation of distortion energies in colloidal liquid crystals from single-particle data 29

3.1 Introduction 30
3.2 Method 30
3.3 Artificial data 35
3.4 Application to experimental data 38
3.5 Conclusion 40

4 Capillary nematisation of colloidal rods in confinement 43

4.1 Introduction 44
4.2 Experiment and results 45
4.2.1 Grand-canonical system 47
4.2.2 Canonical system 50
4.3 Zwanzig model 51
4.4 Density Functional Theory 55
4.5 Conclusion 60

5 Orientational behaviour of silica rods in a Poiseuille flow 61

5.1 Introduction 62
5.2 Jeffery orbits 63
5.3 Experimental methods 67
5.4 Results 68

5.4.1 Orientation distributions 71
5.4.2 Velocity 73
5.5 Comparison to Jeffery theory 76
5.6 Simulations 77
5.7 Conclusion 79

6 Effects of a magnetic field and a non-Newtonian fluid 81
6.1 Introduction 82
6.2 Experiments 82
6.2.1 Magnetic field 82
6.2.2 Non-Newtonian fluid 84
6.3 Results and discussion 86
6.3.1 Magnetic field 86
6.3.2 Non-Newtonian fluid 87
6.4 Conclusion 91
Appendix: Calculation of the overlap volume 92

Summary 93

Bibliography 95

List of publications 107

Acknowledgments 109

Chapter 1

General introduction

1.1 Colloids

Suspensions of colloidal particles are abundant in everyday life. Examples include clay, paints, blood and micro-organisms, but also foods such as margarine and mayonnaise and everyday products such as toothpaste and shampoo. Studying the behaviour of colloidal suspensions can not only provide new insights in these kind of systems, but colloids are also a great tool to study statistical mechanics and are often used as a model system for atoms [1–3].

Colloids are defined as particles with at least one dimensions in the range between 1 nm to 1 µm, and are usually dispersed in a molecular solvent [4]. Both the colloids and solvent can be in either the gas, liquid or solid state. The size range of colloids means that they are small enough to still exhibit Brownian motion, as Einstein pointed out based on the kinetic theory of gases [5, 6], and Perrin later verified experimentally [7, 8]. This means that colloids can explore phase space just as atoms and molecules do, and therefore exhibit much of the same phase behaviour. As they are much larger than molecules however, the time scales in which processes happen are larger, making them considerably easier to observe. Their size also means they can be easily observed via optical microscopy techniques in real time, which is not possible for molecular systems. The properties of colloidal suspensions can easily be tuned by changing the inter-particle interactions, e.g. by adjusting the surface of a colloid [9, 10] or adding polymer to induce a depletion interaction [11, 12].

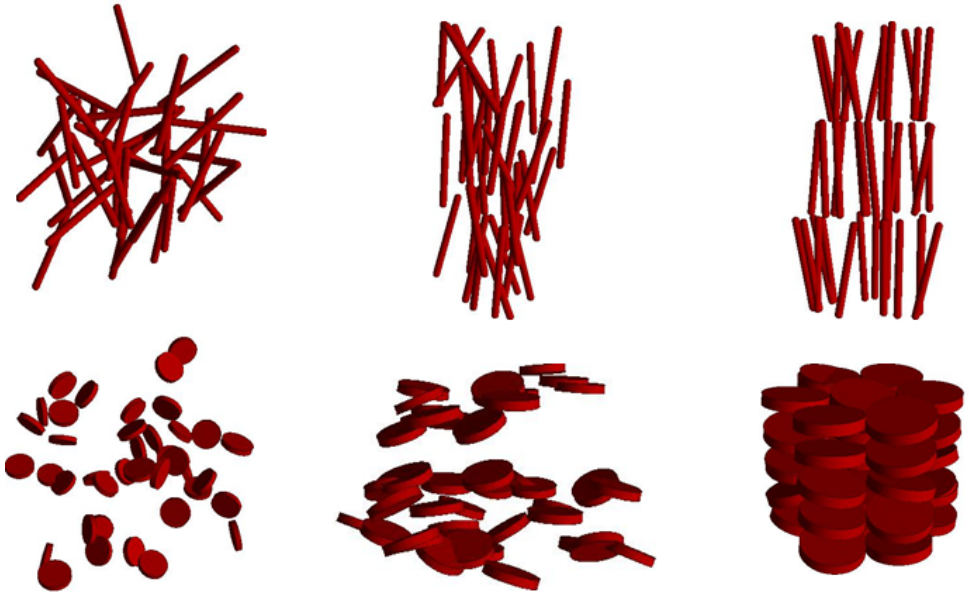


Figure 1.1: Several of the most common liquid crystalline phases for rods (top) and platelets (bottom). The isotropic phases are shown on the left, nematic phases in the middle and on the right are a smectic A and columnar phase for rods and platelets respectively.

Colloidal particles come in many shapes and sizes, e.g. spheres [13–16], rods [17–19], cubes [19–21] and peanuts [19, 21], or more complicated systems such as patchy particles [22], janus particles [23, 24] or lock-and-key particles [25]. Whereas spherical colloids have been studied extensively, the behaviour of anisotropic particles is much more complex, and is far less understood. In this thesis we study suspensions of colloidal rods, which is one of the simplest non-spherical shapes possible, and probe some of the properties associated with the anisotropic nature of these particles in confinement (section 1.3) and flow (section 1.4).

1.2 Liquid Crystals

Spherical colloids can form different phases, e.g. gas, liquid, solid and glass [2]. Anisotropic particles can exhibit even richer phase behaviour, displaying many liquid crystalline phases, which are in between a solid and a liquid [26, 27]. Due to their anisotropy, they do not only display positional order, but may also have orientational order, leading to a plethora of extra phases.

Figure 1.1 shows several of the more common liquid crystalline phases for rods and platelets [28]. An isotropic phase, shown on the left in figure 1.1, is completely disordered in both the

orientation and position of the particles. When a system displays no positional order, but the particles on average are oriented along the same direction, it is called a nematic phase. A schematic representation is shown in the middle of figure 1.1. Columnar and smectic phases, shown on the right hand side of figure 1.1, possess not only orientational order, but also have positional order in one or two dimensions respectively. Note that columnar and smectic phases can occur in both rods and platelets, but columnar phases are more often seen in systems consisting of platelets, and smectic phases are more common for rods.

Liquid crystals were first discovered by Reinitzer and Lehmann, who, when studying suspensions of cholesterol derivatives, noticed that an additional phase existed in between the solid and the liquid phase [29, 30]. Such molecular liquid crystals are thermotropic, meaning that the phase transitions are governed by temperature. In contrast, colloidal liquid crystals are lyotropic, which means that one can move through the different liquid crystalline phases by changing the concentration of particles.

The first colloidal liquid crystals were reported in 1925 by Zocher, who studied V_2O_5 ribbons that formed a nematic phase [31]. Since then, a wide range of colloidal liquid crystalline systems have been discovered or developed, some of which consist of inorganic minerals [32, 33] like the V_2O_5 ribbons studied by Zocher and clay particles such as California bentonite clay [34], gibbsite [35], and boehmite [36], but the list also includes many particles of biological origin, such as tobacco mosaic virus [34], *fd*-virus [37] and DNA [38].

1.2.1 Isotropic-Nematic phase transition

A theoretical framework for hard rods and platelets was first developed by Onsager in 1949 [39], who showed that a minimisation of the free energy predicts an isotropic-nematic phase transition. Onsager theory considers monodisperse, rigid rods with a high aspect ratio; $L/D \to \infty$, where L and D are the length and diameter of a rod respectively. Here we will summarise the main equations in the derivation of the Onsager theory, starting from the virial expansion for non-ideal solutions. A more in-depth derivation can be found in [40].

The Helmholtz free energy for a non-ideal solution of spherical particles is given by

$$\frac{\beta F}{N} = \beta\mu_0 + \ln(\rho\Lambda^3) - 1 + B_2\rho + \frac{B_3}{2}\rho^2 + ..., \tag{1.1}$$

where F is the Helmholtz free energy, N the number of particles, $\beta = \frac{1}{k_B T}$ the inverse temperature, μ_0 the reference chemical potential of the solute, $\rho = \frac{N}{V}$ the number density, $\Lambda = \frac{h}{\sqrt{2\pi m k_B T}}$ the thermal wavelength and B_i the i^{th} virial coefficient. The virial coefficients depend on the pair interactions u_{ij} between particles. The second virial coefficient takes into account only interactions between two particles at a time, B_3 concerns simultaneous interactions between three particles, and so on. The virial coefficients are proportional to integrations over Mayer functions $\Phi_{ij} = e^{-\beta u_{ij}} - 1$ [41], where u_{ij} is the interaction potential between particles i and j;

$$\begin{aligned} B_2 &= -\frac{1}{2V} \iint \mathrm{d}\vec{r_1}\, \mathrm{d}\vec{r_2}\ \Phi_{12} \\ B_3 &= -\frac{1}{3V} \iint \mathrm{d}\vec{r_1}\, \mathrm{d}\vec{r_2}\, \mathrm{d}\vec{r_3}\ \Phi_{12}\Phi_{23}\Phi_{13}. \end{aligned} \tag{1.2}$$

For solutions of rod-shaped particles, the orientation of particles needs to be taken into account as well. We consider the orientation distribution function $f(\Omega)$, which describes the probability of finding a rod with orientation Ω. In the isotropic phase all orientations are equally likely, and therefore $f_{iso}(\Omega) = \frac{1}{4\pi}$. In the nematic phase $f(\Omega)$ is not uniform, and as a result an orientational entropy multiplied by temperature, TS_{or}, should be subtracted from the free energy. S_{or} can be derived by considering particles with different orientations to be different species, and is given by

$$S_{or} = -Nk_B \int \mathrm{d}\Omega\ f(\Omega) \ln(4\pi f(\Omega)). \tag{1.3}$$

A second consequence of considering the orientation of particles is that the virial coefficients should be averaged over all orientations, as the inter-particle interactions depend on the orientation of particles;

$$B_2 = -\frac{1}{2V} \iiint \mathrm{d}\vec{r_{12}}\, \mathrm{d}\Omega_1\, \mathrm{d}\Omega_2\ \Phi_{12}(\Omega_1, \Omega_2) f(\Omega_1) f(\Omega_2). \tag{1.4}$$

Because we are considering hard rods, the inter-particle interactions depend only on the excluded volume V_{exc} of rods, as $u_{ij} = \infty$ for overlapping particles and $u_{ij} = 0$ otherwise. This simplifies the Mayer functions to $\Phi_{ij} = -1$ and $\Phi_{ij} = 0$ for overlapping and non-overlapping

particles respectively. The integrals over these Mayer functions can then be rewritten as

$$\frac{1}{V}\iint \mathrm{d}\vec{r_1}\,\mathrm{d}\vec{r_2}\;\Phi_{12} = \int_{overlap} \mathrm{d}\vec{r_{12}}\;(-1) = -V_{exc}(\Omega_1,\Omega_2). \tag{1.5}$$

If we assume the rods to be spherocylinders, the excluded volume can be approximated as $V_{exc} \approx 2L^2D|\sin\gamma|$, where γ is the angle between the orientations of the two rods. Substituting this in the second virial coefficient we find

$$B_2 = L^2D\iint \mathrm{d}\Omega_1\,\mathrm{d}\Omega_2\;|\sin\gamma(\Omega_1,\Omega_2)|f(\Omega_1)f(\Omega_2). \tag{1.6}$$

Combining equations (1.1), (1.3) and (1.6) and defining a dimensionless concentration $c = \frac{\pi}{4}L^2D\rho$, we find for the Helmholtz free energy

$$\begin{aligned}\frac{\beta F}{N} = \beta\mu_0 + \ln(\rho\Lambda^3) - 1 + \frac{4c}{\pi}\iint \mathrm{d}\Omega_1\,\mathrm{d}\Omega_2\;|\sin\gamma(\Omega_1,\Omega_2)|f(\Omega_1)f(\Omega_2)\\ + \int \mathrm{d}\Omega\;f(\Omega)\ln(4\pi f(\Omega)),\end{aligned} \tag{1.7}$$

where we have truncated the virial expansion after the second virial term, which has been shown to be quantitatively accurate for $L/D > 100$ using Monte Carlo simulations [42]. The first integral in equation (1.7) represents the packing entropy, which is a measure of the free volume available to individual rods, and the second integral concerns the orientational entropy of the system, which is maximised when particles are randomly oriented. At low concentrations the orientational entropy is dominant, resulting in a random orientation of rods, i.e. an isotropic phase. At high concentrations the packing entropy dominates, and particles align along the same direction in order to maximise their free volume, leading to a nematic phase.

To find the equilibrium situation for a given concentration, the Helmholtz free energy (equation (1.7)) needs to be minimised. In order to do this, one can use a trial function for $f(\theta)$ with one or more variational parameters and solve equation (1.7) by minimising with respect to these variational parameters. Here we use a Gaussian distribution as a trial function [43];

$$\begin{aligned} f(\theta) &= N(\alpha)e^{-\frac{\alpha\theta^2}{2}} && 0 \leq\theta \leq \frac{\pi}{2}\\ &= N(\alpha)e^{-\frac{\alpha(\pi-\theta)^2}{2}} && \frac{\pi}{2} \leq\theta \leq \pi,\end{aligned} \tag{1.8}$$

where $N(\alpha)$ is a normalisation constant. For large α this distribution is strongly peaked, rep-

resenting a nematic phase, whereas $\alpha = 0$ leads to a constant orientation distribution, i.e. an isotropic phase.

Using equation (1.8) we can express the Helmholtz free energy in equation (1.7) in terms of α;

$$\frac{\beta F}{N} \sim \ln \alpha + \frac{4c}{\sqrt{\pi\alpha}} + const. \tag{1.9}$$

Minimising this equation with respect to α yields $\alpha = \frac{4c^2}{\pi}$. The nematic order parameter for the system (see section 1.2.2) is given by $S \sim 1 - \frac{3}{\alpha}$. The isotropic-nematic coexistence region can finally be found by equating chemical potentials and pressures of the two phases. This leads to a first-order phase transition, with the following volume fractions and order parameters for the two phases at coexistence:

$$\begin{aligned} \phi_{iso}\frac{L}{D} &= 3.45 \qquad & S_{iso} &= 0 \\ \phi_{nem}\frac{L}{D} &= 5.12 \qquad & S_{nem} &= 0.910, \end{aligned} \tag{1.10}$$

where $\phi = \rho V_p$, with ρ the number density of rods and V_p the volume of a particle.

Although Onsager theory is very useful in understanding the isotropic-nematic phase transition, there are some limitations to its validity. First of all, as already mentioned, it is only quantitatively accurate for relatively long and thin rods, with $L/D > 100$. Onsager theory also assumes that rods are monodisperse and rigid, which is not the case for most experimental systems. Furthermore the isotropic-nematic phase transition can be affected by external factors. One example of this is the capillary nematisation transition induced by confining a system between parallel walls, which we show in chapter 4.

1.2.2 Nematic liquid crystals

Arguably the simplest liquid crystal phase is a nematic, which can be fully described by the director $\vec{n}(\vec{r})$, representing the average local orientation of particles, and the order parameter

$$S = \frac{3\left\langle \cos^2\theta \right\rangle - 1}{2}, \tag{1.11}$$

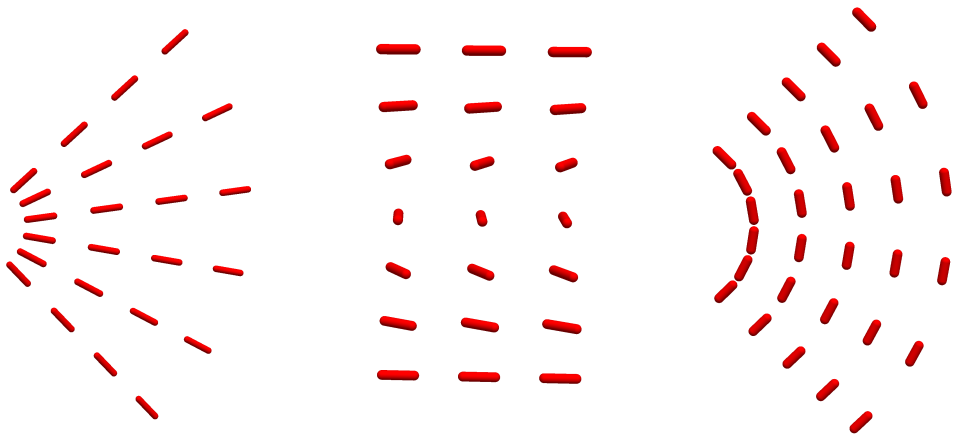


Figure 1.2: Schematic example of the splay (left), twist (centre) and bend (right) deformations in nematic liquid crystals.

which ranges from 0 (completely disordered) to 1 (perfect ordering). Here, θ is the angle between the orientation of a particle and the director $\vec{n}$.

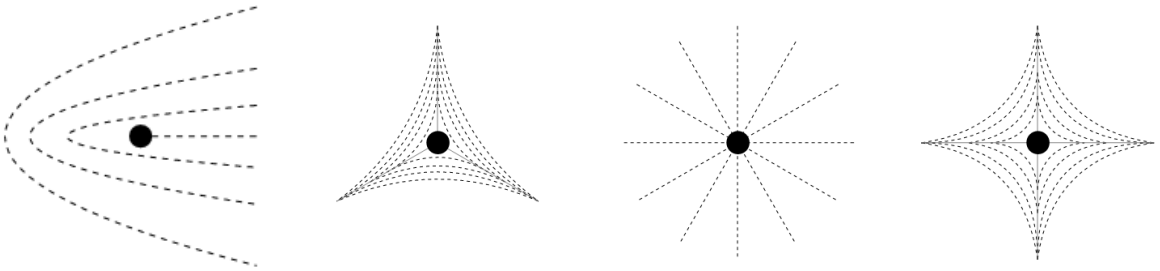
The lowest energy state for a nematic liquid crystal is a uniform director field with $S \to 1$, i.e. where all the particles have approximately the same orientation. In practice a director field is easily distorted from this uniform state. These distortions can either be random, lowering the order parameter, continuous (deformations) or discontinuous (defects).

Any continuous distortion can be described by the Oseen–Frank elastic energy density [44, 45], given by

$$F_e = \frac{K_1}{2}\left(\nabla \cdot \vec{n}\right)^2 + \frac{K_2}{2}\left(\vec{n} \cdot \nabla \times \vec{n}\right)^2 + \frac{K_3}{2}\left(\vec{n} \times \nabla \times \vec{n}\right)^2, \tag{1.12}$$

where the three terms correspond to the splay, twist and bend distortion respectively (see figure 1.2), and K_i are the elastic constants associated with these deformations. The saddle-splay and splay-bend terms have been neglected here, which is valid for strong anchoring conditions, where the orientation of particles at the walls is fixed due to the particle-wall interactions [46]. The elastic constants depend on the system studied, but as a rough estimate, they should scale as $K_i \sim \frac{U}{L}$, where U is the interaction energy between particles, and L is the particle size [26]. For lyotropics, the elastic constants should therefore scale as $K_i \sim \frac{k_B T}{L}$, which for typical colloidal systems is on the order of 10^{-15} N. Typical values for thermotropic liquid crystals lie within the range of 10^{-13}–10^{-11} N [47–49].

Discontinuous distortions can either be point defects or line defects. Many different types



(a) $s = \frac{1}{2}$ (b) $s = -\frac{1}{2}$ (c) $s = 1$ (d) $s = -1$

Figure 1.3: Schematic representation of point defects with strength (a) $s = \frac{1}{2}$, (b) $s = -\frac{1}{2}$, (c) $s = 1$ and (d) $s = -1$. Dashed lines represent the director field, the black dots indicate the location of defects.

of point defects can be identified, which are described by their strength s [50]. In short, s describes the change in director orientation when tracing a full circle around the defect, via $\Delta\theta = 2\pi s$. Figure 1.3 shows some of the more common types of defects and their strength. The energy cost associated with a point defect is given by [27]

$$E_{def} = \frac{\pi}{4} K s^2 \ln\left(\frac{R}{\epsilon}\right), \tag{1.13}$$

where K is the average elastic constant, ϵ is the radius of the defect core region, which is on the order of the nematic correlation length [51] and R is the sample size. As the energy scales with s^2, formation of defects with a high strength is unfavourable.

1.3 Confinement

Confinement of a system introduces new and interesting behaviour, which can be very different from that seen in bulk [52]. Not only do the interactions between the confining walls and the system become more important, as a larger percentage of particles are in close proximity to a wall, but the finite size of the system itself can change its properties [53, 54]. Understanding the effects of confinement is vital in the development of for example liquid crystal displays, where there is an ongoing trend towards smaller cells. When properly understood, the effects of confinement can even be exploited, e.g. by patterning the confining walls to create bistable topological states [55,56]. Confinement also plays an essential role in many biological processes, as many intracellular structures are of comparable size as the cell itself, and therefore will experience finite size effects. For example, protein folding [57] and virus assembly [58] have been

shown to be affected by crowding and confinement.

Although observing systems at the microscale has been possible since the introduction of the optical microscope in the 1600s, manipulation started only in the 1970s with the development of micro-mechanical systems (MEMS) [59]. Some of the early industrial successes of MEMS include airbag activation systems (1980s) and inkjet printers (1990s) [60]. Not long after the start of these silicon-based micro-machines, the first microfluidics devices were developed, which led to miniaturised systems able to perform for example chromatography [61], DNA amplification [62] or chemical reactions [63]. The amount of control we have over such systems on the nano- to micrometer scale today means it is possible to confine colloidal systems down to a size comparable to the colloids themselves, allowing us to study the physics of such systems in confinement, where most macroscopic theories break down. For example, the experiments described in chapters 5 and 6 use microfluidics to flow colloidal rods through a channel with a height of only three times the rod length.

One of the most well-known effects of confinement is capillary condensation, where a system spontaneously forms a liquid in a small capillary, even though in bulk it would form a gas at the same pressure [4]. In more general terms, many phase transitions and phase separations have been found to shift as a result of confinement [53,54,64]. In some systems, completely new phases may arise in confinement, that would never occur in bulk. An example is the hexatic phase for confined spherical particles, which is thought to only occur in (quasi-)2D systems [65–67].

Liquid crystals can also display many new phases as a result of confinement. An isotropic phase can undergo capillary nematisation upon strong confinement, as we show in chapter 4. A nematic liquid crystal in confinement will be subject to a competition between anchoring, which determines the preferred orientation of particles at the walls, and elastic distortions, which can result in interesting new director fields [68–70].

Confinement does not only change the structural properties of a system, but can also change the dynamics of processes [71]. For example, the kinetics of phase separation of a polymer blend have been shown to depend on the sample thickness [72] and in another study, the deformation and droplet breakup point (in terms of capillary number) were found to depend on the degree of confinement [73]. Another example is the demixing of colloid-polymer mixtures, where droplet growth dynamics were found to change significantly as a result of confinement [74].

Chapters 3 and 4 deal with liquid crystals in confinement, where we investigate the effects of strong confinement on the structural properties of the system.

1.4 Flow in confinement

Flow in confinement is fundamentally different from that in macroscopic systems. The Reynolds number Re, defined as the ratio between inertial and viscous forces, is typically very low in confined systems. The Reynolds number is given by

$$Re = \frac{\rho u l}{\eta}, \tag{1.14}$$

where ρ is the density of the fluid, u is the characteristic velocity of the system, l the characteristic length scale and η the viscosity. For colloidal systems on the microfluidic scale, where velocities are usually on the order of $u \sim$ cm/s or smaller, and the length scales are typically $l \sim 10\,\mu$m, the Reynolds number generally does not exceed 10^{-1} [60]. This means that inertial forces can be neglected, and the flow is dominated by viscous forces, leading to a smooth, laminar flow.

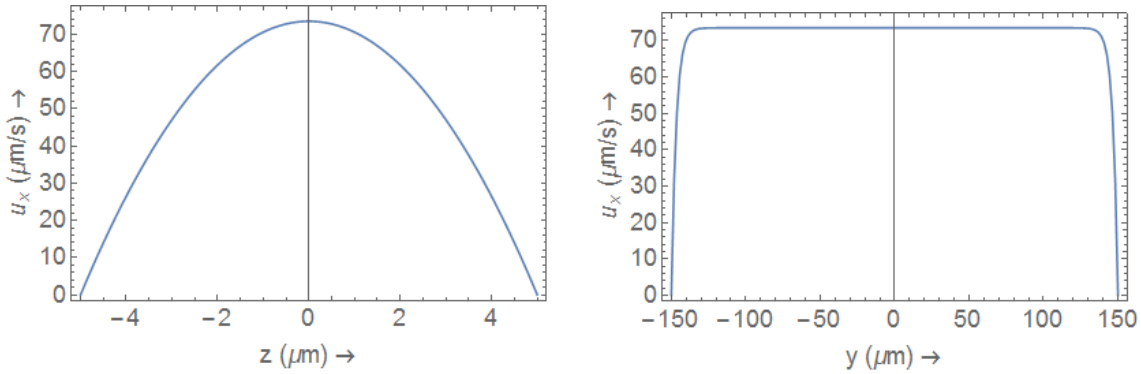
The flow of a Newtonian fluid at low Reynolds number is governed by the Stokes equations [75],

$$\begin{aligned} \nabla p &= \eta \nabla^2 \vec{u} + \vec{F}, \\ \nabla \cdot \vec{u} &= 0 \end{aligned} \tag{1.15}$$

where p is pressure, $\vec{u}$ the velocity and $\vec{F}$ are external forces applied to the system. Solving the Stokes equations for a channel with a rectangular cross-section, which is typically the case in microfluidic channels, gives [60]

$$u_x(y,z) = \frac{4\Delta p}{\eta w} \sum_{n=1}^{\infty} \frac{(-1)^{n+1}}{\beta_n^3} \left(1 - \frac{\cosh(\beta_n z)}{\cosh(\beta_n \frac{h}{2})}\right) \cos(\beta_n y), \tag{1.16}$$

where Δp is the pressure gradient, w and h are the width and height of the channel respectively and $\beta_n = (2n-1)\frac{\pi}{w}$. The axes are defined such that flow is in the x-direction, the width of the channel is along the y-direction, and the height along z. Figure 1.4 shows the flow profiles for a microfluidic channel with $w = 300\,\mu$m and $h = 10\,\mu$m, which are the typical dimensions



(a) (b)

Figure 1.4: Theoretical flow profiles in the microfluidic channels used in chapters 5 and 6, (a) in the xz-plane and (b) in the xy-plane.

of channels used in chapters 5 and 6. The flow profile can essentially be described as a planar Poiseuille flow in the xz-plane, with a constant flow velocity in the xy-plane, except close to the walls.

Another important constant to describe the flow of particles is the Péclet number. We can define two separate Péclet numbers; a translational one, which is a measure for the relative importance of convection and diffusion, and a rotational one, which compares the relative importance of rotational Brownian motion and shear rate. These Péclet numbers are defined as

$$\begin{aligned} Pe_t &= \frac{uL}{D}, \\ Pe_r &= \frac{\eta\dot{\gamma}L^3}{k_BT}, \end{aligned} \tag{1.17}$$

where D is the diffusion coefficient, $\dot{\gamma}$ is the shear rate, L is the length of a rod, and k_BT is the thermal energy. For the flow experiments described in this thesis, the translational Péclet number is on the order of $Pe_t \sim 10^2$, meaning that convection dominates and the effect of diffusion is negligible for the transport of particles. The rotational Péclet number is typically on the order of $Pe_r \sim 50$, which means that shear is much more important than Brownian motion to describe the orientational behaviour of particles.

In chapters 5 and 6 we study the orientational behaviour of colloidal rods in a shear flow, with flow profiles as shown in figure 1.4. Rods in a simple shear flow are known to undergo periodic tumbling motion, where they align along the direction of flow for most of the time and periodically flip their orientation by 180°. The possible paths followed during this flipping

motion are described by Jeffery orbits [76], which are discussed in more detail in section 5.2.

1.5 Thesis outline

Chapter 2 introduces the systems studied and some of the experimental techniques used throughout this thesis. In chapter 3, we describe a mathematical method for calculating distortion energies in a liquid crystal from single-particle data, and illustrate this method by applying it to both artificial data, and experimental results for *fd*-virus particles confined in wedges. Chapter 4 examines capillary nematisation of *fd*-virus rods in confinement, by studying the phase behaviour in microfluidic channels of different heights. This is the first experimental observation of capillary nematisation in a colloidal liquid crystal. We compare our results with two different theories and find reasonable agreement with both. Chapters 5 and 6 concern the flow behaviour of silica rods in a Poiseuille flow. The most simple case of non-magnetic rods in water is discussed in chapter 5. We compare our results for the orientational behaviour of rods with simulations and find qualitative agreement. In chapter 6 we investigate the influence of a magnetic field and the influence of a non-Newtonian fluid as a medium on the orientation of flowing rods.

Chapter 2

System and experimental methods

This chapter introduces the experimental systems and techniques used throughout this thesis. The colloidal rods studied, *fd*-virus and silica rods, are shortly introduced. The process of making microfluidic channels using soft lithography is explained for both PDMS and UV glue channels. The microscopy techniques used to study the samples and the magnetic set-up are discussed. Finally, the image analysis techniques used to analyse microscopy images are summarised.

2.1 Colloidal rods

Two different model systems are used in this thesis. In chapters 3 and 4 *fd*-virus suspensions are used, while the flow experiments described in chapters 5 and 6 were done using silica rods. Both of these systems are shortly introduced here. Note that the author did not grow or synthesise either of the rods; *fd*-virus was supplied by Prof. Pavlik Lettinga from the Forschungszentrum Jülich, and the silica rods were synthesised by Dr. Yongxiang Gao from the University of Oxford.

2.1.1 *fd*-virus

fd is a filamentous bacteriophage that was first discovered in the New York sewers and purified in 1963 by Marvin and Hoffmann-Berling [77]. The virus particles have a length of 880 nm and a diameter of 6.6 nm and are semi-flexible, having a persistence length of 2200 nm. They consist of a single circular strand of DNA enveloped by a protein shell of approximately 2750 copies of the major coat protein (pVIII) and several minor coat proteins at both ends [78]. At $pH = 8.2$, used for *fd*-virus samples throughout this thesis, *fd*-virus is negatively charged, with a charge density of roughly 10 charges/nm [79], which ensures electrostatic stabilisation of the particles.

fd-virus particles can be grown in suspensions of E. Coli, which the virus infects to multiply itself. The exact method for growing *fd*-virus particles is described in [17]. Although this method is relatively simple, the yield is very low, typically 15–20 mg virus per litre of infected E. Coli [17].

At low concentration, suspensions of *fd*-virus form an isotropic phase. With increasing rod concentration the system will go through a cholesteric, smectic, columnar and finally a crystalline phase [80]. The high aspect ratio of the rods means that they are described very well by Onsager theory [39], which assumes infinitely long rods. This, and the fact that as a biological particle they are monodisperse, makes *fd* an ideal model system to study colloidal liquid crystals.

The surface of *fd*-virus particles can be functionalised with a fluorescent dye, Alexa-488. This enables us to study virus suspensions on the single-particle level by labelling a small fraction of the particles, which can then be imaged using confocal laser scanning microscopy.

2.1.2 Silica rods

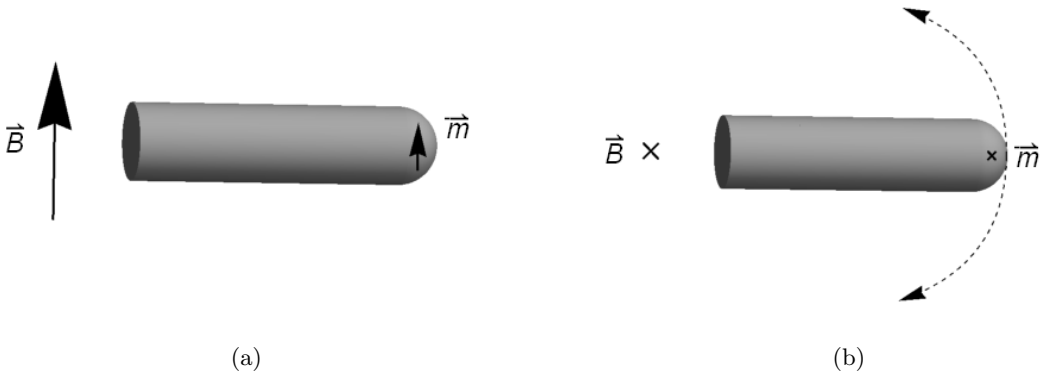
The silica rods used in this thesis were synthesised by Dr. Yongxiang Gao using a method based on that described in reference [18]. This involves forming an emulsion of ethanol/water in pentanol, stabilised by polyvinylpyrrolidone (PVP). Tetraethyl orthosilicate (TEOS) is then added, and silica particles start to grow from the surface of the emulsion droplets. The emulsion droplets stay attached to one end of the silica particle, which results in the asymmetric growth needed to obtain rods. The surface of the particles is negatively charged with SiO^- groups, giving the particles a zeta-potential of $-54\,\mathrm{mV} \pm 6\,\mathrm{mV}$, which is well below the threshold value of $-30\,\mathrm{mV}$ required for colloidal stability [81].

The resulting rods are bullet-like in shape, i.e. one end is a spherical cap, while the other end is straight. They are approximately 3–3.5 µm in length, depending on the exact synthesis procedure, and have a diameter of 0.5 µm. The polydispersity in both length and diameter is typically 5-8%. The rods have a gravitational length of $L_g = \frac{k_B T}{mg} \approx 0.8\,\mu\mathrm{m}$ in water, which means they will sediment to the bottom of a sample cell. With increasing concentration, the rods can form an isotropic, nematic and smectic phase. Because they readily sediment, the system can also exhibit 2D equivalents of these liquid crystalline phases.

A nice feature of these silica rods is that they can be doped with different materials during the synthesis at only one end of the rod, effectively creating a Janus-rod [82]. In this thesis, we have used un-doped rods and rods containing magnetite (Fe_3O_4) nanoparticles, which are approximately 26 nm in diameter. These magnetite particles give the silica rods a permanent magnetic dipole of approximately $m = 1.4\,k_\mathrm{B}T/\mathrm{G}$. The dipole is usually oriented perpendicular to the long axis of the rod, which means that by applying a strong magnetic field, the rod orientation is fixed to a plane perpendicular to the field direction. This is shown schematically in figure 2.1.

2.2 Soft lithography

Soft lithography is a widely used technique in soft matter and biology, as the typical size of systems studied in these fields, e.g. colloids or cells, is of the same order as the devices made using soft lithography. In this thesis, we mainly use soft lithography to create channels in which



(a) (b)

Figure 2.1: (a) Orientation of the magnetic dipole, $\vec{m}$, in iron oxide-doped silica rods with respect to the rod and magnetic field, $\vec{B}$. (b) The rod can freely rotate in the plane perpendicular to the magnetic field. Rotation in the other directions is limited.

we can confine our system, down to a channel height of approximately 2-3 times the length of the rods studied.

Microfluidics channels of two different materials, namely polydimethylsiloxane (PDMS) and UV glue (Norland Optical Adhesive 81) were used in this thesis. Channels made from UV glue have many advantages over PDMS channels; they are airtight, while PDMS is permeable to gasses, they are less prone to leaking and the surface stays hydrophilic for much longer. A sample in a UV glue channel can typically be kept for days, compared to just hours in a PDMS channel. However, setting up a flow system is much easier using PDMS, as the inlet and outlet tubes can be directly connected to the PDMS, whereas UV glue channels would require sand blasting holes and attaching special connection parts [83]. For these reasons, UV glue channels were used in chapters 3 and 4, which concern non-flowing equilibrium systems, while PDMS channels were used for the flow experiments described in chapters 5 and 6.

Figure 2.2 schematically shows the process of creating microfluidic channels of both PDMS and UV glue. First, a mould for the channels is created in SU-8 (Micro Chem) on a silicon wafer. To do this, 5 ml of SU-8 is spin-coated onto a silicon wafer. The type of SU-8 used and the spin velocity determines the thickness of the SU-8 layer on the silicon wafer, and therefore height of the final channels.

After spin-coating, the wafer is soft baked for 2 minutes at 95 °C to improve the adherence of SU-8 to the wafer. A photomask, with the structure of the channels printed on it, is then placed over the wafer together with a longpass UV filter, and the wafer is irradiated with UV

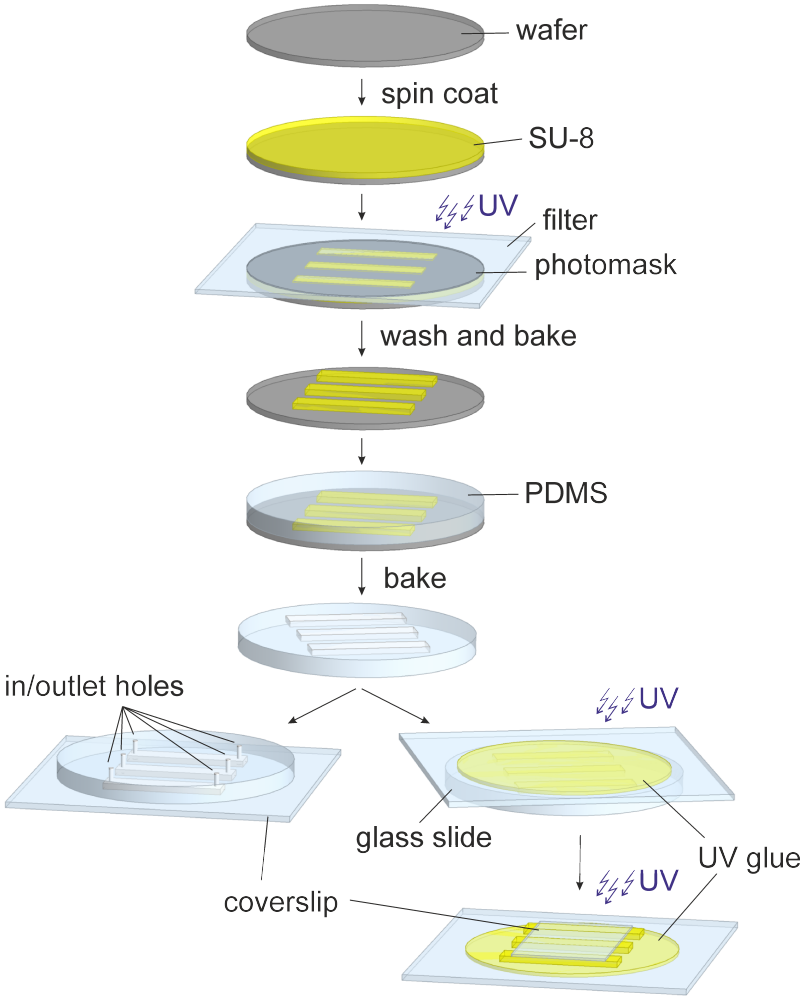


Figure 2.2: Process of producing microfluidic channels in PDMS (left) and UV glue (right).

light of approximately 130 mJ/cm^2 for 10–15 s, where the exact intensity and duration depend on the thickness of the SU-8 layer.

The wafer is then soft baked again for 2 minutes at 95 °C and the unexposed, non-polymerised regions of SU-8 are washed away. The wafer is then hard baked a final time at 150 °C for approximately 30 minutes. Once finished the silicon wafer mould can be used multiple times to create microfluidic channels.

2.2.1 Polydimethylsiloxane (PDMS)

In order to make PDMS channels, tape is wrapped around the silicon wafer mould to create a bowl in which a PDMS solution (Sylgard 184 silicon elastomer kit, Dow Corning) is poured. The PDMS is then left under vacuum for several hours to remove air bubbles, and baked over night at 80 °C. The PDMS slab is then removed from the silicon wafer, and holes are punched through the PDMS, inside the channels, using a hollow syringe needle to create an inlet and outlet for flow experiments. The PDMS and a coverslip are then treated with an oxygen plasma, making their surface hydrophilic. After this, the two are firmly pressed together, forming a covalent bond between them and closing the channels. Tubes can then be inserted into the inlet and outlet holes.

2.2.2 UV-glue

UV glue channels can be made using a PDMS mould, which is made using the method described above, with the exception that no holes are punched through the PDMS, and no coverslip is attached. A small drop of UV glue is then put on the channels in the PDMS mould and covered with a microscope slide. The channel is irradiated with UV light for approximately 30 seconds, which partly polymerises the glue. The PDMS mould is removed, and a coverslip is attached to the UV glue channel, leaving the ends of the channel open so that they can be filled later via capillary action. The channel is then irradiated for another 30 seconds to fully polymerise the glue. To strengthen the glue further, the channels are baked over night at 50 °C.

Note that as a PDMS slab is used as a mould, the final channels in UV glue are the inverse of this. Therefore a single wafer cannot be used to make both PDMS and UV glue channels.

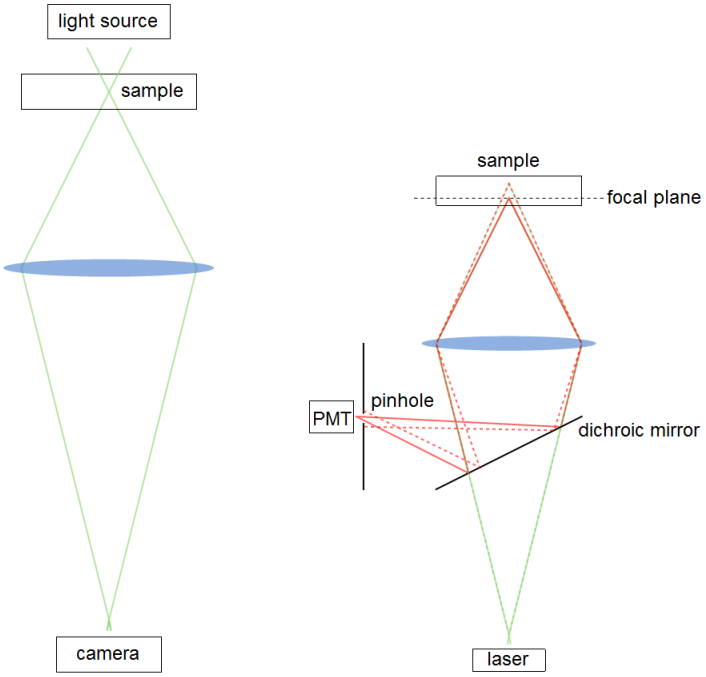
2.3 Microscopy

Microscopy is the perfect tool to study colloidal systems. The typical size of a colloid ($\sim$1 µm) is well within the resolution of an optical microscope, which is on the order of the wavelength of the light used for illumination [84]. As colloids are relatively slow, with a Brownian time on the order of $t_B = 1\,\mathrm{s}$, most physical processes in colloidal systems can easily be recorded in real time.

Bright field microscopy is the simplest microscopy technique, where a light source is placed on one side of the sample to be studied, and an objective lens and camera on the other side. This set-up is schematically shown in figure 2.3(a). As the light travels through the sample, it is transmitted differently by different objects in the sample, creating the contrast needed to obtain a good quality image. The light is then focussed by the objective lens, creating a magnified image of the sample onto the camera.

Confocal microscopy is a more sophisticated technique, in which the resolution is increased by using a pinhole to exclude light from out-of-focus sources and contrast is greatly increased by using fluorescence as opposed to light transmission. The basic set-up for such a microscope is shown in figure 2.3(b). A laser is typically used as a light source for confocal microscopy, and is focussed onto the sample with an objective lens. The parts of the sample that are of interest are fluorescently labelled, and are excited by the incoming laser light. The light emitted from the fluorophores is then focussed onto a detector by the same objective lens used for the excitation light. A dichroic mirror is used to reflect the fluorescent light to the detector, while transmitting the laser light. A pinhole is placed close to the detector, exactly at the conjugate focal plane of the imaged point, to exclude light from any out-of-focus sources (dashed lines in figure 2.3(b)).

As the pinhole in a confocal microscope allows only light from the focus to reach the detector, a very small volume is actually imaged. A larger image can then be constructed by scanning the sample and combining the information from each point. This can be done not only in the xy-plane, perpendicular to the light path, but also in the z-direction, making confocal microscopy a powerful tool to image samples in three dimensions.



(a) (b)

Figure 2.3: Schematic representation of (a) a conventional bright field microscope and (b) a confocal microscope. The solid lines indicate the in-focus light path, the dashed lines in figure (b) indicate the light path for out-of-focus light.

2.3.1 Resolution

To illustrate the difference in resolution between conventional microscopy and confocal microscopy, we can look at the point spread function (PSF) for both systems. The PSF represents the probability that a photon reaches a certain point (ζ, ρ) in space [85], where ζ and ρ are dimensionless optical coordinates along the optical axis and in the focal plane respectively. These optical coordinates are related to real space by $\zeta = z\frac{2\pi NA^2}{n\lambda}$ and $\rho = r\frac{2\pi NA}{\lambda}$, where n is the refractive index of the solvent, λ is the wavelength of incoming light and $NA = n\sin\alpha$ is the numerical aperture of the objective lens, where α is half the opening angle of the light cone that can enter or leave the objective.

The PSFs for a conventional light microscope are given by [86]

$$PSF_{conv}(\zeta, 0) = \left(\frac{\sin(\zeta/4)}{\zeta/4}\right)^2, \tag{2.1}$$

$$PSF_{conv}(0, \rho) = \left(\frac{2J_1(\rho)}{\rho}\right)^2, \tag{2.2}$$

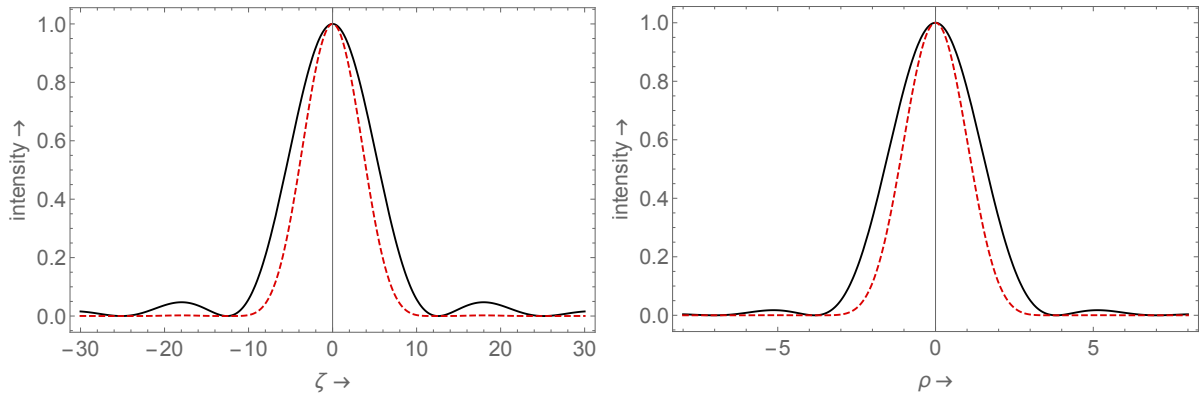


Figure 2.4: Comparison of (a)$PSF(\zeta, 0)$ and (b) $PSF(0, \rho)$ for a conventional microscope (black) and a confocal microscope (red dashed).

where J_1 is the first order Bessel function. The PSFs for a confocal microscope are simply the square of these conventional microscope PSFs, as the light is focussed twice by the objective, and the probabilities for the photon to reach a certain point therefore needs to be squared [87]. Figure 2.4 shows the PSFs for both a conventional microscope and a confocal microscope. It is clear from this comparison that the width of the PSFs is much smaller for a confocal microscope. Furthermore, the height of the second and subsequent maxima are much smaller for a confocal microscope, meaning that there is more light focussed in the main peak, leading to better contrast compared to a conventional microscope.

The resolution of a microscope is determined by the ability to distinguish two objects at a certain distance to each other. This ability is measured by the Rayleigh criterion, which states that two objects can be resolved if the minimum distance between the objects is such that the first minimum in intensity of one object coincides with the maximum in intensity of the second object [84, 88]. This corresponds to an intensity drop of at least 26% between the two maxima [87]. Figure 2.5 shows the intensity profiles for two points in space exactly at this limit for both a conventional and a confocal microscope. It can be seen from this plot that the minimum distance needed for two objects to be resolved is much smaller (by a factor 1.4) for a confocal microscope compared to a conventional microscope.

Most of the work described in this thesis was done on a single set-up that is a combination of an inverted bright field microscope and a confocal microscope. Confocal microscopy was used to study samples of *fd*-virus, where the high resolution was needed to accurately measure the orientation of the rods. Bright field microscopy was used to study the flow behaviour of silica

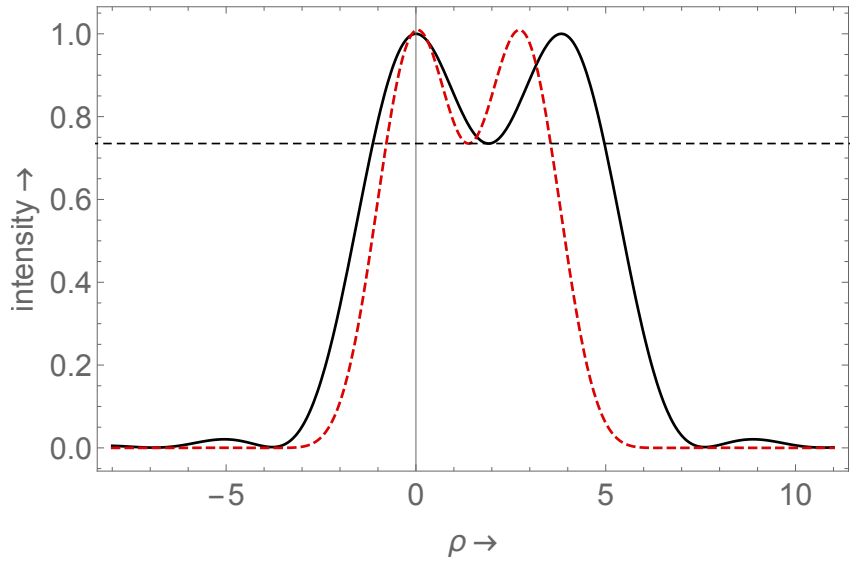
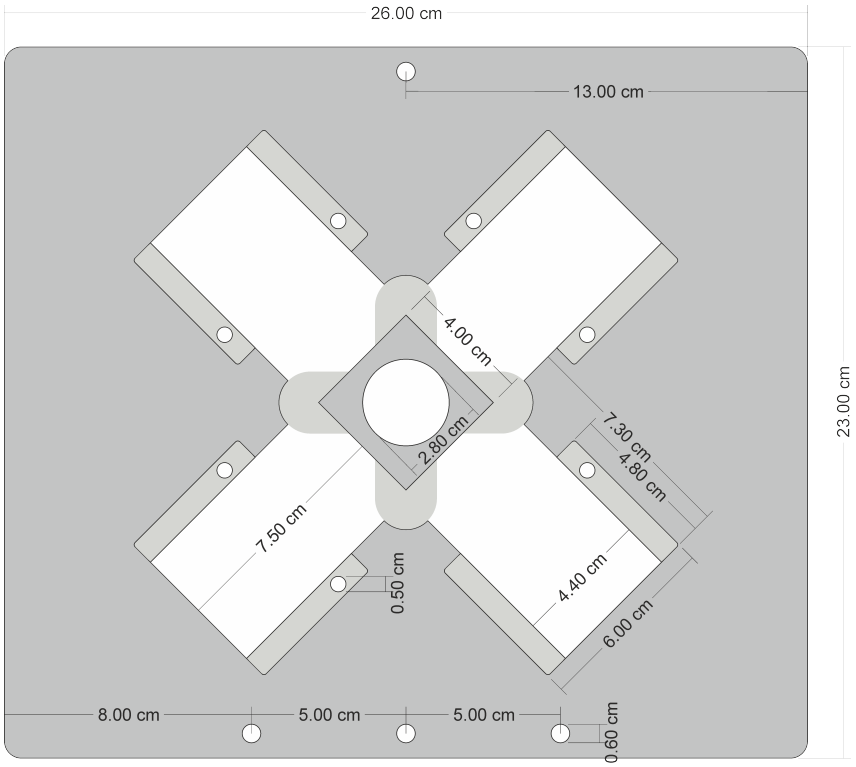


Figure 2.5: Combined PSFs for two points in space at the minimum distance at which the objects can be resolved for a conventional microscope (black) and a confocal microscope (red dashed). The gray dashed line indicates the minimum intensity drop needed for two objects to be resolved from each other.

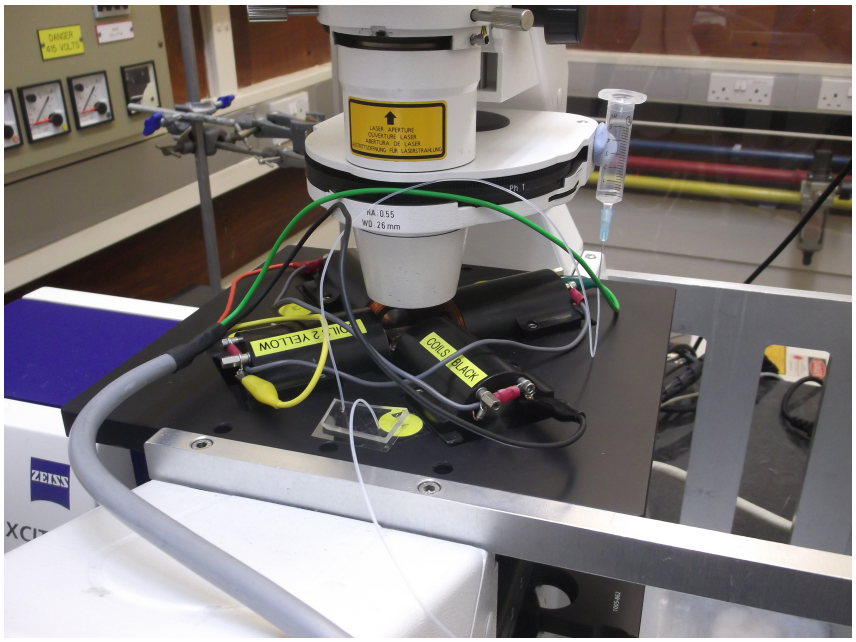
rods (chapters 5 and 6), which required real-time imaging of at least 10 frames/s in order to be able to follow the orientation change of a rod.

2.4 Magnetic set-up

The experiments described in chapter 6 involve applying a magnetic field, in different directions, to a sample while under the microscope. In order to do this, a special microscope stage with room for four solenoids was used, which allowed us to apply a magnetic field in any direction in the imaging plane by changing the current through each of the solenoids individually. Figure 2.6 shows a schematic drawing of this stage as well as a photograph of the stage mounted on the microscope. Field strengths of up to 20 G can be reached by increasing the current through the solenoids used. Solid iron cores can be added inside the solenoids to increase the field strength further, to a range of 20–150 G. To apply a magnetic field perpendicular to the field of view, a single, larger solenoid was placed around the sample. This solenoid can reach field strengths of up to 30 G. Figure 2.7 shows the calibration curves, in terms of magnetic field strength versus applied current, for both the four-solenoid system with iron cores and the solenoid used to create a magnetic field perpendicular to the field of view. The calibration itself was performed by Dr. Yongxiang Gao.

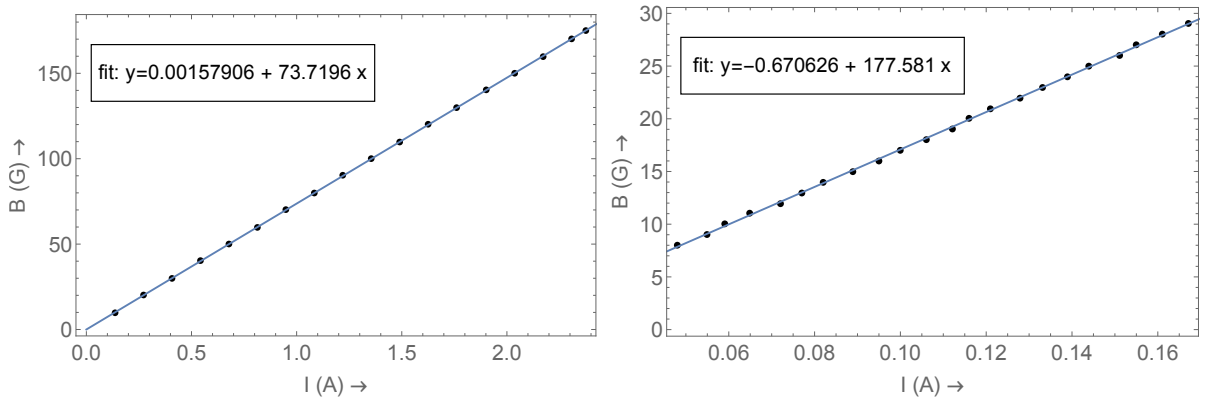


(a)



(b)

Figure 2.6: Microscope stage with four solenoids used to apply a magnetic field in any given direction within the imaging plane. (a) Schematic drawing of the microscope stage with solenoids and (b) a photograph of the microscope with the solenoids.



(a) (b)

Figure 2.7: Calibration curves for (a) the four-solenoid system used to apply a magnetic field in the imaging plane and (b) the solenoid used to apply a magnetic field perpendicular to the imaging plane.

2.5 Image Analysis

Image analysis forms an important part of the research described in this thesis, where accurately detecting rods in microscopy images and obtaining their positions and orientations is essential to analysing the properties of a sample. We use Mathematica^{TM} for all image analysis, which has many useful in-built functions for this purpose.

The process of image analysis is somewhat different depending on the sample studied. *fd*-virus particles are imaged using confocal microscopy, where typically the pixel size is 133–200 µm, meaning that a rod will only be 4–6 pixels long. The difficulty therefore lies mostly in distinguishing the virus particles from noise. The contrast is very good, as they are fluorescent particles against a dark background. Silica rods are much bigger and therefore easier to detect, but the contrast with the background is not as good, as they are imaged using bright field microscopy.

2.5.1 Particle detection

In bright field (BF) images, a background image is first calculated by averaging all frames in an image series, after which this background is subtracted from each image. For confocal microscopy (CSLM) images this is usually not necessary, as the background should be completely black. For both BF and CSLM, a bandpass filter is then applied to the image in order to reduce noise.

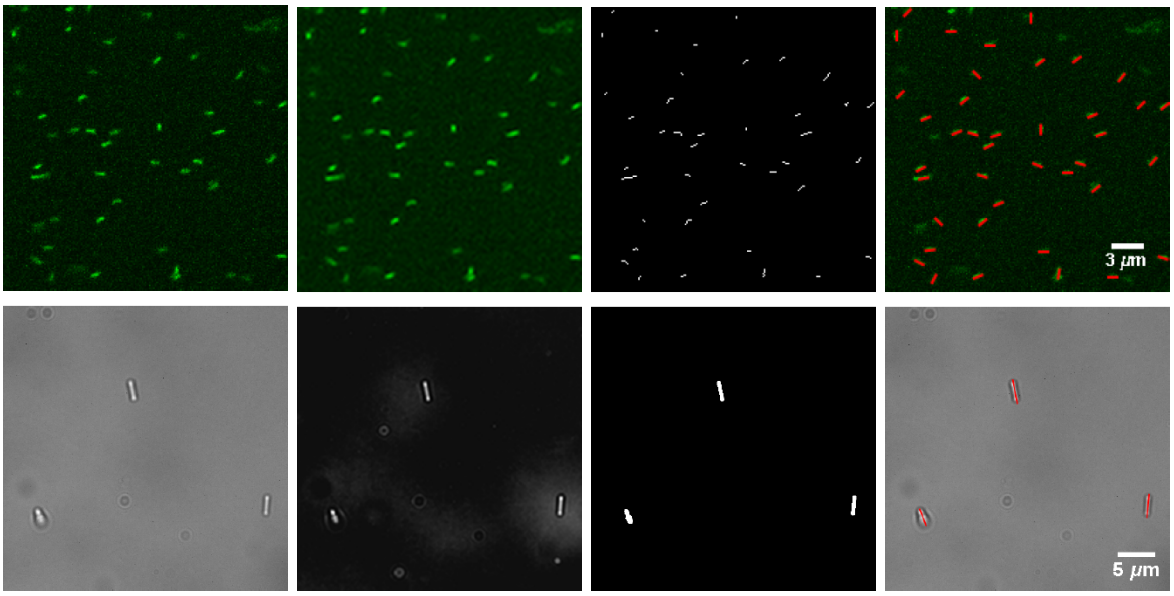


Figure 2.8: Basic image analysis process for *fd*-virus particles (top) and silica rods (bottom). (a) The original image, (b) the image after background subtraction (for silica rods) and filtering, (c) binarised image with selected particles and (d) original image with detected particles overlayed in red.

The image is binarised, either by simply setting a threshold intensity for the entire image, or by using a local threshold value, taking into account the average intensity of pixels in close proximity. This latter method is more useful for bright field images, where the background intensity is not always constant. Particles are then finally detected by selecting objects with the correct properties, e.g. size, elongation or circularity, from the binarised image and the position, orientation and other relevant properties are determined for each particle using the in-built Mathematica function *ComponentMeasurements*. Figure 2.8 shows each of these steps in the image analysis process for an LSCM image of *fd*-virus particles (top) and a BF image of silica rods (bottom).

2.5.2 Particle tracking

Tracking individual particles through time can give valuable information about the dynamics of a system. To be able to accurately track particles, it is important to record image series at a high frame rate, to avoid confusion of which particle is which in subsequent frames.

Once particle positions have been determined in each frame using the image analysis methods described in the previous section, particles can be tracked through time. In stationary

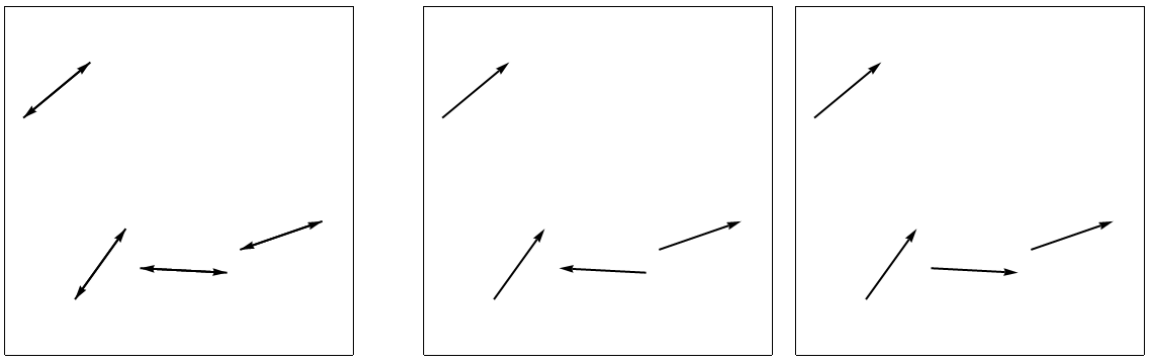
systems, this is often done by simply finding the particle closest to the position found in the previous frame. In flowing systems, an estimated expected position can be determined by taking into account the flow velocity and direction, and the particle closest to this estimated position is selected.

In dilute systems, where there are only a few particles in each frame, it is often easier to combine particle tracking and detection. Instead of finding all the particles in each frame, one simply determines a particle's position in the initial frame, and then crops the next frame around this original position, or an estimated new position in the case of flow, before particle detection. The particle found in this cropped image is then the same particle at its new position. This protocol was checked manually for a number of cases.

2.5.3 Orientations

After particles have been detected, the orientations can be determined easily. As rods are symmetric, there are two possible orientations that can be assigned to each rod, with a difference of π rad between them. For a single particle this causes no problems, but when calculating properties from the orientations of multiple particles, such as the nematic director or the order parameter, care has to be taken to ensure that the orientations of particles are not in opposing directions.

In order to prevent this from happening, we generate vectors pointing in both directions from each rod, and then select two groups of vectors from these, one group of vectors pointing up ($0 \leq \theta < \pi$), and a group of right-pointing vectors ($-\frac{\pi}{2} \leq \theta < \frac{\pi}{2}$). This process is schematically shown in figure 2.9 for randomly generated rods. The relative orientation with respect to the average orientation is then determined for each particle in both groups, and the group of vectors with the lowest variance in relative orientations is then chosen as the set of orientations on which to perform further calculations. It can easily be seen that, even though there is only one rod with a different orientation in figures 2.9(c) and (d), there is quite a large difference in the variance of orientations, which is 1.54 for the upwards pointing vectors, versus 0.19 for the right-pointing vectors.



(a) (b) (c)

Figure 2.9: Schematic representation of the process of choosing the orientation for each particle. (a) The orientations assigned to four rods depicted as vectors, (b) selection of upwards pointing vectors and (c) selection of right-pointing vectors.

2.6 Conclusion

The colloidal systems and experimental methods introduced in this chapter are used throughout this thesis. The *fd*-virus system is used as a model system for colloidal liquid crystals in chapters 3 and 4. The fact that they are monodisperse and very long and thin rods, with an aspect ratio of $L/D \approx 133$, makes them ideal for this purpose. The system is studied using confocal microscopy, which allows us to study individual virus particles in the liquid crystalline phase, and scan the system in three dimensions. Because the virus particles are very small and have a low contrast, observing them using transmission light microscopy is not possible.

The silica rod system is used in flow experiments (chapters 5 and 6). The relatively large size makes them much easier to track than *fd*-virus particles, not only because the rods are easier to observe, but also because the dynamics of large objects are much slower, and therefore easier to study. The silica rod systems are studied using conventional microscopy, where we can observe the dynamics of the system in real time. This is not possible in confocal microscopy, where an image needs to be constructed by scanning a sample pixel-by-pixel, and therefore dynamic processes that happen on a time scale smaller than the scan speed are impossible to study.

We can therefore conclude that both the colloidal rod systems and the two microscopy techniques used are complementary, and in this thesis we use the specific advantages of each to study the behaviour of colloidal rod systems in confinement.

Chapter 3

Direct calculation of distortion energies in colloidal liquid crystals from single-particle data

We report a method to calculate distortion energies of a colloidal liquid crystal from single particle data via a triangulation of the particle positions followed by a linear interpolation of the particle orientations. Our method provides local information on the strength and type of distortions present in a liquid crystal. We validate our method by applying it to artificially generated data and show that the results are in good agreement with exact calculations of the distortion energy. We further illustrate our method by using it on laser scanning confocal microscopy images of the nematic phase of *fd*-virus particles in wedge-shaped microfluidic channels.

3.1 Introduction

The interplay between elasticity, anchoring strength and boundary conditions leads to rich and complex behaviour when confining liquid crystals, see for example recent work by [68, 69, 89–92]. For colloidal liquid crystals the effects of confinement may even be more pronounced with confinement down to the particle level. This raises questions on the applicability of continuum theories, such as Oseen–Frank or Landau–de Gennes theories [26, 44, 45].

One way to explore such questions is by obtaining the director fields from single-particle data and subsequently locally measuring the various elastic contributions. Such data can nowadays be readily obtained by combining colloidal model systems, laser scanning confocal microscopy and soft lithography techniques to confine the liquid crystals [68].

Here, we present a method to directly calculate distortion energies in a liquid crystal from single-particle data, via a triangulation and linear interpolation of particle orientations. Our method provides highly local information on the strength and type of distortions present in a liquid crystal.

This chapter is outlined as follows. We first describe the method for calculating director field distortions in section 3.2. In section 3.3 we will apply our method to artificially generated data and compare the results to exact calculations of the distortion energy. We will continue with an experimental example in section 3.4. Section 3.5 summarises our results and their implications.

3.2 Method

The director field $\vec{n}(\vec{r})$ of a nematic liquid crystal can easily be distorted from its uniform state due to the presence of surfaces, external forces or even by thermal fluctuations. The energy cost associated with any continuous distortion in the director field is given by the Oseen–Frank elastic free energy [44, 45]

$$F_e = \int \mathrm{d}V \left[\frac{K_1}{2} \left(\nabla \cdot \vec{n}\right)^2 + \frac{K_2}{2} \left(\vec{n} \cdot \nabla \times \vec{n}\right)^2 + \frac{K_3}{2} \left(\vec{n} \times \nabla \times \vec{n}\right)^2 \right] \tag{3.1}$$

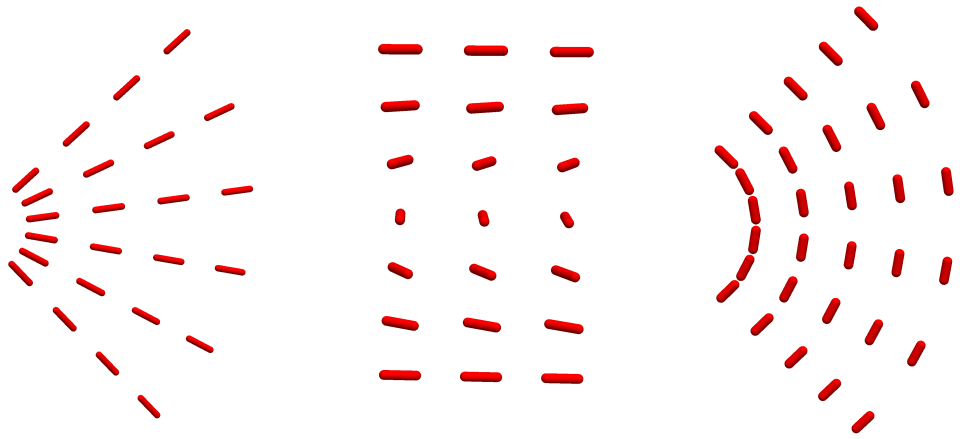


Figure 3.1: Schematic example of the splay (left), twist (centre) and bend (right) deformations in nematic liquid crystals.

where the three terms correspond to the splay, twist and bend deformations respectively, which are schematically shown in figure 3.1, and K_1, K_2 and K_3 are the elastic constants associated with these deformations. Surface terms and the saddle-splay deformation have been neglected.

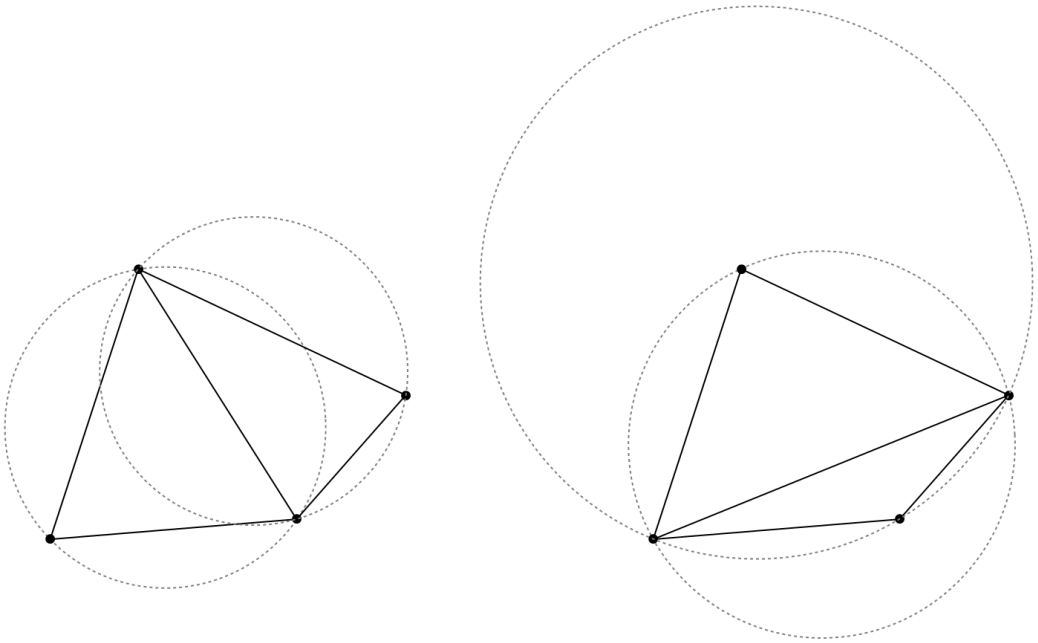
For simplicity we will discuss the 2D case in this chapter, such that we can ignore the second term (twist) in the elastic free energy and the double vector product in the third term reduces to the modulus of the curl of the director field;

$$F_e = \iint \mathrm{d}x\mathrm{d}y \left[\frac{K_1}{2} \left(\nabla \cdot \vec{n}\right)^2 + \frac{K_3}{2} \left|\nabla \times \vec{n}\right|^2 \right]. \tag{3.2}$$

Note that the method can be extended to 3D systems by simply taking into account the full free energy as described in equation (3.1).

In order to calculate the distortion energy from single-particle data, we need to obtain a continuous expression of the director field $\vec{n}$. First, a Delaunay triangulation [93] is performed on the data, using the particle positions as vertices. The Delaunay triangulation breaks up the area into triangles in such a way that if a circle were drawn through the vertices of any triangle, no datapoints other than the three vertices of that triangle can be inside the circle (see figure 3.2). Although in principle any triangulation method can be used, the Delaunay triangulation maximises the sum of the smallest angles and therefore avoids the creation of long and skinny triangles, making it ideal for the interpolation of data [93, 94].

After triangulation, the orientation angle θ, the angle of the local orientation of the director field with respect to an arbitrary reference axis, is linearly interpolated throughout each triangle



(a) (b)

Figure 3.2: (a) A valid Delaunay triangulation, each circle contains only the three vertices of the triangle, and no other datapoints. (b) An invalid Delaunay triangulation; both circles connecting the vertices of the triangles contain a vertex of the other triangle.

using the known orientations at the vertices, as schematically shown in figure 3.3. Extra care needs to be taken for triangles that are are crossed by the reference axis, as in this case there is a 2π jump in θ that needs to be corrected before linear interpolation. This method does require the datapoints to be relatively close together, such that the orientation at the vertices is sufficiently correlated and can be reliably interpolated.

In order to simplify the mathematical description of the interpolation of data in each triangle, we change coordinates from the regular xy-space to $\xi\eta$-space, where ξ and η have directions along the triangle sides and $0 \leq \xi, \eta \leq 1$, as shown in figure 3.4. The continuous descriptions of $\theta(\xi, \eta)$ and the coordinates $x(\xi, \eta)$ and $y(\xi, \eta)$ for any point within the triangle are given by

$$\begin{aligned} \theta(\xi,\eta) &= \theta_1 + \xi(\theta_2 - \theta_1) + \eta(\theta_3 - \theta_1), \\ x(\xi,\eta) &= x_1 + \xi(x_2 - x_1) + \eta(x_3 - x_1), \\ y(\xi,\eta) &= y_1 + \xi(y_2 - y_1) + \eta(y_3 - y_1). \end{aligned} \tag{3.3}$$

Since we can define the director at any point in space as $\vec{n} = (\cos\theta, \sin\theta)$, where θ is a function

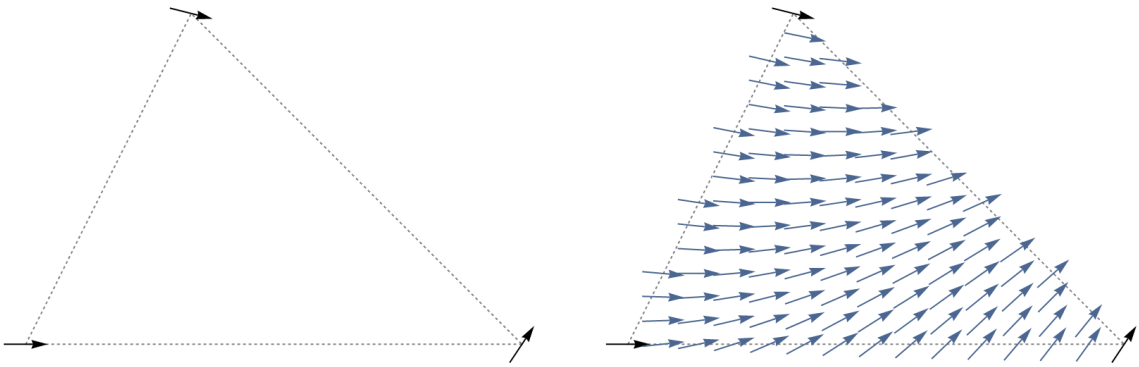


Figure 3.3: Linear interpolation of θ, the angle between the local orientation of the director field and an arbitrary reference axis. On the left the triangle before interpolation, with the known orientation at the vertices indicated as arrows, and on the right the interpolated orientation throughout the triangle.

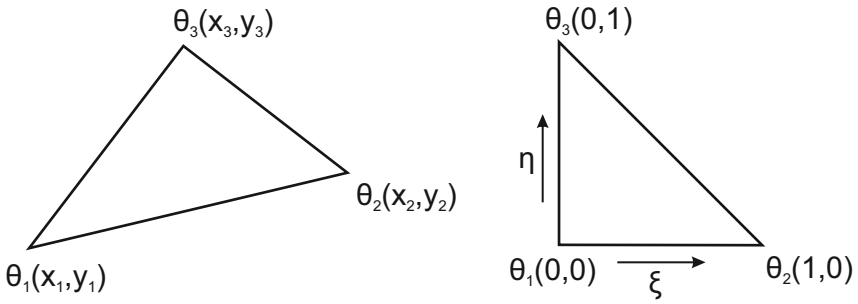


Figure 3.4: Schematics explaining the change from xy-space (on the left) to $\xi\eta$-space (on the right)

of x and y, the derivatives of the director field can be expressed as

$$\nabla \cdot \vec{n} = \cos\theta \frac{\partial \theta}{\partial y} - \sin\theta \frac{\partial \theta}{\partial x}, \tag{3.4}$$

$$|\nabla \times \vec{n}| = \cos\theta \frac{\partial \theta}{\partial x} + \sin\theta \frac{\partial \theta}{\partial y}. \tag{3.5}$$

The different partial derivatives in these two expressions can be calculated using standard differentiation techniques and using the known relation between derivatives

$$\begin{pmatrix} \frac{\partial \xi}{\partial x} & \frac{\partial \xi}{\partial y} \\ \frac{\partial \eta}{\partial x} & \frac{\partial \eta}{\partial y} \end{pmatrix} = \frac{1}{J} \begin{pmatrix} \frac{\partial y}{\partial \eta} & -\frac{\partial x}{\partial \eta} \\ -\frac{\partial y}{\partial \xi} & \frac{\partial x}{\partial \xi} \end{pmatrix}$$

where $J = \left| \frac{\partial x}{\partial \xi}\frac{\partial y}{\partial \eta} - \frac{\partial x}{\partial \eta}\frac{\partial y}{\partial \xi} \right|$ is the Jacobian.

Applying these relations to equations (3.4) and (3.5) gives

$$\begin{aligned} \nabla \cdot \vec{n} =& \frac{\cos\theta}{J}\left[(\theta_3-\theta_1)(x_2-x_1) - (\theta_2-\theta_1)(x_3-x_1)\right] + \\ & \frac{\sin\theta}{J}\left[(\theta_3-\theta_1)(y_2-y_1) - (\theta_2-\theta_1)(y_3-y_1)\right], \end{aligned} \tag{3.6}$$

$$\begin{aligned} |\nabla \times \vec{n}| =& -\frac{\cos\theta}{J}\left[(\theta_3-\theta_1)(y_2-y_1) - (\theta_2-\theta_1)(y_3-y_1)\right] + \\ & \frac{\sin\theta}{J}\left[(\theta_3-\theta_1)(x_2-x_1) - (\theta_2-\theta_1)(x_3-x_1)\right], \end{aligned} \tag{3.7}$$

where of course θ is given by equation 3.3. All terms inside the square brackets are known values of θ, x and y at the three vertices, and the only dependence on η and ξ comes from θ in the sine and cosine terms.

The distortion energy within each triangle can be calculated by simply taking the square of the derivatives given in equations (3.6) and (3.7), for splay and bend distortion energies respectively, multiplying by the corresponding elastic constant $K_i/2$ and integrating over the area of the triangle. This can either be done for the splay- or bend contributions separately, or for the total distortion energy by summing the two terms. The total elastic energy within a triangle is given by

$$F_{e,\triangle} = \iint_{\triangle} \mathrm{d}\xi \mathrm{d}\eta \; J \left[\frac{K_1}{2} (\nabla \cdot \vec{n})^2 + \frac{K_3}{2} (|\nabla \times \vec{n}|)^2 \right], \tag{3.8}$$

where of course the vector field derivatives are given by equations (3.6) and (3.7).

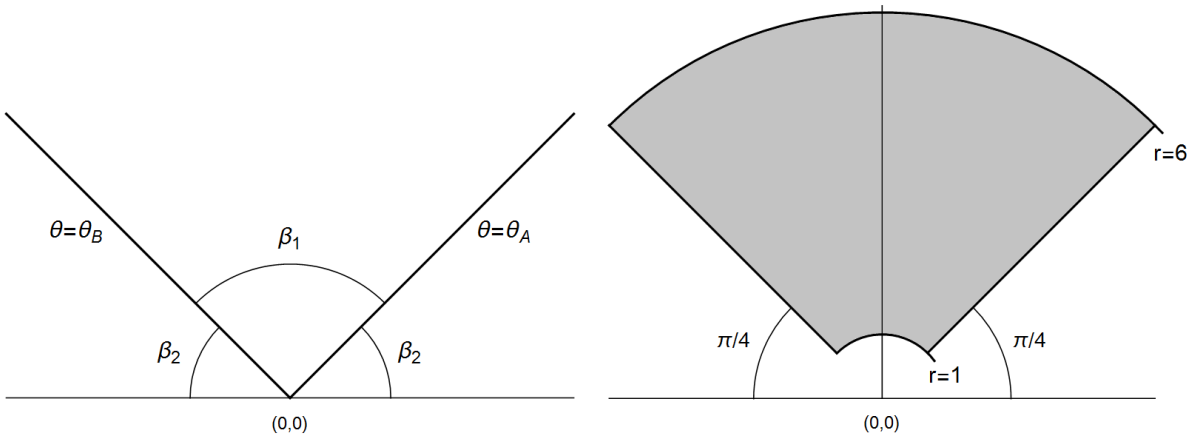


Figure 3.5: (a) Schematic representation of the wedge geometry used to calculate the director fields, and (b) the area in which artificial data was generated.

3.3 Artificial data

To illustrate our method for calculating distortion energies we will discuss an example of the method applied to artificial data, so that we can compare the results to exact calculations of the distortion energy.

The artificial data was generated using an expression for the director field as described in a paper by Mottram et al [95]. Here, the authors solve the Laplace equation in the one-constant approximation $K_i = K$ for a nematic phase confined to an infinite wedge. They assume strong anchoring conditions, such that the orientation of particles at the wall is fixed. The orientation of the director field at any point in the wedge is given by

$$\theta(x,y) = \frac{\theta_B - \theta_A}{\beta_1} \tan^{-1}\left(\frac{y\cos\beta_2 - x\sin\beta_2}{x\cos\beta_2 + y\sin\beta_2}\right) + \theta_A, \tag{3.9}$$

where β_1 and β_2 are the angles defining the shape of the wedge and θ_A and θ_B are the orientations of the director field on the two walls of the wedge. All of these parameters are shown schematically in figure 3.5(a).

In order to simulate experimental data closely, 500 random datapoints were generated within the area indicated in figure 3.5(b). This particular shape was chosen to simplify calculations and to exclude the defect located at the tip of the wedge, which is necessary because the Oseen–Frank elastic energy (equation 3.1) is only valid for continuous director fields. Defects

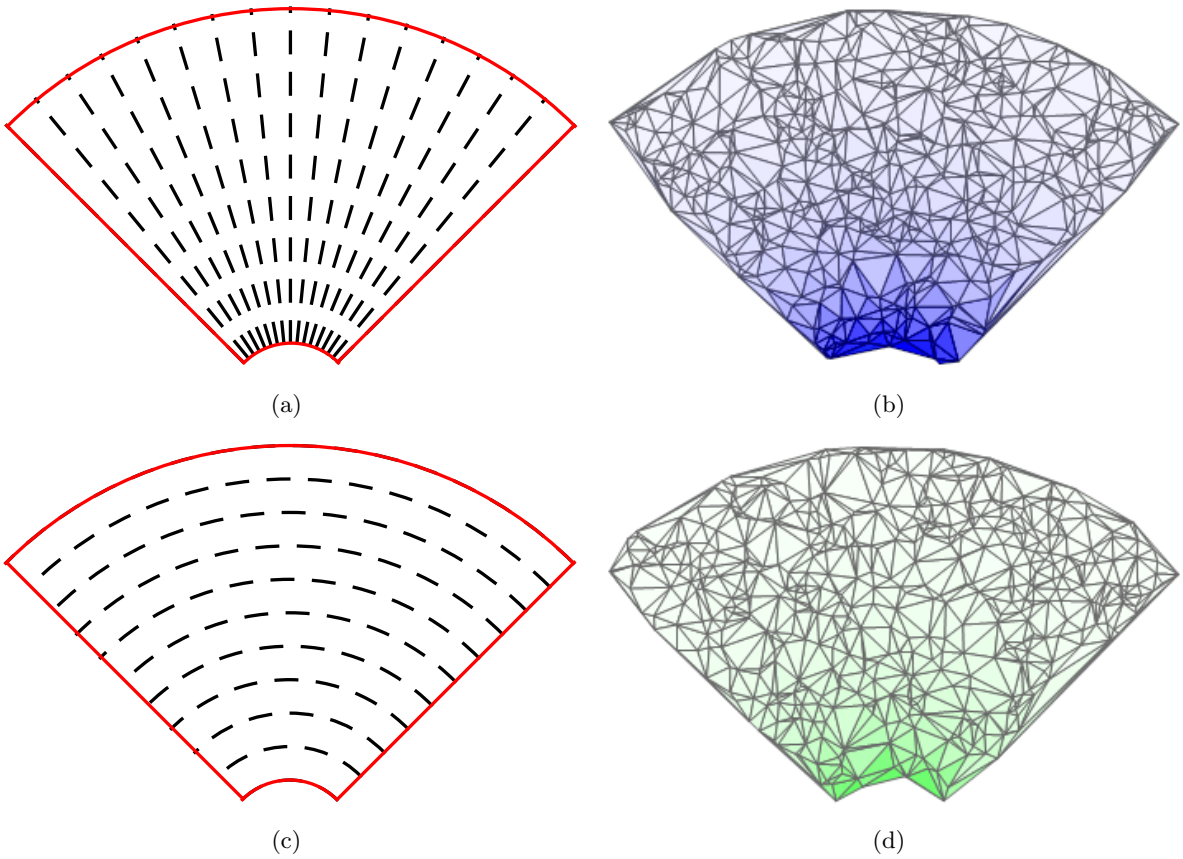


Figure 3.6: Schematic representation of the two director fields used to test our method; (a) a splay-only director field and (c) a bend-only director field, with (b) and (d) the corresponding colour plots indicating the local distortion calculated from artificial data. Triangles in the colour plots are white in the absence of distortions in the director field, the intensities of green and blue increase with increasing bend and splay deformations respectively.

can be easily excluded by removing the datapoints in the defect core region, which has a radius on the order of the nematic correlation length [51]. The energy associated with the defect can then be added to the elastic energy separately.

The orientation of the director field at each generated datapoint was calculated from equation 3.9. Two different datasets were created; one where the director field only has a splay-deformation, corresponding to $\beta_2 = \pi/4$, $\theta_A = \beta_2$ and $\theta_B = \beta_1 + \beta_2$, and one where the distortion is purely of the bend type, with $\beta_2 = \pi/5$, $\theta_A = \beta_2 + \pi/2$ and $\theta_B = \beta_1 + \beta_2 + \pi/2$. The two different director fields are schematically shown in figure 3.6(a) and (c). Note that in the case of the bend-only field, $\beta_2 = \pi/5$ was used to calculate the director field, but datapoints were generated in the region given by $\beta_2 = \pi/4$ as shown in figure 3.5(b).

The distortion energy was then calculated using the triangulation and interpolation method.

	artificial data		exact calculation	
	splay/K_1	bend/K_3	splay/K_1	bend/K_3
splay-only director field	1.23	$4.24{\cdot}10^{-3}$	1.41	0
bend-only director field	$4.34{\cdot}10^{-3}$	1.21	0	1.41

Table 3.1: Distortion energies calculated using artificial data compared to exact calculations for both director fields, which are shown in figure 3.6(a) and (c).

The total distortion energy was also calculated exactly using equation 3.2, where $\vec{n} = (\cos\theta, \sin\theta)$ and θ is given by equation 3.9. The distortion energies found using both methods are summarised in table 3.1.

The distortion energies that we determined for the artificial data are close to the actual values calculated from exact expressions. The (small) difference most probably stems from the fact that the distortion energy cannot be determined close to the edges of the sample, as there are no datapoints on the very edges of the wedge. Note that an increase in number of generated datapoints resulted in calculated values closer to the exact calculations, which further supports this assumption. In this theoretical case the edge problem could be solved by manually placing datapoints on the edge of the region, but in experimental systems the limitation would still exist.

To visualise the distortion energy we have created colour plots that show the triangulation mesh in grey and the extent of splay distortion in blue and bend distortion in green. This makes it easier to quickly see where the director field is most distorted, and which type of distortion is dominating. The results for the two different director fields are shown in figure 3.6(b) and (d). The intensity of both blue and green in the images is adjusted to have maximum intensity for the triangle with the strongest distortion, either splay or bend, found in the image. This was done in order to better visualise the director field distortions. The intensity is therefore not an exact measure of the distortion energy, but splay and bend can be directly compared to each other within the same image.

It can easily be seen from the colour plots that the distortion energy calculated is indeed dominated by splay deformations for the splay-only director field and by bend deformations for the bend-only director field, as expected. Furthermore it is clearly visible that, for both cases, the distortions are strongest towards the narrow part of the wedge, where the director field is most deformed.

3.4 Application to experimental data

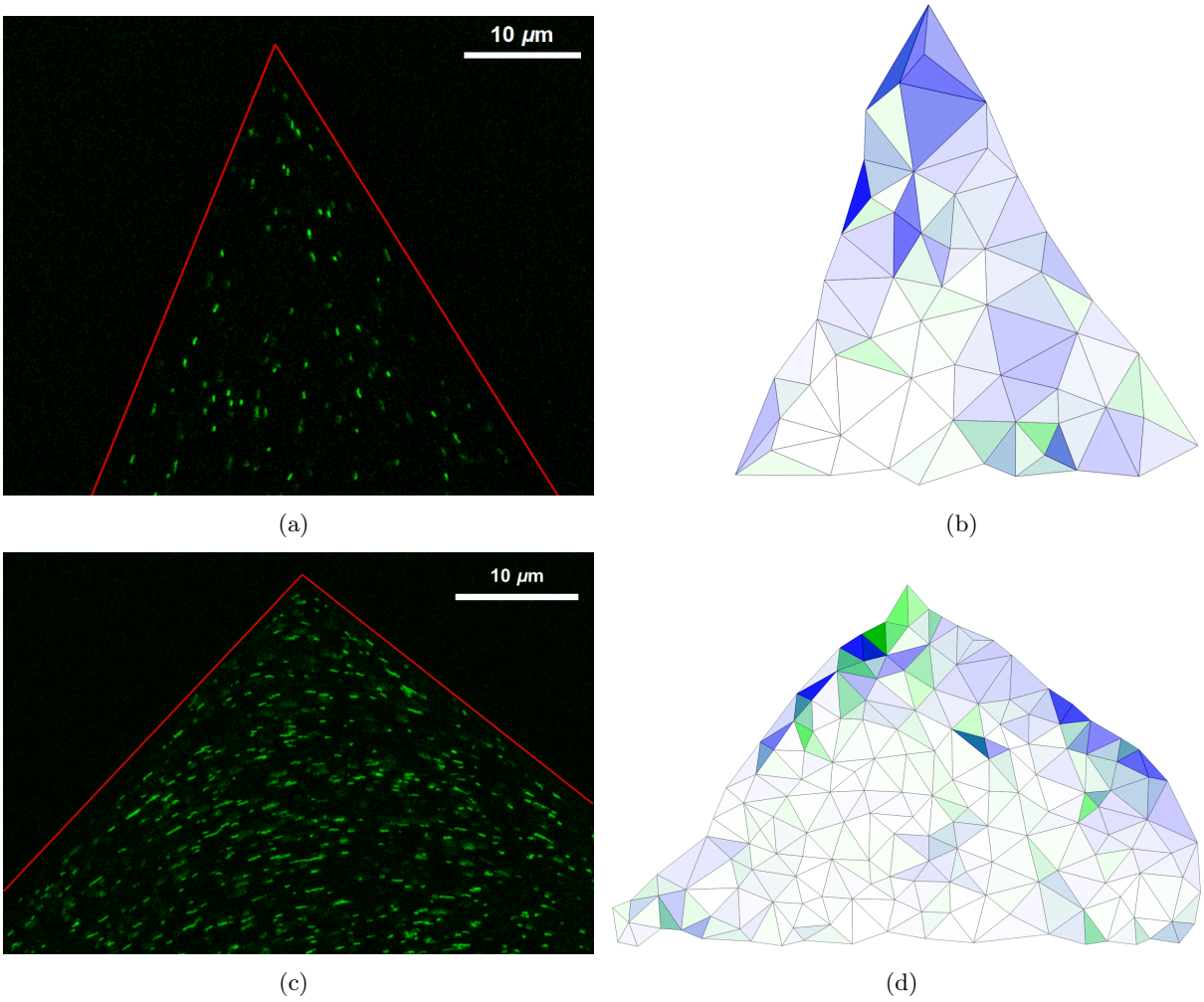
To further illustrate our method we apply it to confocal microscopy images of *fd*-virus particles confined in wedge-shaped microfluidic channels. These rod-shaped viruses, with a length of 880 nm and a width of 6.6 nm, form a cholesteric phase in bulk and are often used as a model system for liquid crystals [96–103]. For a more in-depth discussion of *fd*-virus particles, see section 2.1.1.

Confinement of a liquid crystal, e.g. in microfluidic channels, adds elastic stress to the material. A wall often forces a certain orientation of the particles close to it (anchoring), and when a liquid crystal is confined between two or more such walls, anchoring and distortion energies must compete to determine the configuration of the director field, which is often different from that seen in bulk [69]. It has previously been shown for this particular system that anchoring is very strong and, depending on the opening angle of the wedge, the director field will either form a splay-deformation or a combination of splay and bend deformations [68]. A confocal microscopy image of these two possible configurations is shown in figure 3.7 (a) and (c) in wedges with an opening angle of 60° and 90° respectively [68].

The exact value of the elastic constants K_1 and K_3 are unknown for this system. However, by studying the deformation of the cholesteric phase in wedges with different opening angles it was recently shown that the elastic constants are approximately equal to each other [68]. We can therefore not only qualitatively determine the distortions, but we can also find which of the two distortion types is more prominent in each region of the sample.

We used data obtained from image analysis (see section 2.5) performed on confocal microscopy images for each of the two wedges shown in figure 3.7 to calculate the contributions of bend- and splay deformations in each sample. Approximately 1% of the virus particles was fluorescently labelled to make them visible under the confocal microscope. For both cases data was obtained from short movies of 30 independent frames. Positions and orientations were averaged for particles that were closer together than approximately 2 µm in order to get a more accurate sampling of the director field.

By calculating the distortion energies using the method described earlier we have found that in the wedge with an opening angle of 60° the splay deformation is dominant, and is strongest



(a) (b)

(c) (d)

Figure 3.7: Confocal microscopy images of *fd*-virus particles in wedge-shaped microfluidic channels with opening angles of (a) 60° and (c) 90°. The red lines indicate the location of the channel walls. (b) and (d) the corresponding colour plots of the calculated distortion energies. Triangles in the colour plots are white in the absence of distortions in the director field, the intensities of green and blue increase with increasing bend and splay deformations respectively.

in the tip of the wedge. For the wedge with an opening angle of 90° we found that both splay and bend deformations were present, with the bend deformation being most prominent in the tip of the wedge, and splay deformations along the sides of the wedge. Colour plots for these two wedges, showing the extent of splay deformation in blue and bend deformation in green, are shown in figure 3.7 (b) and (d).

Our triangulation and interpolation method provides very local information on both the strength and type of director field distortions. The colour plots that were created visualise the distortion energy very well, making it possible to quickly see where in a sample distortions are most prominent, and what type of distortions are present.

3.5 Conclusion

We have shown how confocal microscopy data of the nematic phase of single rod-like colloidal particles can be used to locally determine the different contributions from bend and splay deformations. In this particular instance the local position and orientation of each particle needs to be determined, after which an interpolation scheme for the local orientation can be constructed based on a Delaunay triangulation.

One limitation of the method is that it can only be applied to continuous director fields, and will not work for any point defects or disclination lines in the system because the Oseen–Frank elastic free energy does not account for these. If only a small number of defects or disclination lines are present, a general idea of distortions can still be obtained by simply omitting the region containing the defect, as we showed for the artificial data in section 3.3.

The method we have presented is applicable to a wide range of problems in soft matter where a continuous expression needs to be obtained from a discrete dataset, such as particle image velocimetry or calculation of the bond orientational order parameter Ψ_6. Although we have only discussed equilibrium director fields, our method can also be applied to non-equilibrium situations or flowing liquid crystals, as long as the director field orientation in different datapoints can be reliably interpolated. The method can also easily be extended to 3D systems, if the orientations of particles can be accurately determined in 3D, by simply taking into account the full distortion energy given in equation 3.1. The Delaunay triangulation will then result in tetrahedra, for which a linear interpolation can be done in a similar way as for the 2D case.

In systems where the elastic constants K_i are not known exactly a quantitative result for the distortion energy cannot be obtained. However the method can still be used to qualitatively determine the distortion energy and for example compare samples as a function of confinement.

Acknowledgements

We thank Oli Dammone for providing the experimental data from [68].

Chapter 4

Capillary nematisation of colloidal rods in confinement

We confine a colloidal liquid crystal between parallel plates separated down to several times the rod length. We study the sample in both a canonical system and a grand canonical system, which is created by connecting the sample between parallel plates to a reservoir. In both cases we find that upon strong confinement the sample becomes nematic between the parallel plates. This capillary nematisation transition can be followed down to the single particle level by means of laser scanning confocal microscopy. We compare the experimental findings to the Zwanzig model as well as a more advanced density functional theory, in which the effect of rod flexibility is taken into account. Finally, we discuss the wetting behaviour at a single wall for which we find a discrepancy between experiment and theory.

4.1 Introduction

Phase behaviour of liquid crystals (LC) in confinement is of ongoing interest both from a fundamental point of view, to obtain a better understanding of the interplay between bulk properties and wall-induced effects, and for applications such as LCDs, where there is an ongoing trend towards smaller cells. Recently, interest in lyotropic liquid crystals in confinement has greatly increased, leading to theory [69, 91, 104], experiments [69, 90, 105] and simulations [106–108] in order to better understand effects of confinement, where LC-wall interactions lead to different behaviour than in bulk.

Lyotropic liquid crystals are particularly interesting as a model system for biological processes, as many of the cell structures, e.g. membranes and filaments, exhibit liquid crystalline properties [109,110]. As a cell is a very small and crowded environment, the phase behaviour of many of these structures will be affected by confinement [111]. It has been shown, for example, that cytoskeletal filaments will form bundles due to confinement and, in mixtures of filaments, will segregate based on the flexibility of the different filaments [112, 113].

Here, we study the isotropic phase of a colloidal liquid crystal in confinement and particularly focus on the capillary nematisation phenomenon, where the confined nematic phase becomes stable at a concentration below the bulk isotropic-nematic phase coexistence, similar to capillary condensation in simple fluids. When rods in an isotropic phase are confined between walls, it becomes entropically favourable to align their major axis along the walls, increasing the accessible space. The walls will induce a nematic wetting layer close to the wall, despite the concentration being below the isotropic-nematic transition in bulk. When the distance between walls is sufficiently small even an isotropic-to-nematic phase transition throughout the sample may be observed. This phenomenon was first predicted by Sheng [114] and later by Poniewierski and Sluckin [115]. Capillary nematisation has experimentally been confirmed for thermotropic liquid crystals by measuring the force profile originating from confining a molecular liquid crystal between a wall and a colloidal sphere attached to an atomic force microscope [116]. For lyotropic liquid crystals, capillary nematisation has been studied in theory and simulations, see e.g. [104, 117–124], however, direct experimental visual confirmation of capillary nematisation for lyotropic liquid crystals has not yet been reported.

In this chapter we experimentally show a capillary nematisation transition in a colloidal

liquid crystal, using dispersions of *fd*-virus particles in microfluidic channels of different heights. We observe a clear capillary transition in qualitative agreement with calculations based on the Zwanzig model, in which rods can only have three different directions. A more advanced density functional theory, in which rods may point along any direction and in which the flexibility of the rods has been taken into account, shows more quantitative agreement to the experiments. The theoretical predictions furthermore shine light on the possibility of experimentally observing wetting layers.

4.2 Experiment and results

We dispersed *fd*-virus particles, grown using standard methods described in [17], in 20 mM TRIS-HCl buffer at pH 8.2 with 100 mM NaCl and 15% ethanol. These virus particles are rod-shaped, with a length of 880 nm, a diameter of 6.6 nm and a persistence length of 2200 nm, and are commonly used as a model system for liquid crystals [97–100, 102, 103]. For a more detailed description of *fd*-virus particles, see section 2.1.1. The isotropic phase was isolated from an isotropic-nematic biphasic system and then either used as such, or diluted to 90% (w/w) or 99.5% (w/w) of the coexistence concentration of the isotropic phase in bulk, depending on the experiment. This was done to ensure that the sample is completely isotropic in bulk, yet very close to the bulk isotropic-nematic phase transition, so that capillary nematisation can be achieved with a relatively small degree of confinement. A small portion of the virus particles was fluorescently labelled with Alexa-488 NHS ester. The samples were studied with laser scanning confocal microscopy (LSCM) using a Zeiss LSM 5 Exciter, 63x 1.4 NA oil-immersion objective.

Straight, unbranched microfluidic channels with different heights between 1 µm and 12 µm (roughly $1.1 - 13.6\ L$, where L is the length of a rod) and either a width of 560 µm and a length of 7 mm or a width of 300 µm and a length of 18 mm were created in NOA81 UV glue using the method described in section 2.2. In the case of 7 mm long channels, each channel was placed in a glass vial, such that the vial acts as a reservoir from which particles can freely enter or leave the channel, effectively creating a grand canonical system. A schematic representation of this grand canonical sample cell is shown in figure 4.1. The addition of a reservoir is necessary for capillary nematisation to occur, as the phase transition leads to an increase of the concentration inside the channel, which can only occur if there is a reservoir of rods, from which particles can

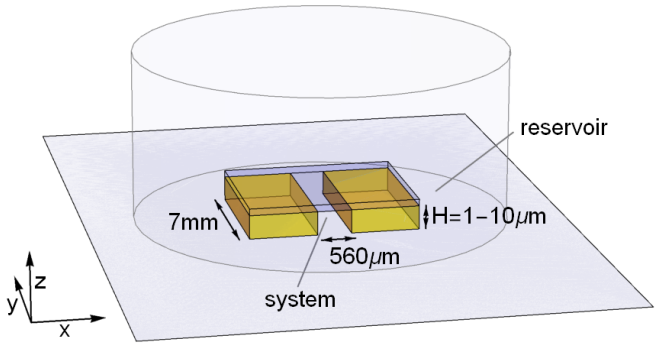


Figure 4.1: Schematic representation of the sample cell with reservoir. The micro-channel itself is in between the two yellow blocks, which represent UV glue. The channel is closed on both top and bottom by a coverslip, and the entire channel is enclosed in a small glass vial, glued onto the bottom coverslip.

be drawn into the channel. The 18 mm long channels were sealed at both ends after adding the sample, creating a canonical system.

The channels were plasma-cleaned and subsequently filled via capillary action by adding approximately 50 µL of the sample per channel (grand canonical) or 2 µL per 9 channels (canonical) to one end of the channel(s). Only a very small amount of sample was required to fill the channel, and in the case of the grand canonical system, the rest of the sample was left at the end of the channel (but inside the glass vial) and acted as a particle reservoir. In the canonical system, the channels were sealed at both ends using UV glue after filling the channels. Although these channels do not have a reservoir, the amount of sample used was larger than what is required to fill the channel, and therefore the excess fluid can act as a reservoir of small but unknown size during the filling process. We found no signs of particles sticking to the confining walls.

LSCM images were recorded for the samples in channels of different heights in order to determine the phase behaviour. Time series were recorded in the xy-plane at $z = 0$, halfway in height between the two confining walls, such that any nematic phase seen must be a capillary nematic state, and not a nematic wetting layer at the walls. In order to see whether nematic wetting layers are indeed present at the wall in the experiment, LSCM images were recorded at different heights throughout a channel, with a z-resolution of 0.2 µm (i.e. 0.2 L) between frames.

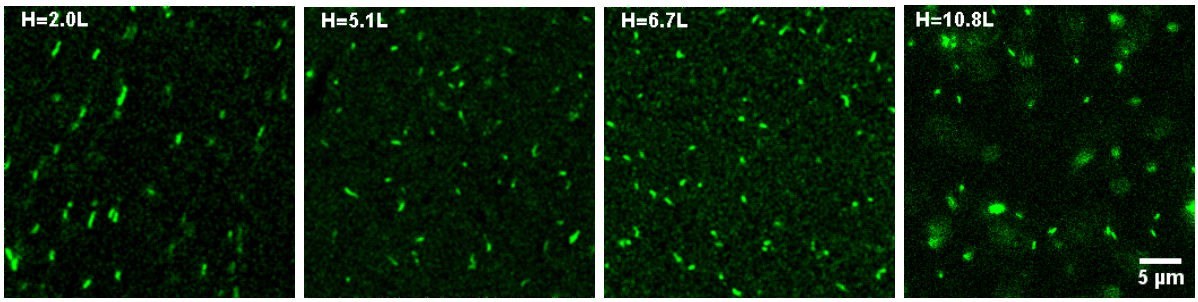
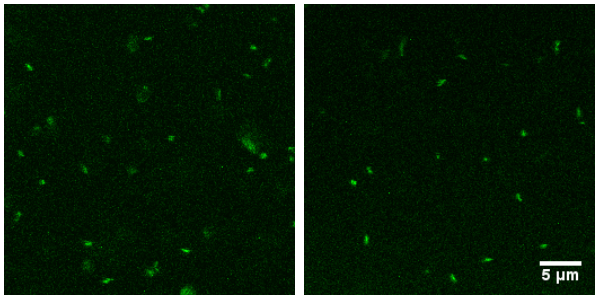


Figure 4.2: LSCM images of *fd*-virus particles in microfluidic channels of different heights (2.0, 5.1, 6.7 and 10.8 L) in the grand canonical system. Each image is a superposition of 5 frames, to increase the number of particles per image.



(a) (b)

Figure 4.3: LSCM images of *fd*-virus particles at the top (left) and bottom (right) wall of a microfluidic channels with a height of 5.1 L.

4.2.1 Grand-canonical system

The isotropic phase taken from a biphasic sample was diluted to 99.5% (w/w), to ensure that the sample is completely isotropic in bulk. Channels with heights of 2.0, 5.1, 6.7 and 10.8 L were used in these experiments.

Figure 4.2 shows typical LSCM images recorded in the middle of a channel ($z = 0$) for each of the channel heights used. The sample remains isotropic down to a confinement of 5.1 L. However, when confined to channel with wall-to-wall separation of 2.0 L, the particles become aligned and the system displays a nematic phase. No nematic wetting layers were seen in any of the isotropic samples. As an example, figure 4.3 shows the images recorded at each of the walls for a channel with a height of 5.1 L.

In order to quantify the results, the order parameter S was calculated for each sample using

$$S = 2\left\langle \cos^2 \theta' \right\rangle - 1, \tag{4.1}$$

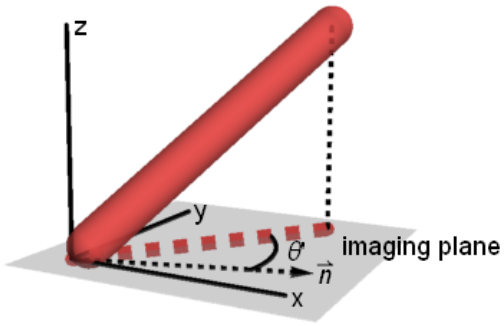


Figure 4.4: The angle θ' measured from confocal images is the angle between the projection of the rod on the imaging plane (red dashed line) and the average orientation of rods $\vec{n}$.

where θ' is the orientation of a particle projected on the imaging plane, as we measure it from our confocal images, with respect to the average projected orientation of all particles in that frame (see figure 4.4). Because we can only measure this projected angle, and not the full 3D angle, the order parameter equivalent to that of a 2D system should be used, which has been shown to be a good estimate of the 3D order parameter [125].

The order parameter for each time series, recorded in the middle of the channel in terms of height, was calculated. As there are relatively few particles per frame, particles from 10 independent frames were combined before calculating the order parameter, leading to an average of 200 or more tracked particles per calculation. This was done for at least 5 time series of 10 frames and then averaged for each channel height. The result is shown in figure 4.5. The order parameter for the channel with $H = 2.0\ L$ was found to be 0.73, which is clearly much higher than the order parameter found in the bigger channels, which was typically around 0.1. This indicates that capillary nematisation has indeed occurred in the smallest channel. We furthermore note that the nematic director is oriented along the length of the microfluidic channel (y-direction), due to the anchoring conditions on the bounding walls.

The order parameter calculated for LSCM images recorded at different heights in a channel was not found to change significantly throughout the channel for any of the channel heights. Figure 4.6 shows an example of the order parameter calculated at different heights for a channel with a height of 5.1 L.

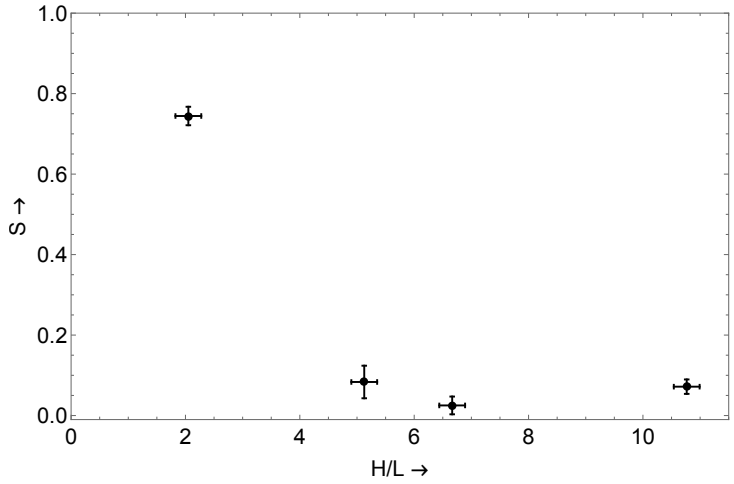


Figure 4.5: Order parameter in the grand canonical sample versus the height of the channel. Error bars represent the standard deviation.

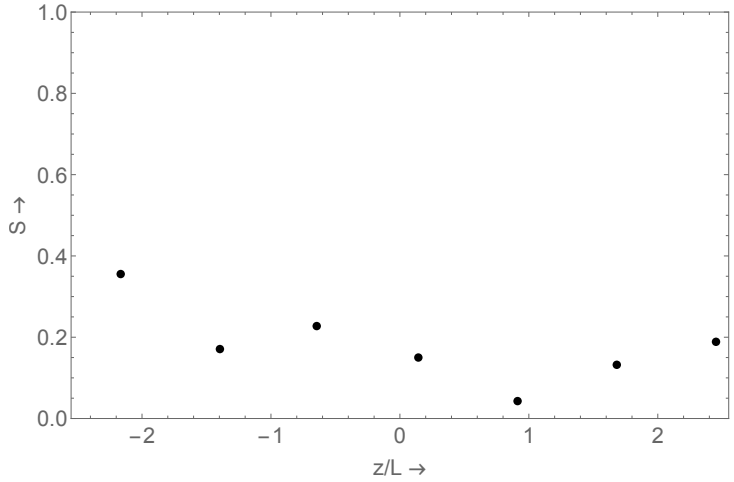


Figure 4.6: Order parameter at different heights throughout a channel, for a channel height of 5.1 L.

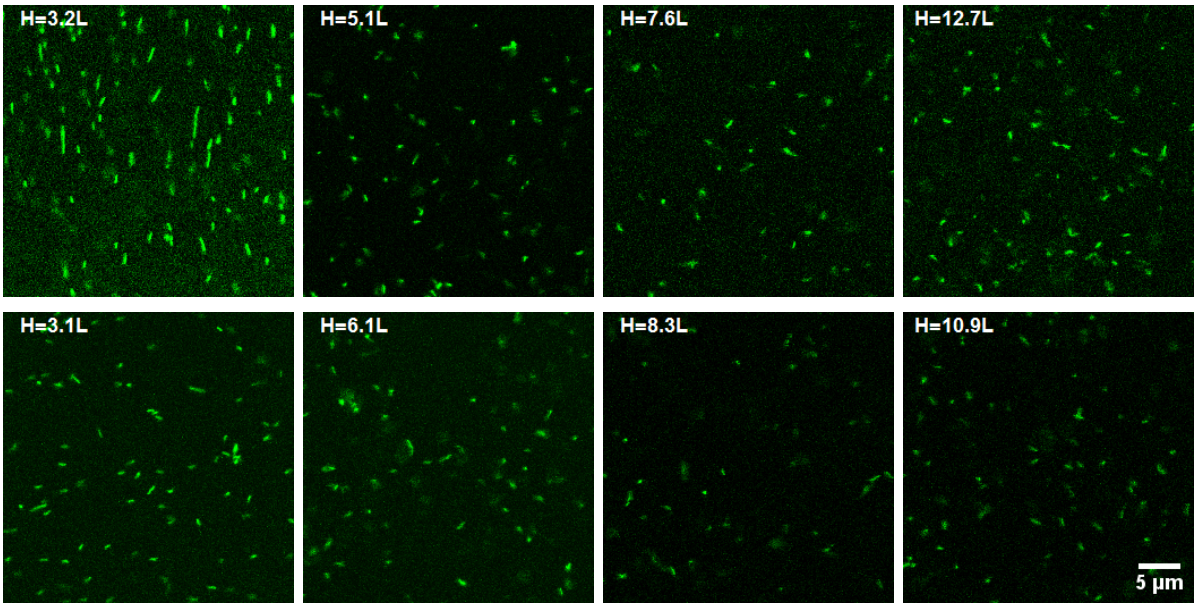


Figure 4.7: LSCM images of *fd*-virus particles in microfluidic channels of different heights in the canonical system, for a concentration of an isotropic phase at coexistence (top) and diluted to 90% (bottom).

4.2.2 Canonical system

Experiments in the canonical system were performed to study the effect of concentration on capillary nematisation. The experiments were done in a canonical system simply because they were performed before the grand canonical system was designed. The isotropic phase isolated from a biphasic sample was either used as such, or diluted to 90% of the original concentration. Different channel heights between 2–12 µm ($2.3 - 13.6\ L$) were used in these experiments. Due to the nature of the channel fabrication process, the channels used are not exactly the same height for both samples.

Figure 4.7 shows typical LSCM images recorded in the middle of a channel ($z = 0$) for each of the channel heights used. It can be seen that the sample is isotropic in all cases except for the higher concentration sample in a channel of 3.2 L, where the particles are more aligned. As with the grand canonical sample, no nematic wetting layers were seen in any of the isotropic samples.

The order parameter S was calculated for each image series, taken in the centre of a channel in terms of height, using equation 4.1. The resulting order parameters are shown in figure 4.8. The order parameter was found to be 0.76 in the channel for the capillary nematisation had

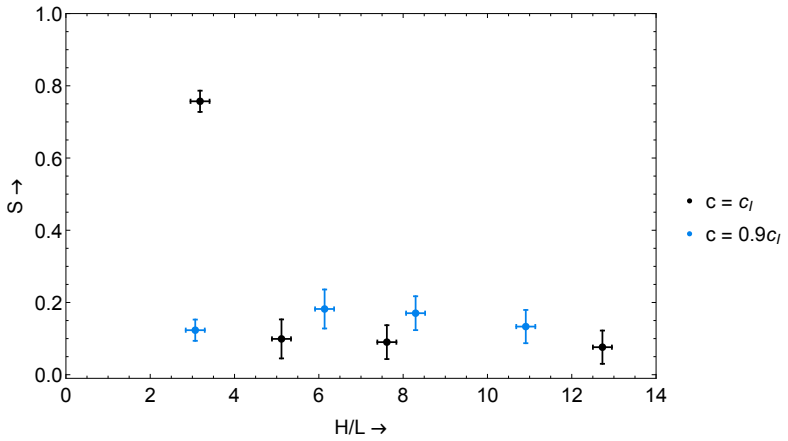


Figure 4.8: Order parameter in the canonical system plotted versus the height of the channel for a concentration of the isotropic phase at coexistence (black) and diluted to 90% (blue). Error bars represent the standard deviation.

occurred, and around 0–0.2 for the other channels. As with the grand canonical system, the order parameter was not found to change significantly at different heights throughout a channel.

The fact that capillary nematisation occurs in the smallest channel for a sample with a concentration of the isotropic phase at coexistence, but not in the sample which was diluted to 90% indicates that it is indeed capillary nematisation, and not for example a filling effect of the smaller channels that aligns the rods along the direction of the channel. The sample stays isotropic in the bigger channels even for a concentration at coexistence, which is an indication that we indeed have a finite-sized reservoir.

4.3 Zwanzig model

We will first compare our results to theoretical calculations using the Zwanzig model [126]. This is one of the simplest models in which rods are considered to be rectangular blocks of $L \times D \times D$, with $L \gg D$, that can only be oriented along one of three perpendicular unit vectors $\hat{x}_i$. The positions of the rods are continuous. This model has been shown to give qualitatively accurate results for the isotropic-nematic transition [126] and confinement phenomena [117, 118] of hard rods. Although calculations for the capillary nematisation transition have been performed previously using the Zwanzig model, here we calculate the phase diagram corresponding to our exact system, using the dimensions of rods and confinement used in the experiments.

We base our calculations on a paper by van Roij et al. [118], where the equilibrium phase behaviour for Zwanzig rods confined between two parallel plates is calculated in a grand canonical ensemble by minimising the grand potential function $\Omega(c)$, where $c = L^2 D\rho$ is the dimensionless number density, with ρ the actual number density. Each of the three possible orientations $\hat{x}_i$ is considered to be a different phase, with number densities $c_i(z)$, where z is the direction perpendicular to the confining walls, with $z = 0$ being at the centre of the channel. A hard wall-rod interaction is incorporated as external potentials $V_i(z)$ and the separation between the two walls is H in units of particle length.

The rescaled grand potential function for this system is given by

$$\begin{aligned}\frac{\beta\Omega(c)L^2D}{A} = \Sigma_{i=1}^{3} \int \mathrm{d}z\ c_i(z)(\log c_i(z) - 1 - \beta\mu(c_R) + \beta V_i(z)) \\ + 2\int \mathrm{d}z(c_1(z)c_2(z) + (c_1(z) + c_2(z))\,\bar{c}_3(z)),\end{aligned} \tag{4.2}$$

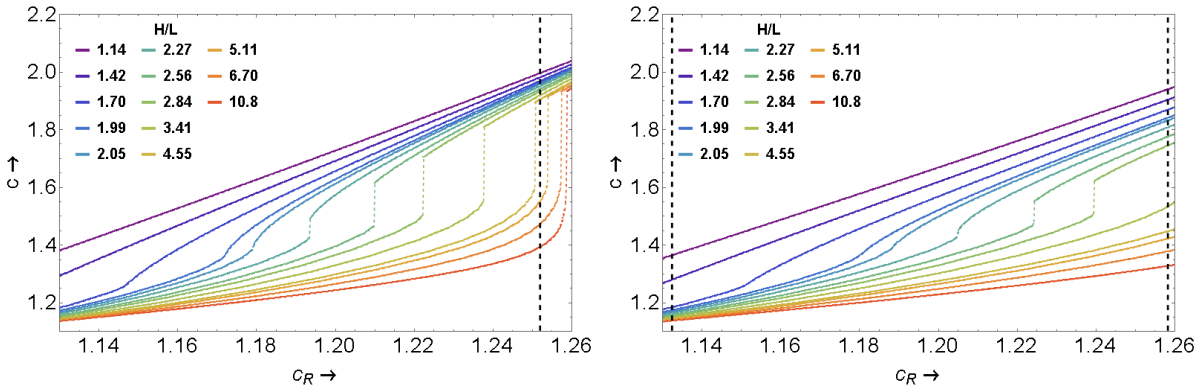
where A is the area of the confining walls, $\beta = 1/k_BT$, $\bar{c}_i(z) = \frac{1}{L}\int_{z-L/2}^{z+L/2} \mathrm{d}z' c_i(z')$ and $\mu(c_R)$ is the chemical potential, with c_R the concentration of rods in the particle reservoir. The Euler-Lagrange equations, obtained from the minimisation conditions $\partial\Omega(c)/\partial c_i(z) = 0$, are

$$\ln c_1(z) = \beta\mu(c_R) - \beta V_1(z) - 2c_2(z) - 2\bar{c}_3(z), \tag{4.3}$$

$$\ln c_2(z) = \beta\mu(c_R) - \beta V_2(z) - 2c_1(z) - 2\bar{c}_3(z), \tag{4.4}$$

$$\ln c_3(z) = \beta\mu(c_R) - \beta V_3(z) - 2\bar{c}_1(z) - 2\bar{c}_2(z). \tag{4.5}$$

The Euler-Lagrange equations are solved iteratively to obtain the equilibrium particle densities $c_i(z)$. In order to simulate a finite reservoir, c_R and μ are re-evaluated at each iterative step, based on the total particle density inside the channel, c, and the starting reservoir concentration $c_{R,0}$, assuming the volumes of reservoir and channel are constant. The total volume V_{tot}, of reservoir and channel together, was set to (i) 50 µL, in agreement with the grand canonical experiments, or (ii) 2/9 µL, which is approximately what was added to each channel in the canonical systems before sealing them.



(a) $V_{tot} = 50\,\mu L$ (b) $V_{tot} = 2/9\,\mu L$

Figure 4.9: Phase diagrams calculated using the Zwanzig model for (a) $V_{tot} = 50\,\mu L$, as used in the grand canonical system, and (b) $V_{tot} = 2/9\,\mu L$, as estimated for the canonical system. Each line represents a different channel height H. Plotted is the density inside the channel versus the density in the reservoir. The vertical dashed lines indicate the reservoir concentrations used in the experiments.

The total concentration of rods $c(z)$ and orientational order parameters $s(z)$ and $\Delta(z)$ were then calculated using

$$\begin{aligned} c(z) &= c_1(z) + c_2(z) + c_3(z), \\ s(z) &= \frac{c_3(z) - \frac{1}{2}\left(c_1(z) + c_2(z)\right)}{c(z)}, \\ \Delta(z) &= \frac{c_1(z) - c_2(z)}{c(z)}. \end{aligned} \tag{4.6}$$

The order parameters are chosen such that for an isotropic phase $s(z) = \Delta(z) = 0$, and for a perfect nematic with the director parallel to the walls $\Delta(z) = \pm 1$ and $s(z) = -\frac{1}{2}$. For a more detailed discussion of these two order parameters the reader is referred to [118]. Note that the experimental order parameter S should be compared to $\Delta(z)$, not $s(z)$.

The average concentration inside the channel, $c = \frac{1}{H}\int_{-H/2}^{H/2} \mathrm{d}z\; c(z)$, was calculated for many different starting concentrations $c_{R,0}$ and wall separations H. The phase diagrams shown in figure 4.9 were created by plotting c against c_R for each of these calculations. Each line in the phase diagram corresponds to a different wall separation H.

In both phase diagrams, a capillary nematisation transition occurs for approximately $H \gtrsim 2\ L$ at a certain value of c_R, where the concentration inside the channel jumps to a higher value. From calculations of the order parameters we confirmed that this is indeed an isotropic-nematic phase transition. For smaller H there is no phase transition visible, as in this case the sample

inside the channel will be nematic even at very low c_R. The difference between the two phase diagrams is most obvious in the difference in concentration, c, between the isotropic and capillary nematic phases, which is much smaller for the smaller reservoir size. In addition, a higher c_R is required for capillary nematisation to occur in the smaller reservoir size for the same wall-to-wall distance H. Both of these differences can be explained by the fact that for a smaller reservoir, a small change in concentration due to particles from the reservoir entering the channel when capillary nematisation occurs, will have a larger impact on the concentration of particles in the reservoir itself.

In the experiments we used a starting reservoir concentration that was 90%, 99.5% or 100% of the concentration of a bulk isotropic phase that is in coexistence with a nematic phase. In the Zwanzig model the isotropic phase in coexistence with a nematic phase has a concentration of $c_I = 1.258$ [118]. The experimental concentrations therefore correspond to $c_{R,0} = 1.132$, 1.252 and 1.258 respectively in the Zwanzig model. The experimental reservoir concentrations are indicated in figure 4.9 with dashed vertical lines.

It can be seen that for the grand canonical system (figure 4.9(a)) at the experimental concentration, capillary nematisation is expected to occur for $H \lesssim 4.7\ L$. Given the approximate nature of the model this corresponds remarkably well with our experiments, where we found capillary nematisation to occur in a channel with $H = 2.0\ L$, but not in a channel with $H \geq 5.1\ L$. In the case of the canonical system (figure 4.9(b)) capillary nematisation occurs at $H \lesssim 3.3\ L$ for the undiluted sample, and at $H \lesssim 1.5\ L$ for the sample diluted to 90%. Again, this corresponds very well with our experiments, where we observe a phase transition between $H = 3.2\ L$ and $H = 5.1\ L$ for the undiluted sample, and do not observe capillary nematisation in any channel heights down to $H = 3.1\ L$ for the diluted sample.

The concentration and order parameters in the centre of the channel, at $z = 0$, were calculated for different wall separations in order to compare this to our experimental order parameters. Figure 4.10 shows a plot of these calculations for each of the three systems, as well as a plot of $|\Delta|$ together with the experimental order parameters S. A sharp phase transition can clearly be seen for both concentration and order parameters in each of the three graphs on the left. For the grand canonical system the transition happens at approximately $H = 4.7L$. In the canonical system the transitions are at $H = 1.6L$ and $H = 3.3L$ for the concentrations of 90% and 100% respectively. This corresponds well with our experiments, where the order

parameter shows a transition at a similar level of confinement.

In each of the three graphs on the left in figure 4.10, we can see that although c and Δ have a sharp transition upon capillary nematisation, s goes to zero much more slowly. Equations 4.6 tell us that this means that in this region $c_1 = c_2 > c_3$, or in other words, the concentration of rods with an orientation perpendicular to z, the direction of confinement, is actually smaller than the concentration of rods with the other two possible orientations. The confining walls clearly disfavour rods that are oriented perpendicular to them, even at a wall distance far beyond the capillary nematisation transition. This effect would of course be smaller in a system where all orientations are possible. It is not possible to determine whether this effect occurs in our experiments, as we only image the xy-plane, and do not know the exact three-dimensional orientation of the rods.

In order to check for nematic wetting layers at the walls, the concentration $c(z)$ and order parameters $s(z)$ and $\Delta(z)$ were calculated as a function of z for several different wall separations H, using $c_{R,0} = 1.252$ and $V_{tot} = 50\,\mu\text{L}$, which is equivalent to our grand canonical experiment. As an example, figure 4.11 shows a plot of these three values for a wall separation of $H = 4.5\ L$. Both the concentration of rods as well as the order parameters clearly show a nematic wetting layer close to the wall, and an isotropic phase in the centre. As discussed earlier, this was not seen in any of our experiments.

One possible explanation for this could be that the thickness of the wetting layer is smaller than the axial resolution of the confocal microscope (see section 2.3.1), and therefore cannot be resolved. Another reason could be that the flexibility of the *fd*-virus particles, which was not incorporated in the Zwanzig model, prevents such a wetting layer from forming.

4.4 Density Functional Theory

Note: The DFT calculations were performed by Professor S.A. Egorov from the University of Virginia.

Although the concentration at which capillary nematisation occurs agrees well between Zwanzig theory and experiments, the exact value of the order parameter shows a discrepancy between the two (see figure 4.10). It is possible that this discrepancy is caused by the relative

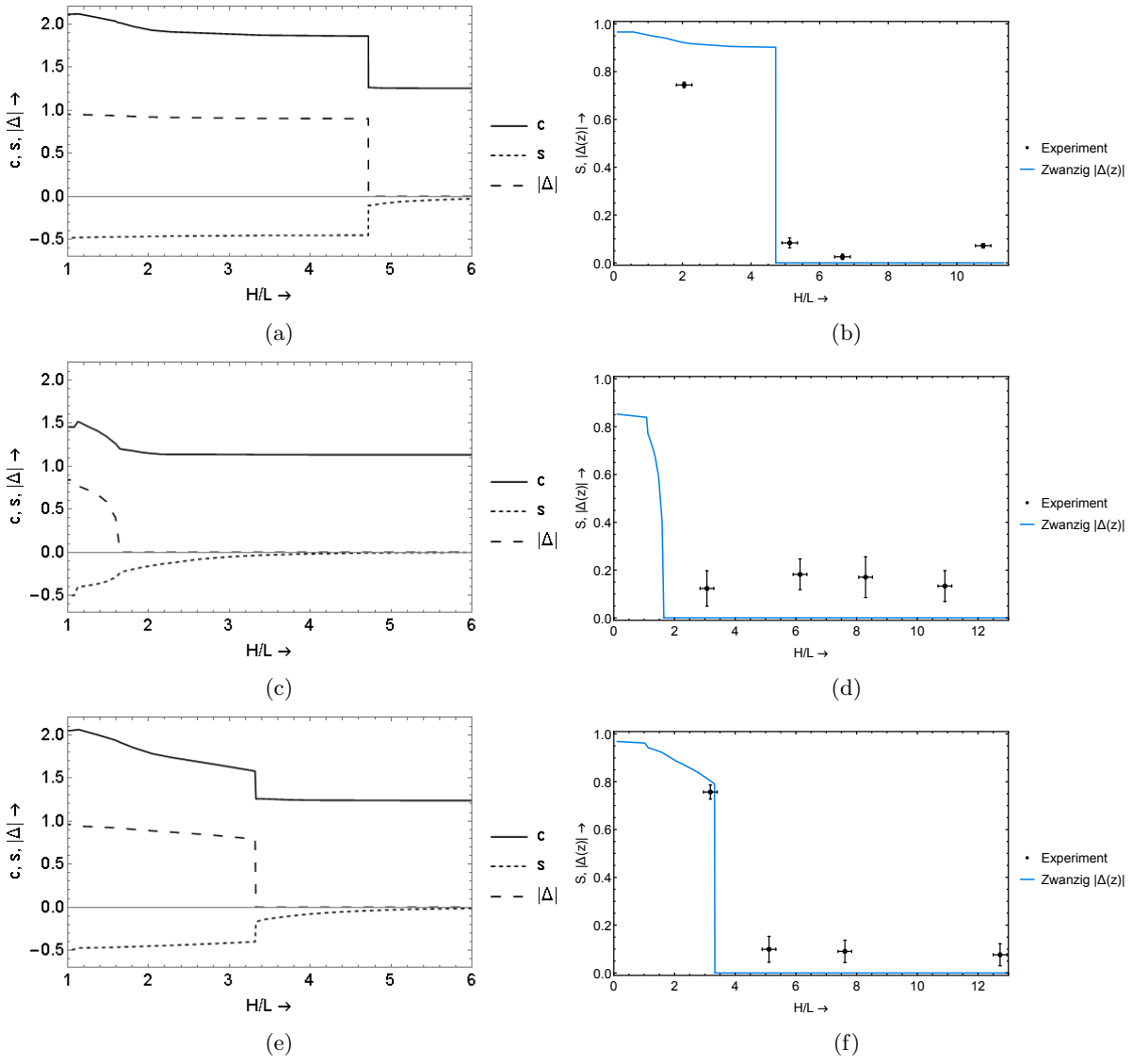


Figure 4.10: On the left; concentration and order parameters in the centre of a channel as a function of channel height H/L, calculated with the Zwanzig model (a) using $c_{R,0} = 1.25193$ and $V_{tot} = 50\,\mu\text{L}$, (c) using $c_{R,0} = 1.13240$ and $V_{tot} = 2/9\,\mu\text{L}$ and (e) using $c_{R,0} = 1.25822$ and $V_{tot} = 2/9\,\mu\text{L}$. On the right; corresponding comparison between $|\Delta|$ and the experimental order parameter for each system.

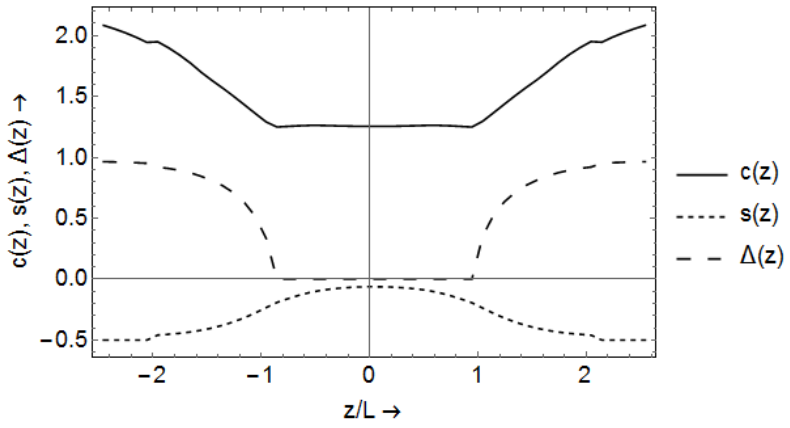


Figure 4.11: Calculated concentration $c(z)$ and order parameters $s(z)$ and $\Delta(z)$ for a channel of $H/L = 4.5$. In the center of the channel ($z = 0$) the rods form an isotropic phase, along the edges of a channel a nematic layer is formed.

simplicity of the Zwanzig model, where only three orientations are allowed and the flexibility of rods is not taken into account. We therefore performed additional theoretical calculations with a different version of the Density Functional Theory (DFT), which has been recently developed specifically to study semi-flexible polymers confined between flat walls [127].

The two key novel features of this alternative DFT approach, which distinguish it from the Zwanzig model discussed above, are (1) the *finite flexibility* of the rods, incorporated in the microscopic model via a stiffness parameter, and (2) the *unrestricted* angular orientations of the rods, achieved by implementing DFT in continuous space, i.e. off-lattice. While it is clearly crucial to account for the finite flexibility of the *fd*-virus particles used in the experiments, the unrestricted orientation is equally important for the present problem, since lattice-based treatments of capillary nematisation are known to suffer from lattice artefacts [120]. Accordingly, it is of interest to compare the results of this new DFT method both with the lattice-based Zwanzig model and the experiment.

In brief, our microscopic description of a semi-flexible rod is based on a tangent hard-sphere model, where a rod is represented as a linear chain of hard spheres. The flexibility of a rod is controlled via the stiffness parameter, which determines the bond-bending potential between spheres. The confinement is incorporated via two hard flat parallel walls in the xy-plane, separated by distance H along the z-axis. As usual, the DFT approach is based on minimising the free energy of the system and produces the equilibrium density distribution, which is both spatially and orientationally inhomogeneous. By integrating over the angular variables, the order parameter of the system $S(z)$ is obtained as a function of the distance from the confining

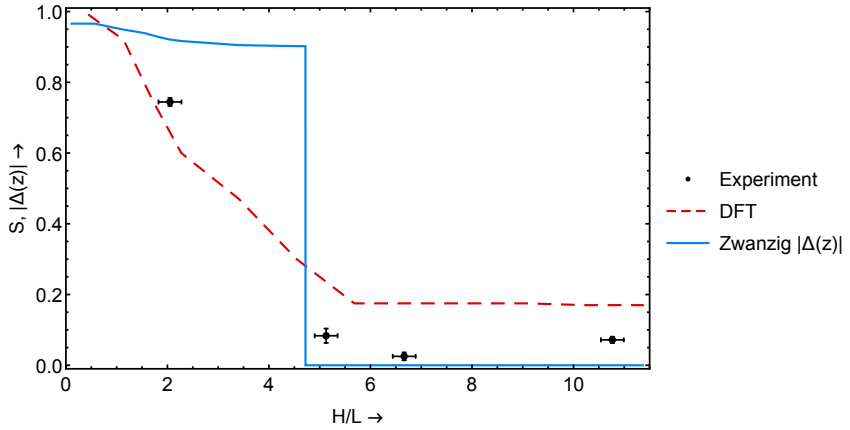


Figure 4.12: Experimental order parameter of the grand canonical sample versus the height of the channel (black) and corresponding results from DFT calculations (red dashed) and the Zwanzig model (blue). Error bars represent the standard deviation.

walls. The relevant DFT equations and the details of the numerical implementation are provided in [127].

Using this DFT model, the order parameter S was calculated in the middle of a channel for different channel heights H using the parameters equivalent to the grand canonical experiment. The stiffness parameter was set such that the persistence length of a rod is roughly 3 times its contour length to mimic the *fd*-virus parameters. The resulting order parameter is shown in figure 4.12 together with the grand canonical data from the experiment and the order parameter Δ (equation 4.6) calculated using the Zwanzig model. Both the Zwanzig model and DFT calculations show a good agreement with the experiment in terms of the channel height at which capillary nematisation takes place. Furthermore, both DFT and experiment produce small but non-zero values of S for the slit heights significantly higher than the one corresponding to the nematisation. On the theory side, this behaviour is due to the residual propagation of the wall-induced order all the way towards the middle of the slit. Overall the novel off-lattice DFT model based on a semi-flexible chain produces the values of the order parameter in the middle of the slit (as a function of the slit height) that are in good agreement with the experimental observations.

Apart from capillary nematisation itself, the DFT calculations reveal that nematic ordering also appears in the vicinity of the walls well before the capillary nematisation transition has taken place, see figure 4.13. Compared to the Zwanzig model (figure 4.11), which predicts a pronounced wetting layer, the DFT calculations show that the concentration of rods drops off

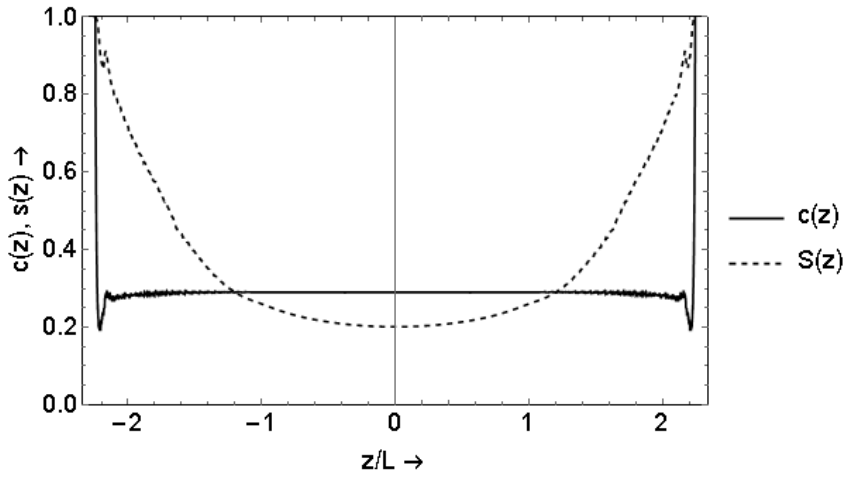


Figure 4.13: Concentration $c(z)$ and order parameter $S(z)$ for a channel of $H/L = 4.5$ calculated using the more elaborate DFT model.

much faster close to the wall. The order parameter however decreases slowly and even remains non-zero in the centre of the channel. Looking at the results for both models, it is not clear why we did not observe wetting layers in the experiments.

Although the order parameter Δ in the Zwanzig model goes to zero in the isotropic phase, DFT calculations show a non-zero order parameter in the middle of the channel in cases where capillary nematisation has not occurred. This behaviour is due to the propagation of the nematic wetting layer all the way towards the middle of the channel. The experimental values for the order parameter S in this region are non-zero, but lower than those predicted from DFT. It is unclear why the order parameter in the experiments is non-zero, as in the theory this is an effect of the nematic wetting layers, which we did not observe in the experiment. This could be an indication that there actually is a wall-induced ordering effect, which simply cannot be observed in our experiment, for example because the wetting layer thickness is smaller than the axial resolution of our microscope.

The incorporation of non-restricted orientation and rod flexibility clearly makes a large difference in the nature of the capillary nematisation transition and the order parameter values found. Recent work by Luzhbin and Chen [124] shows that the flexibility of rods indeed has a significant influence on the phase transition. They found that an increase in flexibility of the rods leads to a higher concentration at which the capillary nematisation transition occurs and a sharper phase transition. The phase transition in the Zwanzig model, where rods are completely rigid, seems to contrast this trend. The sharpness of the phase transition seen in this case may

be a result of the restricted orientation, where a deviation from the nematic director immediately leads to a large excluded volume.

4.5 Conclusion

In conclusion, we have experimentally shown capillary nematisation in a colloidal liquid crystal, which, to the best of our knowledge, has not been observed before. We have compared our results with calculations performed using both the Zwanzig model of rigid rods and an off-lattice DFT model of semi-flexible rods, and find very good agreement for capillary nematisation itself. Nematic wetting for a single wall was predicted by both theories, but was not observed in the experiments, the extent of which is possibly suppressed by rod flexibility as shown by the DFT calculations.

Acknowledgements

This work was a collaboration with Professor Sergei A. Egorov from the University of Virginia. Professor Pavlik Lettinga is thanked for providing the *fd*-virus particles used in this chapter.

Chapter 5

Orientational behaviour of silica rods in a Poiseuille flow

We study the orientational behaviour of colloidal silica rods flowing through a microfluidic channel. The system is confined down to approximately 3 rod lengths in one dimension, resulting in a Hele–Shaw-like flow, with a Poiseuille flow in the confined dimension and a constant flow velocity in the other dimension. We observe kayaking and xy-tumbling behaviour, with a slight dependence on flow velocity. The orientational behaviour is found to be relatively random, as opposed to the periodic motions predicted by Jeffery's theory. We compare our results with multi-particle collision dynamics simulations, which take into account both hydrodynamics and Brownian noise. The simulations show qualitative agreement with the experimental results. This is a strong indication that the presence of Brownian motion can explain the difference between experiments and Jeffery theory.

5.1 Introduction

The orientational behaviour of single non-Brownian spheroidal rods in a simple shear flow was analysed theoretically by Jeffery in 1922 [76], who found that the rods will undergo a periodic tumbling motion. In the years thereafter, much work was done in an attempt to expand the results found by Jeffery to macroscopic rheological properties of rod suspensions in more complicated systems, such as particles with Brownian motion [128–130], polydisperse particles [128, 131–133], interacting particles [134], fluid inertia [135] and more complicated shear fields [136]. All of these investigations have shown that, independent of initial conditions, the same steady state will be reached, where rods have a (time-dependent) preferred orientation. The distribution of orientations around this preferred orientation was found to be constant through time.

Although the macroscopic properties of suspensions have been extensively studied in many different complex systems, the behaviour of individual rods is not yet fully understood in systems that differ from Jeffery's ideal system. Work has been done on slightly asymmetric particles [137–139], where quasi-periodic or in some cases even chaotic tumbling behaviour was found. The effects of other deviations from the ideal system, such as Brownian motion and asymmetric shear profiles, have not yet been investigated. Both of these properties are crucial when describing suspensions of particles flowing through a channel, where the flow profile is often Poiseuille-like. One example of such a system is the flow of red blood cells through a blood vessel.

In this chapter, we study the behaviour of rod-shaped silica particles in a plane Poiseuille flow. The system is confined in one dimension and particles exhibit Brownian motion. We observe single rods as they move through the channel using optical microscopy and analyse their orientational behaviour. The results are compared to multi-particle collision dynamics (MPCD) simulations, which shows good agreement with experiments.

This chapter is outlined as follows. We start by discussing Jeffery's theory for non-Brownian rods in a simple shear in section 5.2. Section 5.3 describes the experiments performed and the results are shown in section 5.4. We then compare our experimental results with Jeffery's theory in section 5.5. The MPCD simulations performed in order to better understand our experimental results are described and discussed in section 5.6 and finally section 5.7 summarises our results and their implications.

5.2 Jeffery orbits

In his seminal 1922 paper, Jeffery [76] showed that axisymmetric ellipsoidal particles in a linear shear flow undergo a periodic rotational motion. The orbit a particle follows is determined by the aspect ratio λ, the shear rate $\dot{\gamma}$ and the orbit constant C, and has a period of $T_J = \frac{2\pi\left(1+\lambda^2\right)}{\dot{\gamma}\lambda}$. These Jeffery orbits are described by

$$\vec{n}(C,t) = \frac{1}{\sqrt{\cos^2\omega t + \frac{1}{C^2} + \lambda^2 \sin^2\omega t}} \begin{pmatrix} -\cos\omega t \\ \frac{1}{C} \\ \lambda \sin\omega t \end{pmatrix}, \tag{5.1}$$

where $\vec{n}$ is the normalised orientation of the rod, t is time and $\omega = \frac{2\pi}{T_J}$ is the frequency of the orientational motion.

The orbit constant depends on the initial orientation of a rod and can range from 0 to ∞. For $C = \infty$ the orbit describes a circular motion in the xz-plane, where x is the direction of flow and the shear gradient is along z (see figure 5.6 for the flow profiles). A rod following this orbit is oriented along the direction of flow for most of the time, and periodically flips by 180°. This type of motion is called "tumbling" in literature. For smaller values of C, the motion will have a stronger y-component, and looks very similar to the paddles of a kayak if viewed from the side, hence the term "kayaking" for these orbits. At $C = 0$, the rod will orient along the y-direction and only rotates around its long axis. This last type of motion is called "log-rolling", and has been shown to be unstable for rod-shaped particles [140]. Figure 5.1 shows Jeffery orbits plotted on a unit sphere for $\lambda = 6$, $\dot{\gamma} = 1/\mathrm{s}$ and different values of C.

The periodicity of the motion is more obvious when plotting the projections of the rod orientation, n_i, on the x, y and z-axes, as shown in figure 5.2 for three different Jeffery orbits. The motion for a particle kayaking with a large amplitude in x (figure 5.2(b)) looks similar to that of a tumbling particle (figure 5.2(c)), except that the amplitude in n_z is smaller and the motion has a large y-component. With decreasing orbit constant (figure 5.2(a)), the average value of n_y increases, with the amplitude n_z decreasing faster than n_x. For all orbit constants, n_x and n_z change sign periodically, while n_y keeps its sign, as is expected from the orbits shown in figure 5.1.

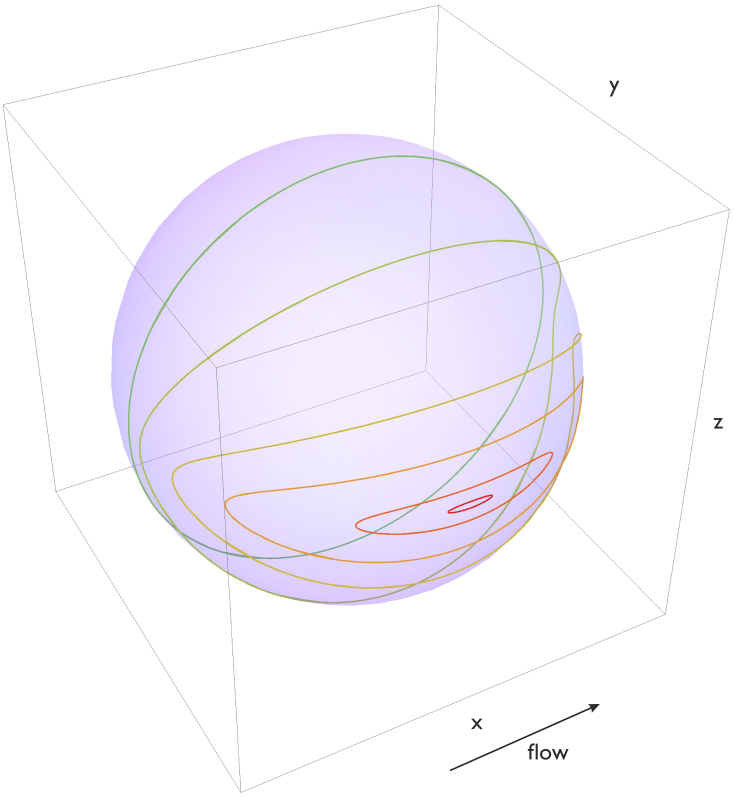
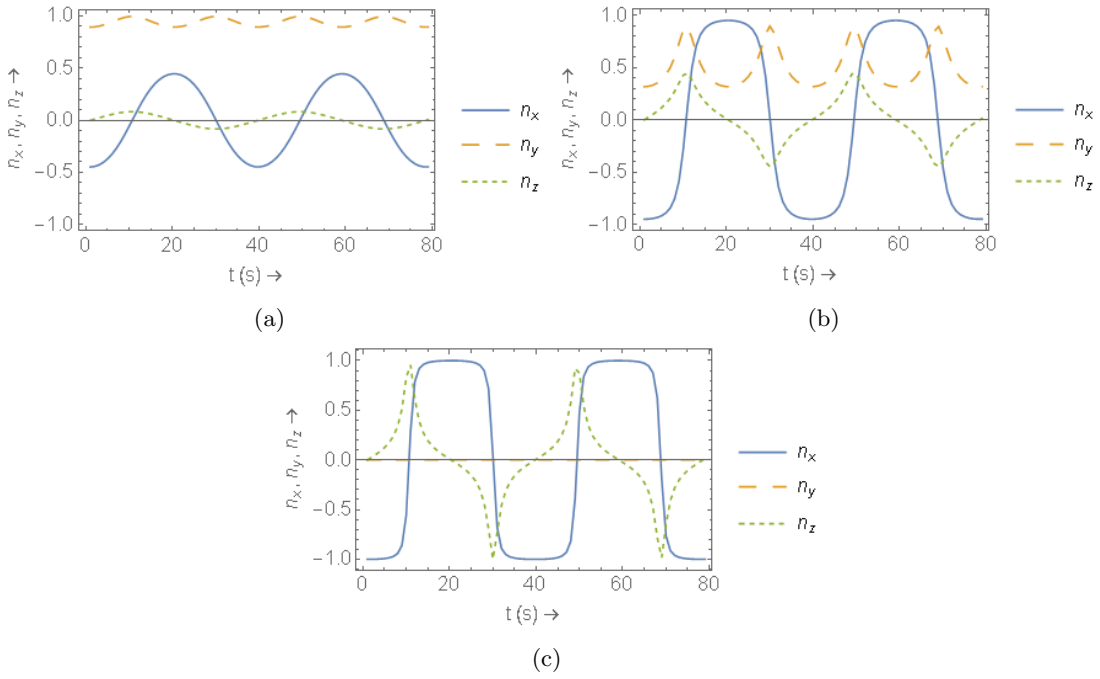


Figure 5.1: Jeffery orbits for $\lambda = 6$, $\dot{\gamma} = 1/\text{s}$ and $C = 0.1, 0.5, 1.5, 3, 10, \infty$, going from red to green, plotted on a unit sphere.



(a) (b)

(c)

Figure 5.2: Projections of the rod orientation on the x, y and z-axis for Jeffery orbits with $\lambda = 6$, $\dot{\gamma} = 1/\text{s}$ and (a) $C = 0.5$, kayaking with a small amplitude in x, (b) $C = 3$, kayaking with a large amplitude in x, and (c) $C = \infty$, tumbling.

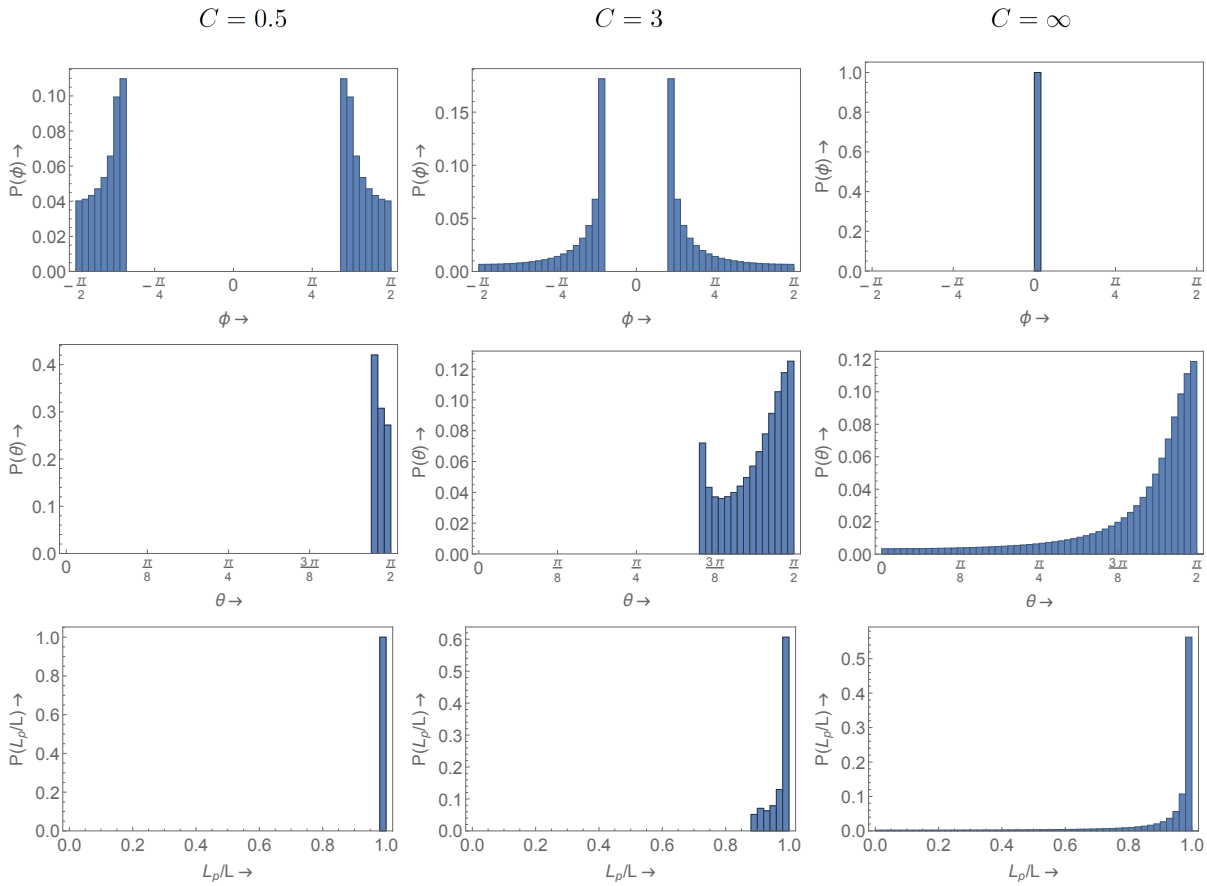


Figure 5.3: Orientation distributions for rods following Jeffery orbits with $C = 0.5$ (left), $C = 3$ (middle) and $C = \infty$ (right). Top row: ϕ, middle row: θ and bottom row: L_p/L.

A more quantitative measure for the orientational motion can be obtained by plotting the orientation distributions of a rod that is tracked through time. Figure 5.3 shows the orientation distributions in terms of ϕ, the angle between the projection of a rod on the xy-plane with respect to the x-axis and θ, the angle of a rod with the z-axis (see figure 5.4 for the definition of these angles). The normalised projection length of the rods, L_p/L, is also plotted, because this is what we focus on in the experiments instead of θ, as will be explained later.

For a tumbling rod (on the right in figure 5.3) ϕ is always zero, as the tumbling motion takes place in the xz plane. The distribution of θ contains all possible orientations, but is strongly peaked around $\theta = \frac{\pi}{2}$. This is a result of the fact that the rate of change in orientation is not constant; a rod spends most of its time oriented along the x-axis, and the least time oriented along z, where the shear force exerted on the particle is strongest. For kayaking particles the distribution in ϕ contains a gap around zero, of which the width increases with decreasing orbit constant. The distribution is peaked on the edges of this gap, again because the particle spends

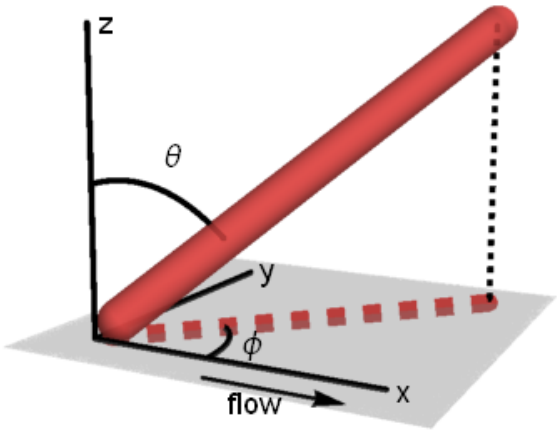


Figure 5.4: Schematic figure showing the angles ϕ and θ. The red dashed line indicates the projection of the rod on the xy-plane.

most of its time on the apex of the orbit, which is the point closest to aligning with the flow. The distribution in θ narrows with decreasing C, lower values for θ are no longer explored as the orbit flattens out towards the xy-plane. Note that the limits of the angles in figure 5.3 are half of what they usually are, as for symmetry reasons an orientation of ϕ is equivalent to that of $\phi + \pi$, and similar for θ.

Jeffery's theory works really well for a system of axisymmetric particles in a simple shear, where noise does not play a role. Any deviations from this ideal system however, will result in different behaviour. Yarin et al. [139] have shown that triaxial particles can deviate from Jeffery orbits even at a very small degree of triaxiality. Depending on the initial orientation of the rod, either a double periodic motion, where particles periodically change between different Jeffery orbits, or a chaotic motion was found. The effects of more complicated shear profiles and thermal noise on the orientational motion of rods are not yet fully understood and form the focus of the present work.

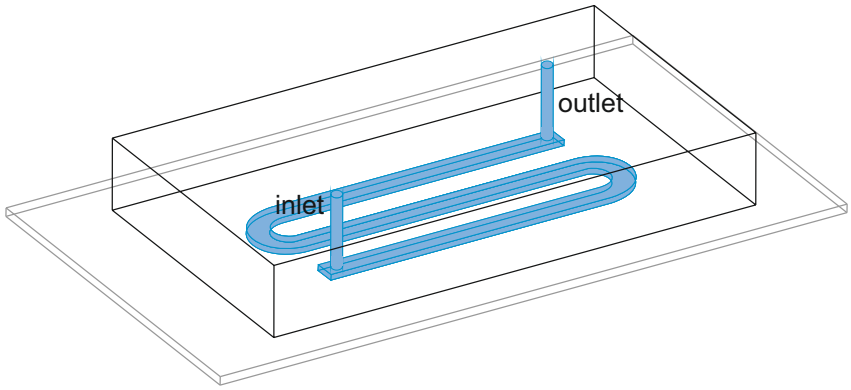


Figure 5.5: Schematic representation of the microfluidic channels used.

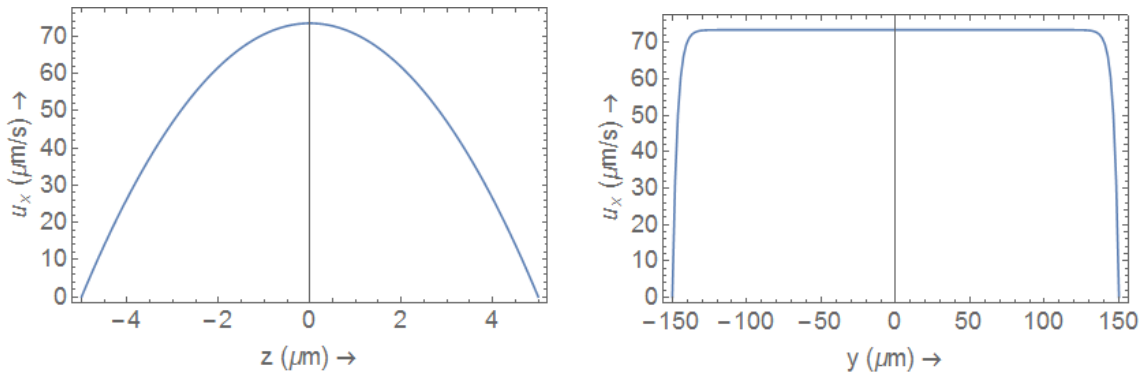
5.3 Experimental methods

Silica rods with a length of 3 µm and a diameter of 0.5 µm were dispersed in deionised water. The concentration of rods was approximately 10 particles/nl at most, such that particles are far apart and do not interact with each other. The rods are bullet-shaped, with one end being a spherical cap while the other end is straight (see section 2.1.2 for a more detailed discussion of the rods).

Microfluidics devices with a simple, unbranched channel, having a height of 10 µm and a width of 300 µm were prepared in PDMS. The channel design is schematically shown in figure 5.5. The bends in the channel are purely to increase the length, so that rods have enough time to settle before being imaged. Particles were imaged in the centre of the second straight segment, such that the effect of the bends as well as the walls can be neglected. Channels were plasma cleaned before use and a flow was achieved via a pressure difference between inlet and outlet tubes, by using gravity.

As the width and length of these channels is much larger than their height, the flow profile is comparable to a Hele-Shaw flow [60], having a plane Poiseuille flow in the xz-plane (figure 5.6(a)), whereas the flow velocity is constant in the xy-plane except close to the walls (figure 5.6(b)). The particles flowing through these channels therefore experienced a non-linear, asymmetric shear in the xz-plane. As the silica rods will sediment easily, rods will typically be at the lower end of the flow profile shown in figure 5.6(a), where the shear rate changes quickly with z.

The system was imaged in the xy-plane, using a Zeiss LSM 5 Exciter in bright field mode,



(a) (b)

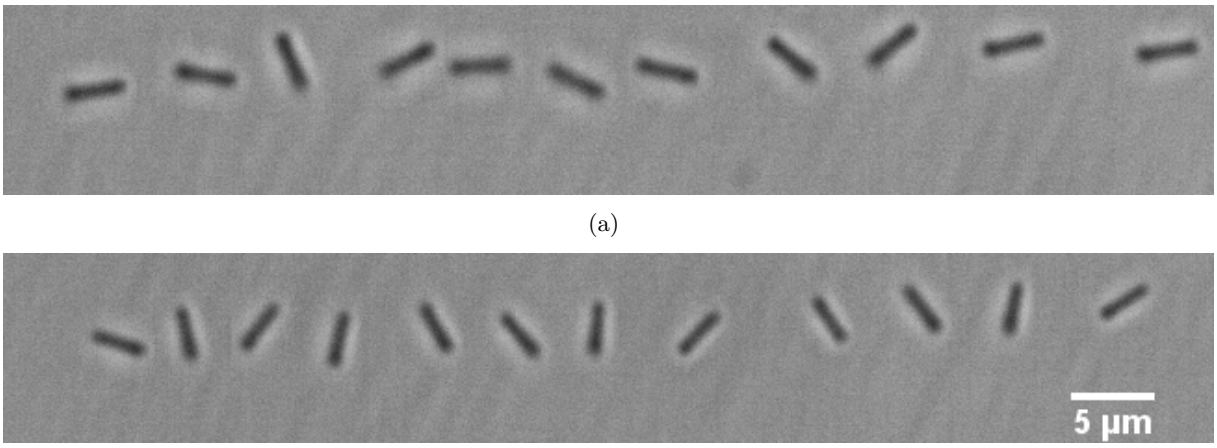
Figure 5.6: Theoretical flow profiles in the microfluidic channels used, (a) in the xz-plane and (b) in the xy-plane.

with a 63x 1.4 NA oil-immersion objective. Images were recorded using a Ximea MQ042MG-CM CMOS camera. Care was taken to image in the centre of the channel, away from the walls and bends. Image series of 1000 frames with a frame rate of 10 frames/s were recorded. Particles were then tracked through time and their positions, orientations in the xy-plane, ϕ, and projected lengths L_p determined in each frame using image analysis techniques described in section 2.5. The projected length of the rods on the imaging plane was used to determine the absolute value of the z-component of the orientation, which is therefore always positive.

5.4 Results

A wide variety of behaviour was seen for particles flowing through a microfluidic channel. Kayaking was seen for most particles, but tumbling in the xy-plane was observed as well. This latter behaviour is interesting, as it is not predicted by Jeffery's theory. Examples of rods exhibiting these two types of motion are shown in figure 5.7. Both images show a single rod at different times as it moves through the channel, with 0.3 s between each used image. Note that although the motion for the two rods looks similar at first glance, the xy-tumbling rod (figure 5.7(a)) rotates a full 360°, while the orientation of a kayaking rod (figure 5.7(b)) goes back and forth. Particles tumbling in the xz-plane, as predicted by Jeffery's theory, were not observed.

The orientation of each particle was tracked through time and plotted on a unit sphere, which makes it easier to identify the type of motion exhibited by each particle. In addition, the x, y and z-components of the orientation were plotted in order to see if the motion is periodic.



(a)

(b)

Figure 5.7: Image showing a silica rod at different times as it flows through a microfluidic channel. (a) an xy-tumbling rod and (b) a kayaking rod.

Examples of these two plots are shown in figure 5.8 for both an xy-tumbling rod and a kayaking rod. Note that these examples were chosen specifically because they show these two behaviours most clearly, but are not representative for all rods. The difference between xy-tumbling and kayaking can easily be seen in the orientation tracks plotted on a unit sphere. The track of a kayaking particle stays on a quadrant of the unit sphere (figure 5.8(b)), whereas a tumbling particle will cover both sides of the y axis (figure 5.8(a)). In the bottom two plots in figure 5.8, the difference is best seen in n_y, which changes sign for a tumbling particle, but mostly remains the same sign for a kayaking particle.

In contrast to Jeffery's theory, where rods will follow a single periodic orbit indefinitely, the behaviour of rods in our experiment was found to be very irregular, with rods changing from kayaking to xy-tumbling or even flow-aligning at seemingly random moments. This makes it very difficult to quantify the behaviour. As a rough estimate, particles were labelled as either xy-tumbling or kayaking, based on which of the two was dominant for that particular rod. Only particles that could be tracked through a minimum of 25 frames were taken into account, which corresponds to roughly one period of tumbling. Out of 108 rods that were analysed, 63 particles (58%) were found to be mainly kayaking, with a wide range of different amplitudes, 37 (34%) were found to be mostly xy-tumbling, and 8 (7%) were found to have different behaviour, meaning that their orientation was too random to fit into either category.

For the kayaking particles, the amplitude of kayaking was determined by looking at the distance between maxima of n_x in each orbit. A histogram showing the distribution of amplitudes

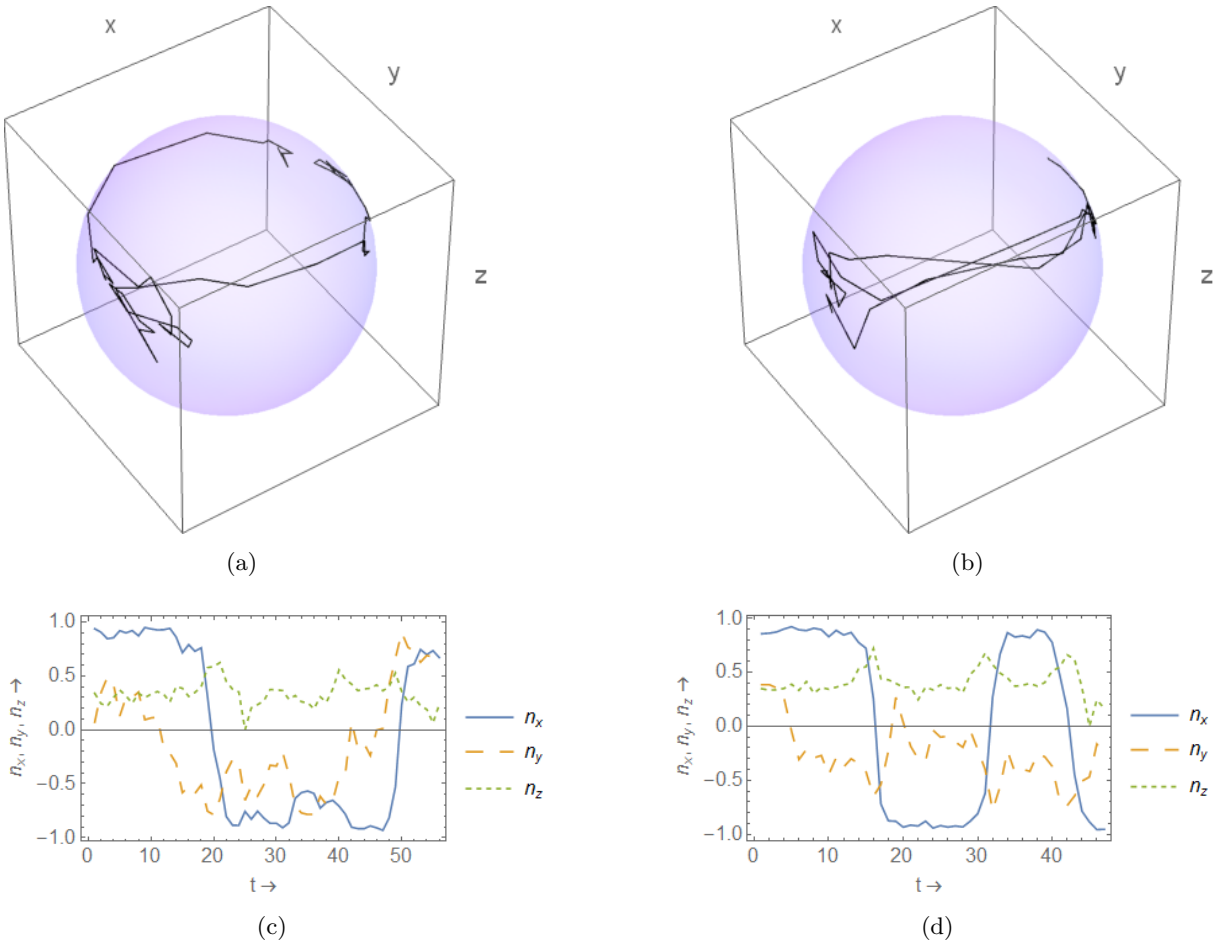


Figure 5.8: The orientation of a rod plotted on a unit sphere for (a) an xy-tumbling rod and (b) a kayaking rod, and (c) and (d) the corresponding plot of the x, y and z components of the orientation.

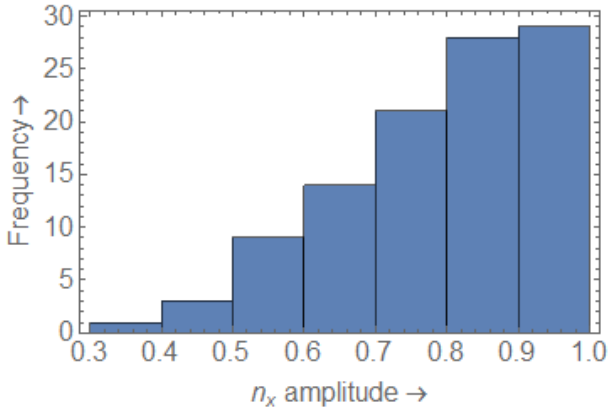


Figure 5.9: Histogram showing the distribution of amplitudes in n_x for kayaking particles.

is shown in figure 5.9. The average amplitude was found to be $\Delta n_x = 0.79 \pm 0.14$, indicating that most particles are kayaking with a relatively high amplitude (corresponding to a higher orbit constant in Jeffery's theory), almost aligning with the flow direction at the maxima.

5.4.1 Orientation distributions

Orientation distributions of the rods were calculated in an attempt to get a more quantitative measure for the orientational behaviour. All the rods in each tracked frame were taken into account in these distributions, leading to a total of 3666 orientations measured from 108 particles. Figure 5.10 shows the distributions for the angle ϕ, the orientation in the xy-plane measured from the x-axis and the angle θ, the angle between a rod and the z-axis (see figure 5.4 for a schematic representation of the two angles). In addition, the projected length of the rod, which is used to calculate θ, is plotted in figure 5.10(c).

The average value of ϕ is close to zero, meaning the particles are most likely to align with the flow-direction. The distribution of ϕ looks most similar to that of a particle kayaking with a high amplitude in n_x in Jeffery's theory (see figure 5.3). In such Jeffery orbits, however, kayaking particles never fully align with the x-axis, and therefore there is a gap in the distribution at $\phi = 0$. In our experiment we observe several xy-tumbling rods, which cross over the x-axis during their motion, which could account for the relatively large values of ϕ around 0.

The average value of θ is found to be close to $\frac{3\pi}{8}$, whereas for kayaking or xy-tumbling particles one would expect a peak in the distribution close to $\frac{\pi}{2}$, i.e. the rod lying in the xy-plane (see figure 5.3). This discrepancy is most likely an effect of the image analysis process. The

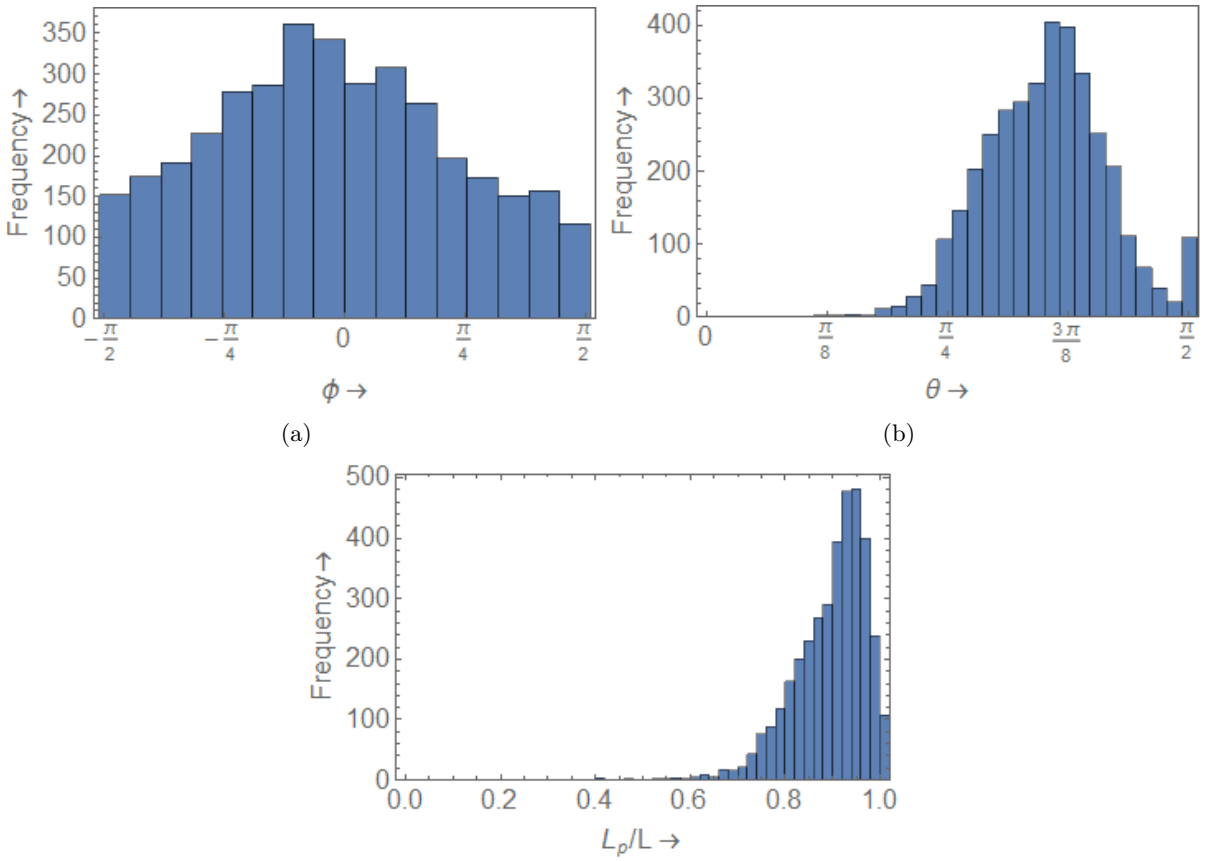


Figure 5.10: Histograms of orientation distributions for all particles. (a) ϕ, the orientation in the xy-plane, (b) θ, the angle of the particle with the z-axis and (c) L_p/L.

angle θ is calculated using $\theta = \arcsin\left(\frac{\lambda L_p/L - 1}{\lambda - 1}\right)$, where $\lambda = 6$ is the aspect ratio of the rods, L_p is the projected length of a rod measured from the image analysis and L is the length of the rod, which is taken to be the maximum value of L_p found for each rod. This measure for L is used because it is not possible to measure the length of each individual rod exactly. As can be seen from figure 5.10(c), L_p/L is peaked around 0.9 instead of 1, which is most probably caused by the fact that there is a relatively large error in the measurement of L_p, and therefore L is overestimated for each rod. This error in L_p/L is even more pronounced in θ, as the arcsin is most sensitive to changes in the argument when the argument is close to 1. We therefore decide to focus on the distribution of L_p/L rather than θ, while keeping in mind that the distribution is slightly shifted to the left.

5.4.2 Velocity

The flow velocity can have an influence on the orientational behaviour of a rod in two ways. Firstly, a higher flow velocity results in a stronger and less symmetric shear force experienced by the particle at the same z-position. Secondly, at a high flow velocity, a rod-shaped particle will tend to align with the flow-direction to minimise drag [75].

The instantaneous and average velocity of each particle was determined by calculating the distance travelled in a frame or complete track respectively, and dividing by the time. The instantaneous velocity was found to be relatively constant for all particles, changing by no more than a few µm/s throughout the time the particle was tracked. The average velocity of particles was found to be roughly between 10–40 µm/s. Figure 5.11 shows a histogram of all average velocities. The Péclet number for this system, defined as $Pe = \frac{\eta\dot{\gamma}L^3}{k_B T}$, with η the viscosity, $\dot{\gamma}$ the shear rate, L the length of a rod and $k_B T$ the thermal energy, is on the order of $Pe \sim 50$. This means that the shear force is dominant over Brownian motion (see section 1.4). The Reynolds number is on the order of $Re \sim 10^{-5}$, meaning that inertial effects are negligible.

To determine if the flow velocity influences the behaviour of rods in terms of whether kayaking or xy-tumbling is preferred, tracked particles were divided into two groups based on their average velocity. The slowest half was found to contain 32 kayaking and 18 tumbling particles, versus 31 kayaking and 17 tumbling particles in the faster half. A similar result was found when dividing the tracks into three or four groups. This indicates that the velocity does

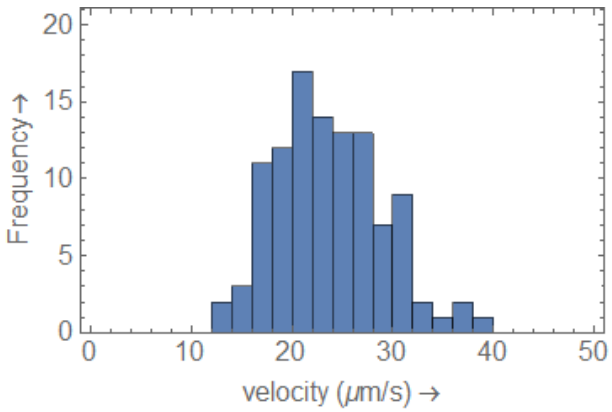


Figure 5.11: Histogram showing the distribution of velocities of all tracked particles.

not influence which type of behaviour is preferred for rods, within the velocity range that we observed. This is consistent with Jeffery's theory, where the orbit followed depends only on the initial orientation of the rod, and the velocity merely changes the frequency of the motion. It also suggests that the shape of the shear profile either does not change significantly with increasing velocity, or does not influence the orientational behaviour much within the velocity range observed.

The effect of the flow velocity on the average orientation of rods was investigated by plotting the distribution of rod orientations. The rods were divided into four equally large groups based on their average velocities, and the orientation distributions were determined. For each rod, the orientation in each tracked frame was taken into account. Figure 5.12 shows the distributions of the angles ϕ and θ, as well as L_p/L for the four groups of particles, with velocity increasing from left to right.

It can be seen that as the velocity increases, the distribution of ϕ narrows around a constant mean value of 0, meaning that particles are more often oriented along the direction of flow. The distributions of θ and L_p/L are similar at all velocities, with an average mean angle of $\bar{\theta} = 1.15$, or close to $\frac{3\pi}{8}$. To quantify the width of the distributions, a Gaussian function was fitted to each of the distributions in figure 5.12 and the full width at half maximum (FWHM) was determined. The resulting FWHMs for both ϕ and θ are shown in figure 5.13. We use θ instead of L_p/L in this case because we are comparing the width of the distributions in the two angles. Note that we choose a Gaussian fit simply to get a measure for the width of the distributions, and do not claim the distributions should indeed have a Gaussian shape.

The FWHM of ϕ is clearly much larger than that of θ, even when taking into account

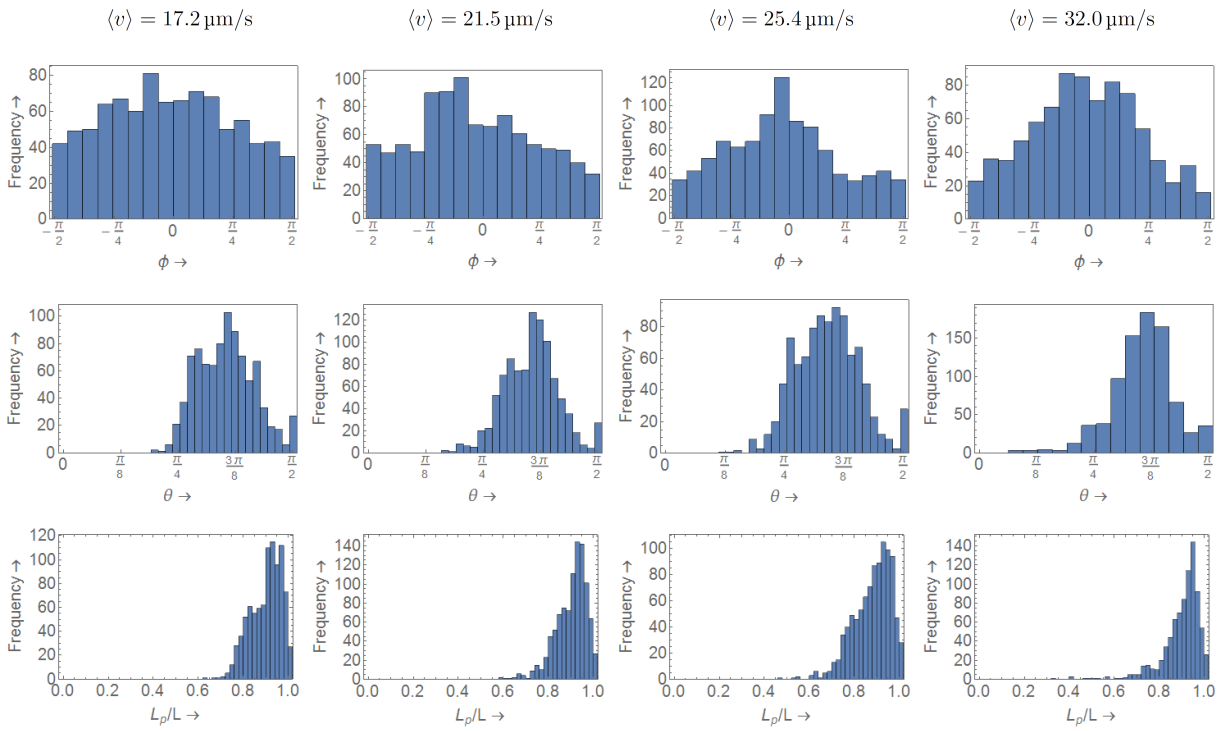


Figure 5.12: Distributions of the angles ϕ (top) and θ (middle) and L_p/L (bottom) for particles divided into four equally large groups based on the average velocity of a particle, with velocity increasing from left to right.

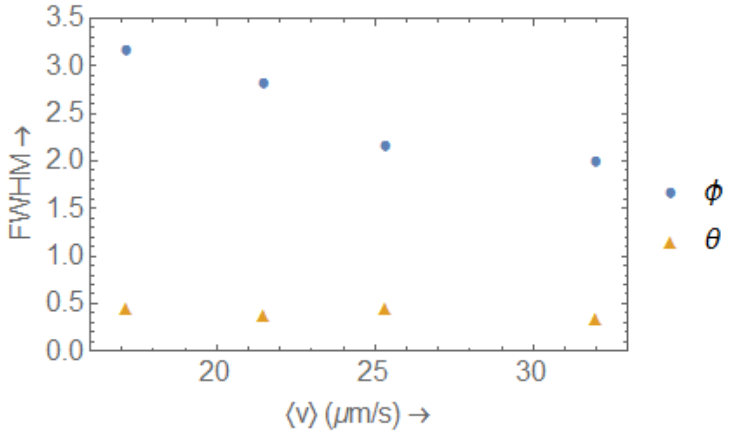


Figure 5.13: Full width at half maximum of the Gaussian fits to the orientation distributions of ϕ and θ in the four velocity groups.

that the range of possible angles for ϕ is twice as large as that for θ. This, together with the relatively large values of θ, indicates that the kayaking and tumbling motions span all of the possible orientations in the xy-plane, while the motion in z is limited. This can be explained by the fact that the rods are relatively heavy and therefore a flat orientation, with $n_z = 0$ and $\theta = \frac{\pi}{2}$, should be favoured due to gravity. As discussed earlier, the lower average value for θ and L_p/L found in the orientation distributions is possibly caused by the way in which n_z, and therefore θ, is determined, namely by determining the projected length of a rod, which is inherently relatively inaccurate.

5.5 Comparison to Jeffery theory

The observed orientational behaviour of silica rods deviates in many ways from Jeffery's theory. The most obvious difference lies in the aperiodicity of the motions observed and the apparent random jumping between different orbits. This type of motion has been predicted theoretically for triaxial particles [139] and has been observed in non-Brownian rods [137], where the authors again attribute this effect to the slight asymmetry of their particles. It is possible that the asymmetry in the ends of our silica rods leads to the seemingly random behaviour observed. Another possible explanation is that Brownian motion of the rods changes their orientation in such a way that they move from one orbit to another constantly, leading to a seemingly random orientational motion.

The xy-tumbling motion, which is not predicted by Jeffery theory and also has not been observed for anisotropic particles, can be explained by Brownian motion as well. If the particles follow a kayaking motion with a large amplitude, they come very close to aligning with the x-axis after each flipping motion. As in a Jeffery orbit a particle spends most of its time in this flow-aligned orientation, the particle will spend some time performing a Brownian motion around this orientation, which could pull the particle to the other side of the x-axis before it starts another kayaking cycle, effectively making it tumble in the xy-plane.

Finally, the non-linear and asymmetric shear profile used in our experiments could influence the behaviour of rods and lead to a deviation from Jeffery theory, where a simple shear flow is considered. The two ends of a tumbling rod will experience different shear forces. Additionally, small changes in the z-position of a particle will have a large effect on the shear force profile

experienced by it. The exact effects of this on the tumbling behaviour of rods is difficult to predict. We have therefore performed multi-particle collision dynamics simulations to get a better understanding of our experimental results.

5.6 Simulations

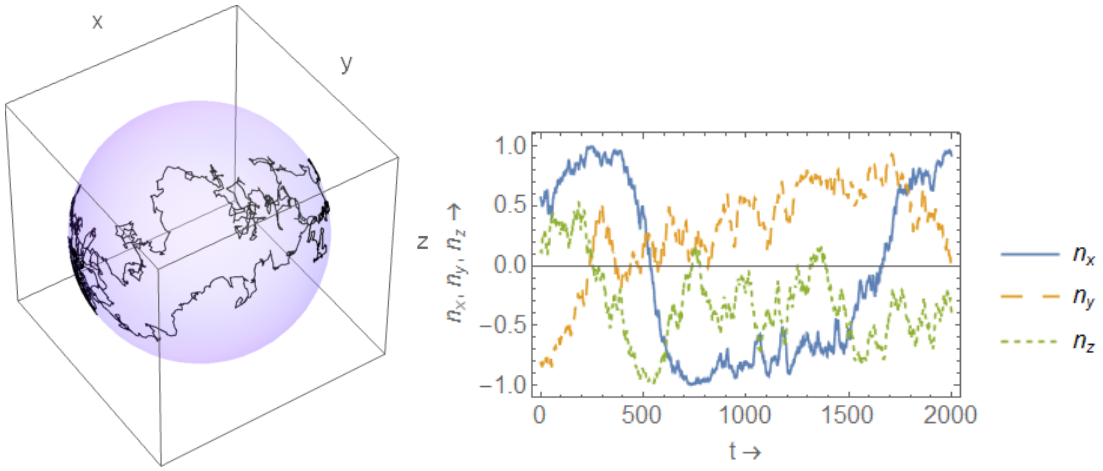
Note: The simulations were performed by Dr. Andreas Zöttl at the Rudolf Peierls Centre for Theoretical Physics, University of Oxford, in the group of Professor Julia Yeomans

In order to get a better insight in the underlying reasons for the aperiodic orientational behaviour observed in our experiments, multi-particle collision dynamics (MPCD) simulations were performed. MPCD simulations are ideal for systems where both hydrodynamics and thermal fluctuations are important [141].

The parameters used in the simulations were set to mimic the experimental system as closely as possible. In each simulation, a single rod was modelled as a rigid spheroid with a length of 3 µm and a diameter of 0.5 µm. The density difference between the rods and the surrounding fluid was set to $1\,\mathrm{g/cm^3}$. The surrounding fluid (water) is modelled explicitly using approximately 3×10^6 pointlike particles. Confinement is incorporated via two hard walls in the xy-plane, with a distance of 10 µm between them. Periodic boundary conditions were used on the x- and y- edges of the simulation box, which was 12 µm by 12 µm in size.

The simulation consists of streaming and collision steps. In the streaming step, fluid particles undergo ballistic movement during a time step Δt, driven by a constant pressure force $\vec{F}$ that models the pressure-driven flow in the experiments. In the collision steps fluid particles interact with each other, the walls and the rod with the help of virtual particles [141,142]. When fluid particles collide with a wall or the rod, a bounce-back collision rule, in which particles are reflected back to the position they came from, is applied to satisfy the no-slip boundary conditions. When a collision occurs between a fluid particle and the rod, momentum and angular momentum are transferred between the two. The fluid is kept at a constant temperature T, fixing the strength of thermal noise. The relative strength of shear and Brownian motion, i.e. the Péclet number, can be tuned via the driving force $\vec{F}$.

For each simulation, a single rod was simulated. The rod was initially placed at $z = -3.5$ µm



(a) (b)

Figure 5.14: (a) Orientation track of a typical simulated rod plotted onto a unit sphere and (b) the corresponding plot of n_x, n_y and n_z.

and the initial orientation of the rod was randomised. During the simulation, the rod was observed to slowly drift towards $z = 0$. This behaviour is interesting, as the rods have a gravitational length of $L_g \approx 0.8\,\mu\text{m}$ (see section 2.1.2), meaning that based on just gravity one would expect a z-position close to $z = -4\,\mu\text{m}$. Clearly the shear flow has an effect on the position of a rod in the channel here. It is not clear if this effect is also present in the experiments, as it is impossible to determine the z-position of a particle with the current set-up.

In total 40 simulations were performed, with an average Péclet number of $Pe = 5.7$, which is much lower than the estimated $Pe = 50$ for the the experimental system. However, if the z-position of rods in the experiments is actually closer to the centre, at $z = 0$, than expected, the Péclet number may be much lower than originally estimated. The orientational behaviour of simulated rods was found to be very random, roughly resembling the kayaking behaviour seen in Jeffery orbits, but without any periodicity. Figure 5.14 shows the orientation track for a typical rod in the simulations plotted on a unit sphere and the corresponding plot of n_x, n_y and n_z. The behaviour is very similar to that observed in the experimental system. Furthermore, it can be seen from the irregular pattern of the track that Brownian motion obviously plays an important role in the orientational behaviour.

Figure 5.15 shows the orientation distributions, obtained using all simulated rods. It can be seen that qualitatively these distributions agree very well with those found in the experiments (figure 5.10), taking into account the fact that the distributions for θ and L_p/L are slightly shifted towards lower values in the experiment. The distribution of ϕ is peaked more strongly

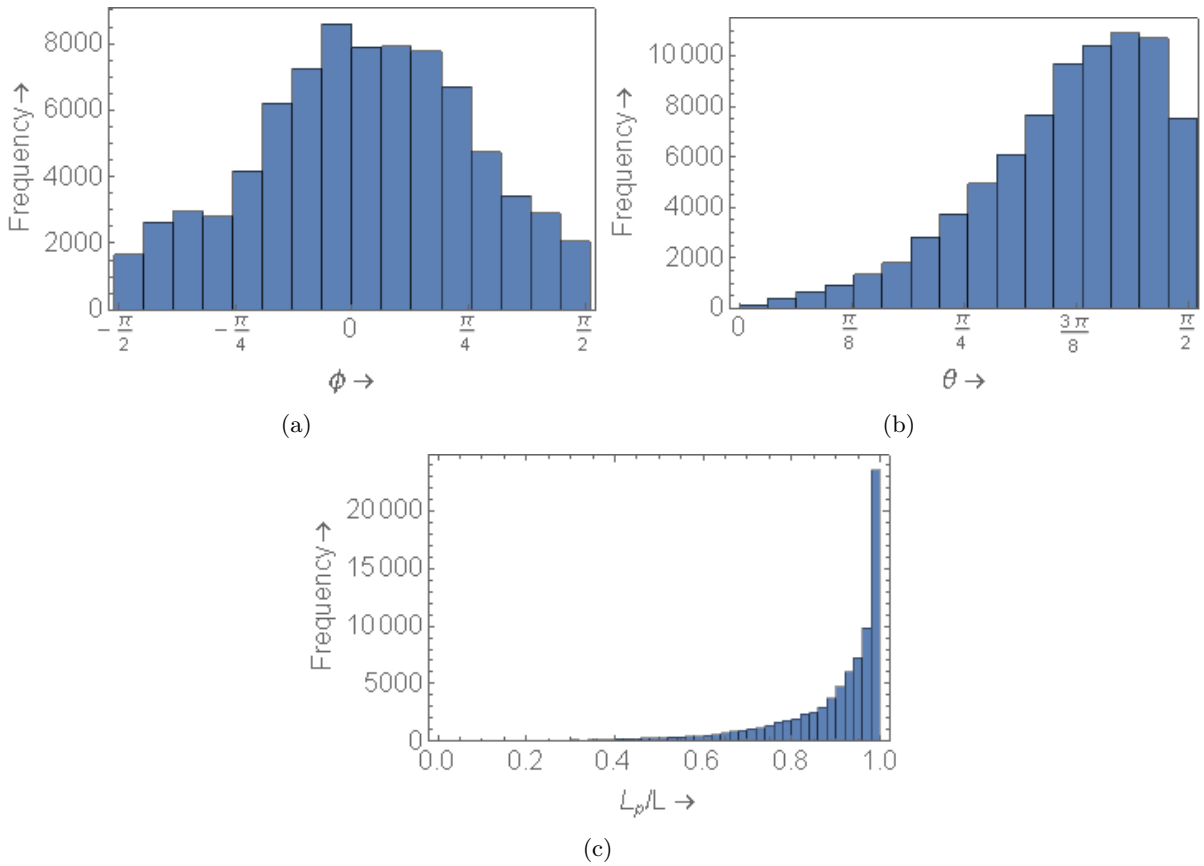


Figure 5.15: Histograms of orientation distributions obtained from the simulations. (a) ϕ, the orientation in the xy-plane, (b) θ, the angle of the particle with the z-axis and (c) L_p/L.

at $\bar{\phi} = 0$ than in the experiments, meaning that rods are more often oriented along the direction of flow. It is possible that this is caused by a slight discrepancy between flow velocities in the experiment and the simulations. In fact, the distribution is quantitatively very similar to that of the fastest group of rods in the experiment (see figure 5.12).

In the experiment we can determine the flow velocity of the rods, but it is not possible to determine the exact z-position of a rod in the channel. This makes it very difficult to correctly estimate the actual experimental flow profile and the resulting shear experienced by a rod.

5.7 Conclusion

We have studied colloidal rods flowing in a plane Poiseuille flow, and observed particles performing kayaking and xy-tumbling motions. The latter behaviour is not explained by Jeffery theory, but is most likely an effect of the Brownian nature of the rods. The orientational motion

of rods was found to be aperiodic, and particles were found to be switching from one type of behaviour to another. This can also be explained by Brownian motion, which allows rods to swap from one Jeffery orbit to another. A weak dependence on flow velocity was found, where a higher velocity leads to particles more often being aligned along the direction of flow. The type of orientational motion was found to be independent of velocity.

Multi-particle collision dynamics simulations were performed in order to better understand the underlying reasons for the deviations from Jeffery theory found in the experiments. These simulations assume axisymmetric particles that undergo Brownian motion, and give very similar results to the experiment. This indicates that Brownian motion can indeed explain the experimental results observed, and the asymmetry of the rods does not necessarily play a role.

Acknowledgements

This work was a collaboration with Dr. Andreas Zöttl and Professor Julia M. Yeomans. We would like to thank Dr. Yongxiang Gao for synthesising the silica rods used in these experiments and Andrew Balin for useful discussions.

Chapter 6

Effects of a magnetic field and of a non-Newtonian fluid on the behaviour of silica rods in a Poiseuille flow

In the previous chapter we investigated the orientational behaviour of silica rods in a plane Poiseuille flow. Here, we expand this further by studying the effect of (i) a magnetic field and (ii) a non-Newtonian fluid on the orientational behaviour of colloidal rods flowing through a microfluidic channel. (i) The magnetic field confines the orientation of a rod to a plane perpendicular to the field. By applying a magnetic field in different directions, we study the effect of the competition between magnetic forces and shear forces on the tumbling behaviour of rods. We observe that we can suppress certain Jeffery orbits towards the plane perpendicular to the field. (ii) Particles flowing through a non-Newtonian fluid were found to be aligned with the direction of flow. The absence of tumbling behaviour may be explained by the depletion interaction between rods and the wall, induced by the presence of xanthan. However, it is unclear why the rods prefer to orient along the flow direction.

6.1 Introduction

Single rod-shaped particles suspended in a linear shear flow undergo a periodic rotational motion due to the difference in flow velocities at the two ends of the rod. These periodic motions were first described by Jeffery [76] for non-Brownian axisymmetric spheroids. The exact orbit followed by a rod depends only on the initial orientation of a rod and can either be a tumbling motion or a kayaking motion (see figure 5.1). The period of the motion depends on the aspect ratio λ and the shear rate $\dot{\gamma}$, and is given by $T_J = \frac{2\pi\left(1+\lambda^2\right)}{\dot{\gamma}\lambda}$.

Although the orientational behaviour of rods in the ideal case is well understood, small deviations from this ideal, e.g. a non-linear shear field or Brownian motion, can lead to very different behaviour, which is not yet fully understood. In chapter 5 we studied the orientational motion of Brownian rods in a plane Poiseuille flow, and found that rods undergo xy-tumbling or kayaking motions, but not in the periodic way expected for Jeffery orbits. In this chapter we further explore deviations from Jeffery's theory, namely the effects of (i) an external force and (ii) a non-Newtonian fluid. To investigate the effect of an external force, we apply a magnetic field to the same system used in chapter 5 and study the interplay between the magnetic torques and the shear flow. The effect of a non-Newtonian fluid is studied by adding a non-adsorbing polymer to the system used in chapter 5, which results in a shear-thinning medium. This type of system is relevant both for polymer processing and many biological processes, e.g. a rod-like macromolecule travelling through a pore.

This chapter is outlined as follows. In section 6.2 we describe the experiments performed, both for the magnetic field and the non-Newtonian fluid. The results are shown and discussed in section 6.3. The experiments with a magnetic field are described first, followed by the experiments in a non-Newtonian fluid. Section 6.4 summarises the results and their implications.

6.2 Experiments

6.2.1 Magnetic field

In these experiments we study the competition between magnetic torques and the torques exerted by the shear flow, which leads to new interesting behaviour of the rod-shaped particles. The

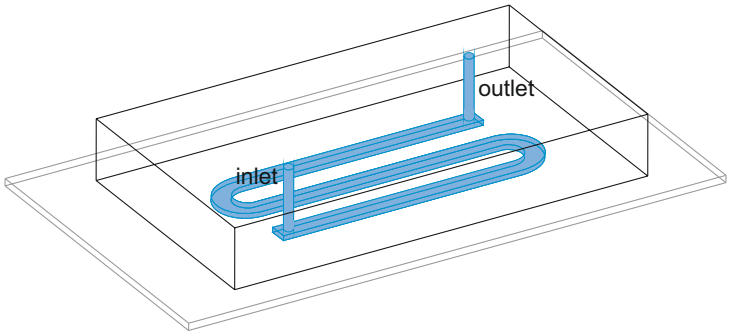


Figure 6.1: Schematic representation of the microfluidic channels used.

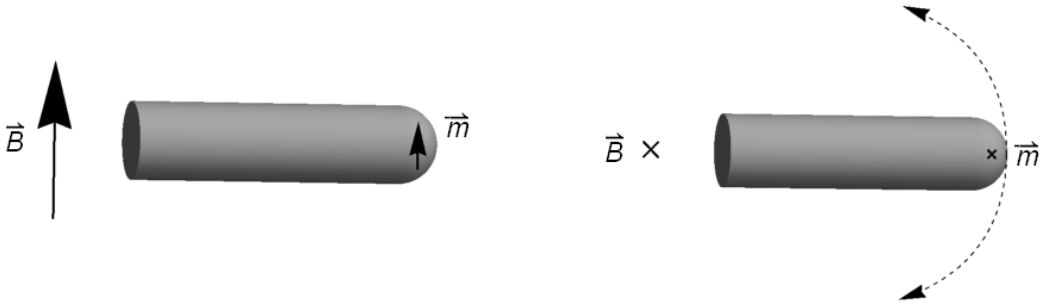
magnetic field confines a rod to a plane perpendicular to the field (see section 2.1.2), suppressing the orientational motion of the rods to a certain degree.

Magnetic silica rods with a length of 3 µm and a diameter of 0.5 µm dispersed in deionised water were used. The magnetic nature of the rods comes from magnetite nanoparticles incorporated in one end of the silica rod during the synthesis process, leading to a permanent dipole moment of $m = 1.4\,\mathrm{k_B T/G}$. Note that the rods were synthesised by Dr. Yongxiang Gao. A more detailed discussion of the particles can be found in section 2.1.2.

Microfluidics channels with a long, unbranched channel were created in PDMS. The channels have a width of 300 µm and a height of 10 µm. A schematic representation of the channel is shown in figure 6.1. The bends in the channel are added only to increase the length of the channel, giving rods ample time to settle and sediment before being imaged. The particles are imaged in the middle of the second straight segment, away from the inlet and outlet.

Channels are plasma cleaned before use and a flow is achieved by using gravity to create a pressure difference between inlet and outlet tubes. The design of the microfluidic channel leads to a plane Poiseuille flow in the xz-plane, where x is the flow direction and z is the direction in which the system is confined down to 10 µm, or approximately 3 rod lengths. The flow velocity in the xy-plane is constant except close to the walls. For this reason we neglect any particles that are found close to the walls in the experiment. For a plot of the flow profiles see figure 5.6 in the previous chapter.

The system was imaged in the xy-plane using a Zeiss LSM 5 Exciter in bright field mode, with a 63x 1.4 NA oil-immersion objective. Image series of 500 frames with a frame rate of 5 frames/s were recorded using a Ximea MQ042MG-CM CMOS camera. Particles were then tracked through time and their positions, orientations in the xy-plane (ϕ) and projected lengths



(a) (b)

Figure 6.2: (a) Orientation of the magnetic dipole, $\vec{m}$, in iron oxide-doped silica rods with respect to the rod and magnetic field, $\vec{B}$. (b) The rod can freely rotate in the plane perpendicular to the magnetic field. Rotation in the other directions is limited.

L_p determined in each frame using image analysis techniques described in section 2.5. The projected length of the rods on the imaging plane was used to determine the absolute value of the z-component of the orientation. For each field direction, the orientational behaviour of 36 or 37 rods were tracked through time.

A magnetic field in either the x, y or z direction was applied to the system using the set-up described in section 2.4. A field of $B_{x,y} = 150\,\mathrm{G}$ was used for the x and y directions, using the four coil set-up. The field strength in the z direction was only $B_z = 30\,\mathrm{G}$, as in this case a larger coil needed to be placed around the sample, which unfortunately was more limited in the field strengths that could be reached.

The resulting magnetic dipole in each particle is oriented roughly perpendicular to the long axis of a rod [143], which means that in a strong magnetic field a rod orients itself in the plane perpendicular to the magnetic field, where it is free to rotate within that plane, as shown schematically in figure 6.2. Rotation in the other directions is limited, with the probability of a certain orientation scaling as $e^{\frac{-\vec{m}\cdot\vec{B}}{k_B T}}$.

6.2.2 Non-Newtonian fluid

Note: The preparation of xanthan stock solution and the rheological measurements were performed by Michael Mordan

In these experiments we study the effect of a non-Newtonian fluid on the orientational

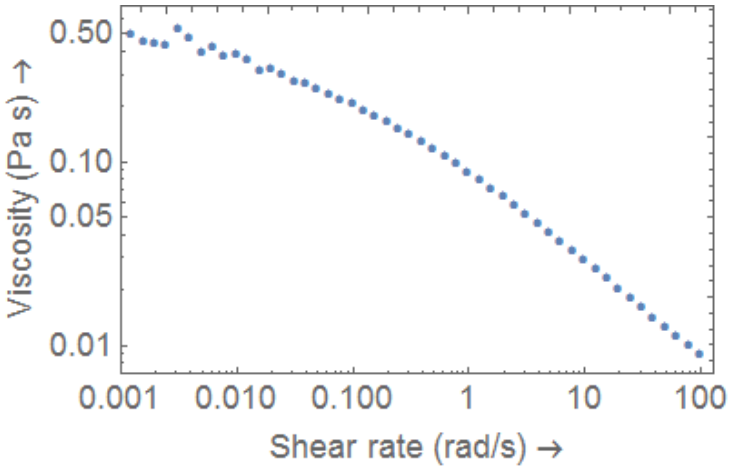


Figure 6.3: Viscosity versus shear rate for a xanthan solution with the same concentration as the sample used in the experiments.

behaviour of colloidal rods in a Poiseuille flow. The experiments were identical to those described above for the magnetic field, except for the sample used and the absence of a magnetic field.

A mixture of non-magnetic silica rods with a length of 3 µm and a diameter of 0.5 µm and the non-adorbing polymer xanthan (Kelzan®) were dispersed in deionised water containing 0.5 mM NaCl and 0.5 mM NaN_3. The volume fraction of xanthan with respect to the overlap concentration in the resulting sample was approximately $\phi_{xan} = 9.19$. The concentration of rods was very low, such that particles are far apart and do not interact with each other.

Whereas for Newtonian fluids the viscosity is not affected by the shear rate, dispersions of xanthan are shear thinning, meaning that the viscosity decreases with increasing shear rate [144]. Figure 6.3 shows a plot of the viscosity versus shear rate for a dispersion with the same concentration as that used in the experiments. The relation between viscosity and shear rate affects the flow profile in a microfluidic channel, where the shear rate is a function of the z-position in the channel.

For a shear-thinning fluid, the flow profile is typically more blunted in the centre of the channel compared to the parabolic profile seen for a Newtonian fluid [145–147]. However, for the flow velocities and xanthan concentration used in these experiments we expect this effect to be minimal.

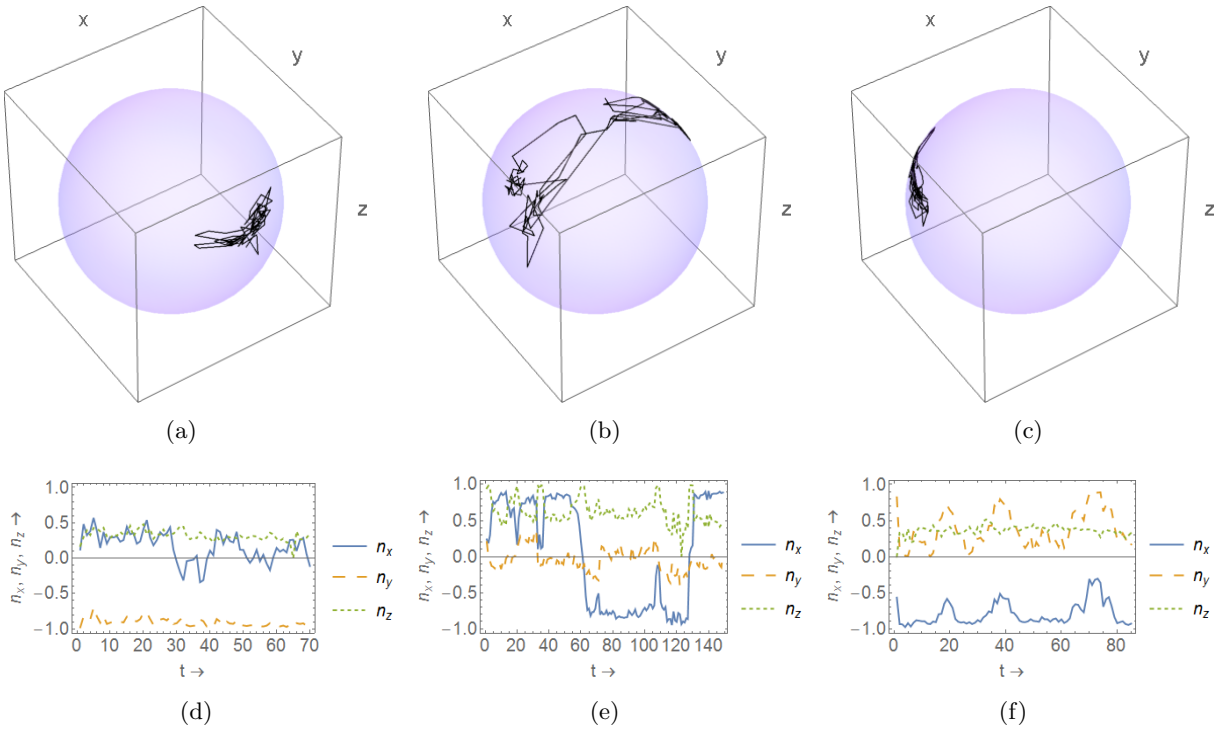


Figure 6.4: The orientation of a rod plotted on a unit sphere for a magnetic field in (a) the x-direction, (b) the y-direction and (c) the z-direction and (d)-(f) the corresponding plots of the x, y and z components.

6.3 Results and discussion

6.3.1 Magnetic field

The orientational behaviour of rods was greatly influenced by the presence of a magnetic field, which essentially suppresses the possible orientations of a rod to a plane. Figure 6.4 shows the orientation of a typical rod plotted on a unit sphere and the corresponding plot of the projections n_x, n_y and n_z for each of the field directions used. Note that n_z is always positive, as we can only determine the absolute value of the orientation in this direction from our experiments.

For a field in the x-direction (flow-direction), particles were found to be mostly oriented in the y-direction, occasionally flipping by 180° in the xz-plane. As can be seen from figure 6.4(a) and (d), there was still some motion in the x-direction, although strongly suppressed compared to the case without a magnetic field (see chapter 5). When a field in the y-direction was applied, rods were seen to tumble in the xz-plane, essentially following a Jeffery orbit with $C = \infty$ (section 5.2). Although this behaviour is predicted by Jeffery theory, we did not observe it in

the experiments without a magnetic field. Again, although the motion in y is strongly suppressed in this case, it is clearly non-zero. If we look more closely at figure 6.4(e), we actually notice that the behaviour of n_y is strongly linked to that of n_x and n_z, which could be an indication that the motion is simply the same as the kayaking seen in the non-magnetic experiments, but strongly suppressed towards the xz-plane. A field in the z-direction confined the particles to the xy-plane, where they were seen to behave seemingly random (Brownian), without following any kind of orbit.

To get a more quantitative idea of the orientational behaviour of rods, orientation distributions were plotted for each field direction. The orientations of all tracked particles in every frame were taken into account. Figure 6.5 shows the orientation distributions calculated in terms of ϕ, the angle between the projection of a rod on the xy-plane and the x-axis, θ, the angle of a rod with the z-axis, and L_p/L, where L_p is the length of a projected rod and L is the actual length of the rod, taken to be the maximum L_p found for each rod. Note that, as explained in the previous chapter, θ and L_p/L are both systematically underestimated due to the nature of the image analysis process.

It can be clearly seen from the orientation distributions that for a magnetic field in the x-direction (on the left in figure 6.5), ϕ has a maximum close to $\frac{\pi}{2}$, which corresponds to an orientation perpendicular to x, as expected in this case. For a magnetic field in y or z, ϕ is peaked around 0, i.e. along the flow-direction, as was the case for rods without a magnetic field. If we look at the distributions of L_p/L, we see that for all cases the distribution has a peak close to one, indicating that particles lie in the xy-plane most of the time. This was also observed for rods without a magnetic field, where we attributed this effect to the high density of silica rods, which results in sedimentation. For a magnetic field in the y-direction, we see a much higher frequency of low values of L_p/L than in any of the other cases, which can be explained by the tumbling motion observed in this case, which forces the rod to orient along the z-axis during the flipping motion.

6.3.2 Non-Newtonian fluid

All tracked particles were found to be aligning with the flow direction, with small fluctuations around this orientation. Figure 6.6 shows the orientation plotted on a unit sphere and the corresponding plot of n_x, n_y and n_z for a typical rod. This is clearly very different from the

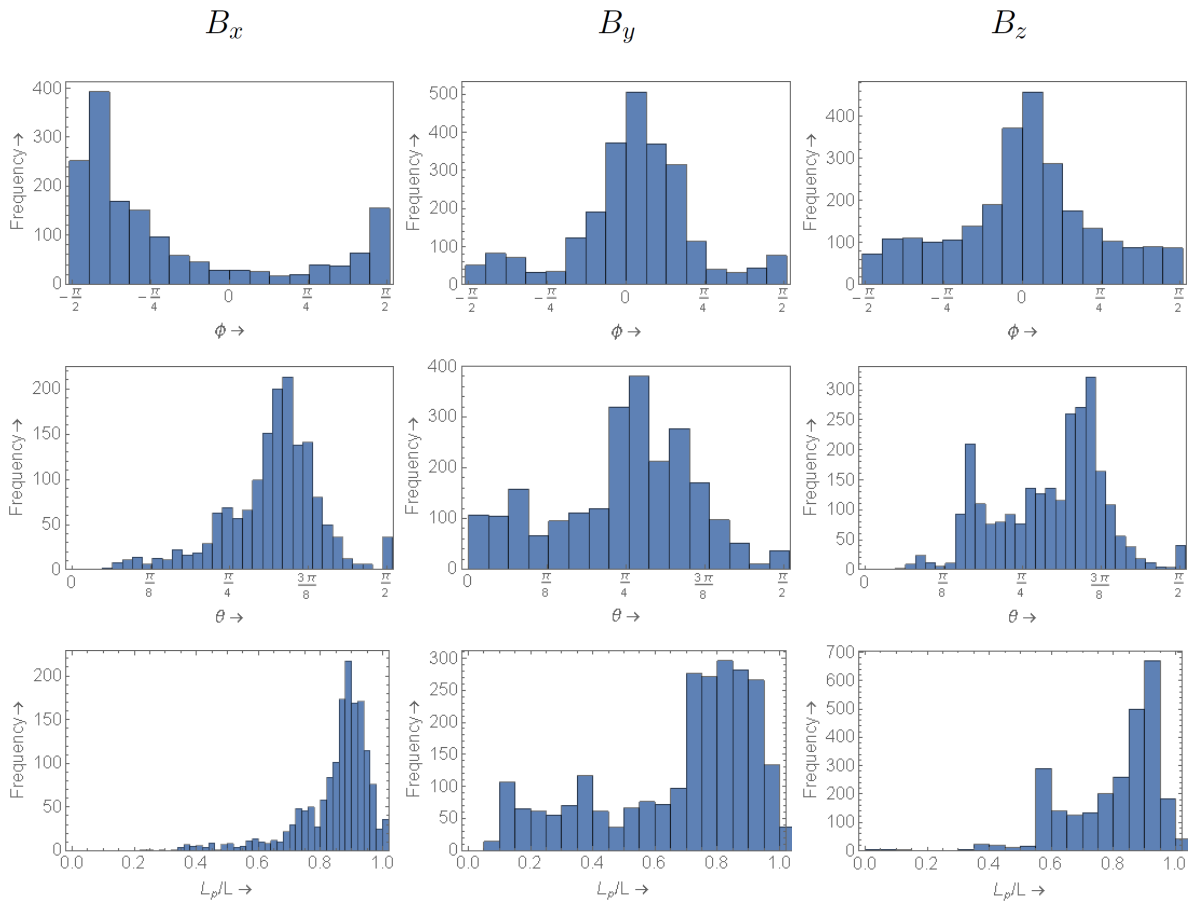
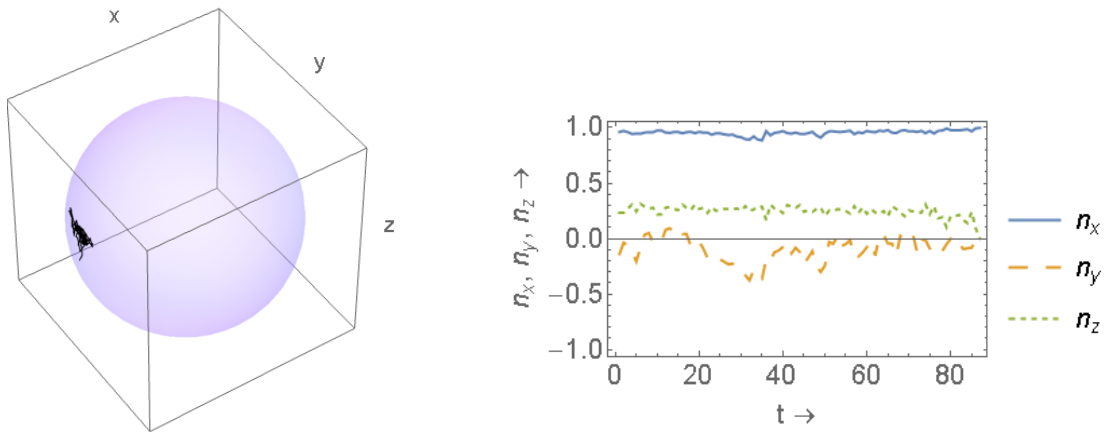
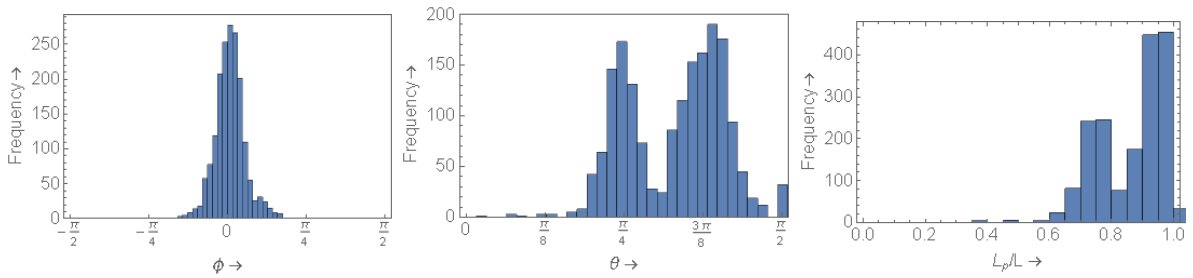


Figure 6.5: Histograms of the orientation distributions for all particles in the experiments with a magnetic field. Top: ϕ, the orientation in the xy-plane, middle; θ, the angle of the particle with the z-axis and bottom; L_p/L. From left to right; a magnetic field in the x, y and z-directions.



(a) (b)

Figure 6.6: (a) The orientation of a rod flowing through a non-Newtonian fluid plotted on a unit sphere and (b) the corresponding plot of the x, y and z components.



(a) (b) (c)

Figure 6.7: Histograms of orientation distributions for all particles in the experiments with a non-Newtonian fluid. (a) ϕ, the orientation in the xy-plane, (b) θ, the angle of the particle with the z-axis and (c) L_p/L.

tumbling and kayaking behaviour seen for a Newtonian fluid in the previous chapter and for the magnetic system.

The orientation distributions in terms of ϕ, θ and L_p/L are shown in figure 6.7. The distribution in ϕ clearly shows a strong peak around $\phi = 0$, which corresponds to the rod aligning with the flow direction. The distributions in θ and L_p/L show two distinct peaks, which may be simply a result of difficulties with the image analysis (see chapter 5). When looking at the rods in the recorded images, they seem to be oriented in the xy-plane most of the time.

Using a non-Newtonian fluid can lead to a different flow profile, and therefore shear rate, than that expected for a Newtonian fluid. However, in the experiments performed we expect this effect to be very small, and therefore this should not significantly change the behaviour of the

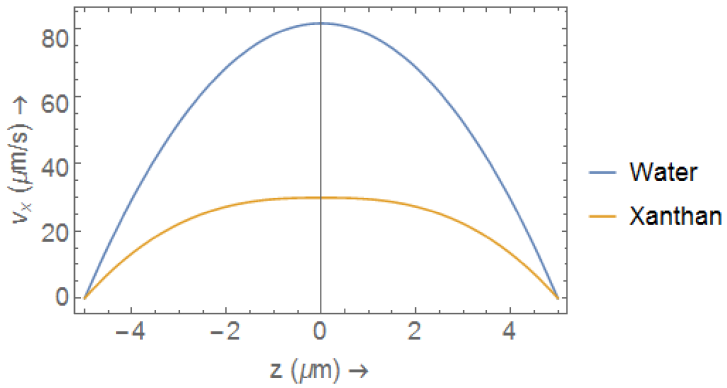
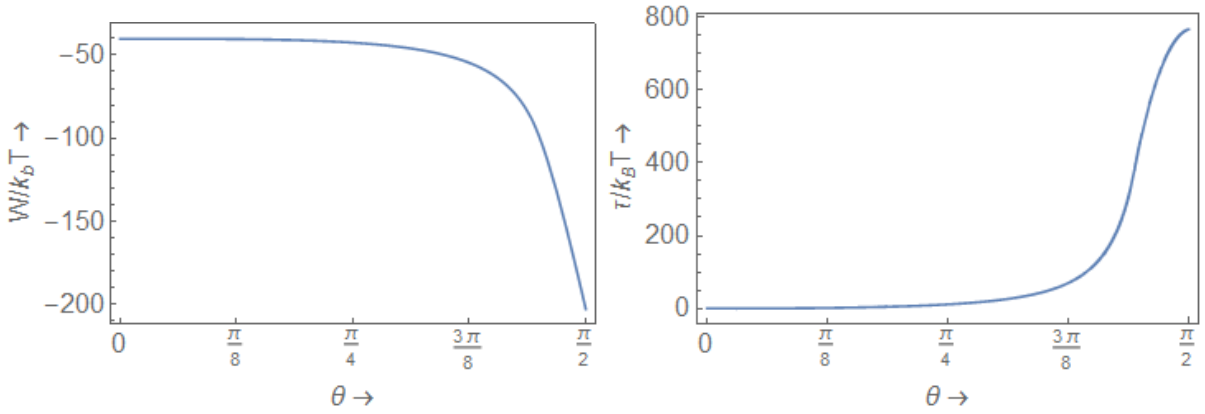


Figure 6.8: Calculated flow profiles for water and for the xanthan solution used in the experiment.



(a) (b)

Figure 6.9: (a) Depletion potential and (b) the resulting torque on a rod, as a function of θ.

rods. Figure 6.8 shows the flow profile in the xz-plane for the channels used in the experiment, calculated by solving the Stokes equation (see section 1.4) using the Cross model [148] for the viscosity; $\eta(z) = \eta_\infty + \frac{\eta_0 - \eta_\infty}{1+(b\dot{\gamma}(z))^m}$, where $\dot{\gamma}(z) = |\frac{\mathrm{d}\vec{u}}{\mathrm{d}z}|$ and the other quantities are obtained from a fit to the data in figure 6.3.

It is possible that the tumbling behaviour is suppressed by a depletion force between a rod and the wall, induced by the presence of xanthan [11,12]. In the most simple model, the strength of the depletion interaction is given by $\frac{W}{k_BT} = -n_b V_{ov}$, with n_b the number density of polymer in the system and V_{ov} the overlap volume of the depletion regions of rod and wall [149]. Figure 6.9 shows the depletion potential and the resulting torque τ on a spheroid as a function of θ, the angle of a rod with the z-axis. The overlap volume was calculated numerically, assuming the rod is in direct contact with the surface. The exact procedures followed for this calculation are described in the appendix. The depletion interaction becomes stronger with increasing θ, as the overlap volume increases. For a rod lying flat on the wall ($\theta = \frac{\pi}{2}$), the depletion interaction

is approximately $\frac{W}{k_B T} \approx -200$. As a rough estimate, the torque exerted by the shear flow is approximately $\tau \approx \eta \dot{\gamma} L^2 D \sim 10$, which is an order of magnitude smaller than the torque exerted by the depletion interaction (figure 6.9(b)). The depletion interaction is clearly very strong in this system, which can explain the absence of any tumbling.

It is not clear why the rods prefer to orient along the direction of flow. As the rods are flowing through the channel together with the surrounding fluid, friction forces should not play a significant role. A possible explanation would be that the shear flow causes polymer molecules to slightly stretch out along the direction of flow, which could then affect the orientation of the colloidal rod. We plan to perform simulations on this system, similar to those described in the previous chapter, in order to better understand the results found.

6.4 Conclusion

The behaviour of silica rods in a Poiseuille flow is influenced greatly both by the presence of an external magnetic field and by using a non-Newtonian fluid. In the experiments with a magnetic field we observed kayaking and tumbling behaviour that was somewhat similar to that seen in chapter 5, but suppressed towards the plane perpendicular to the magnetic field. In the case of a non-Newtonian fluid, rods were seen to align with the direction of flow. The absence of tumbling behaviour can be explained by the depletion interaction between rods and the wall, induced by the presence of xanthan. However, it is unclear why the rods prefer to orient along the flow direction. We plan to perform simulations, similar to those used in the previous chapter, in order to get a better insight in these results.

Acknowledgements

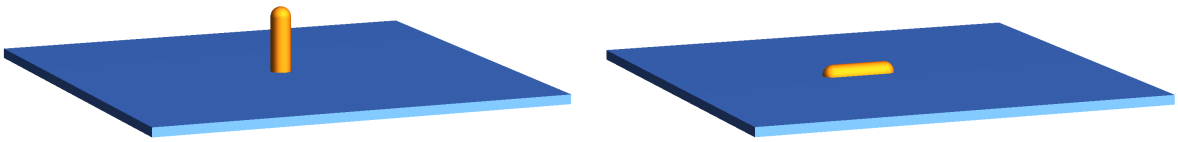
We would like to thank Dr. Yonxiang Gao for synthesising the silica rods used in these experiments and Michael Mordan for allowing the use of his xanthan stock solution and rheological data.

Appendix: Calculation of the overlap volume

The overlap volume between a spheroid and a flat surface was calculated numerically using Mathematica^{TM} which has useful in-built functions to do this.

First, the region of the surface and the corresponding depletion region was defined as a large cuboid with dimensions $-10\,\mu m \leq x, y \leq 10\,\mu m$ and $-R_g \leq z \leq R_g$, where $R_g = 222\,nm$ is the radius of gyration of the xanthan polymer. To define a spheroid, we used the function *RegionUnion* to combine a cylinder of length $L - D$ and radius $\frac{D}{2} + R_g$, where L and D are the length and diameter of the silica rods respectively, and two spheres with radius $\frac{D}{2} + R_g$, placed at the two ends of the cylinder. This results in a spheroid that corresponds to the rod and its surrounding depletion layer.

In order to incorporate the orientation of the spheroid, the two spheres were placed at positions $(0, 0, \frac{D}{2})$ and $((L - D)\sin\theta, 0, \frac{D}{2} + (L - D)\cos\theta)$, with the cylinder spanning between them. Here, θ is the angle of the spheroid with the z-axis. Figure 6.10 shows images of the excluded regions around the spheroid and surface for $\theta = 0$ and $\theta = \frac{\pi}{2}$. The overlap regions are clearly quite large compared to the rod, as can be seen in figure 6.10(b), where only slightly more than half the spheroid is still visible above the surface.



(a) (b)

Figure 6.10: Spheroid and surface generated in order to calculate the overlap volume of their depletion layers. (a) for $\theta = 0$ and (b) for $\theta = \frac{\pi}{2}$.

The overlap volume V_{ov} between two regions was finally calculated using the in-built functions *RegionIntersection* and *RegionMeasure*. To ensure this calculation is correct for all values of $0 \leq \theta \leq \pi$, the overlap volume for $\theta > \frac{\pi}{2}$ was defined as $V_{ov}(\pi - \theta)$. This is necessary in order to correctly calculate the torque, which involves the derivative of the overlap volume.

Summary

In this thesis we study colloidal rods in confinement and under flow. The size of colloids makes them ideal as model systems, as physical processes take place on an accessible timescale ($\sim 1\,\mathrm{s}$) and due to their size they can easily be imaged using optical microscopy techniques. We study both concentrated, liquid crystalline suspensions (chapters 3 and 4) and very dilute samples (chapters 5 and 6) of rods, observing the samples on the single particle level. Throughout this thesis we combine experiments with theory and simulations in order to obtain a better understanding of the underlying physics involved in the observed behaviour.

In chapter 1 we introduced some of the important concepts in this thesis. We started by discussing colloids and some of their important properties, such as Brownian motion. We then briefly introduced liquid crystals, focussing on nematic liquid crystals and the isotropic-nematic phase transition. Finally, the effects of confinement and more specifically flow in confinement were discussed. The two model systems used in this thesis and some of the experimental techniques were discussed in more detail in chapter 2.

In chapter 3 we described a mathematical method to calculate distortion energies in a nematic liquid crystal from single-particle data. We used a triangulation of particle positions, followed by a linear interpolation of the particle orientations in order to obtain a continuous expression of the director field, from which the distortion energy can easily be calculated. We illustrated this method by applying it to both artificial data and experimental results for *fd*-virus particles confined in wedges with different opening angles.

We continued the theme of liquid crystals in chapter 4, where we discussed the first observation of a capillary nematisation in a colloidal liquid crystal. We confined an isotropic suspension of *fd*-virus particles using microfluidic channels of different heights and examined the phase behaviour using confocal microscopy. We observed a capillary nematisation transition in

the channel with strongest confinement. The results were compared to two different theories, the Zwanzig model and a more elaborate DFT model for semiflexible rods, and both were found to be in good agreement with experiments. The DFT model was found to have a better quantitative agreement, which can be explained by the fact that in this model the orientation of rods is unrestricted and rod flexibility is taken into account.

Chapters 5 and 6 concern the orientational motion of silica rods in a Poiseuille flow. In chapter 5 we explored the simplest case of non-magnetic rods in demineralised water. We observed kayaking and xy-tumbling motions for most rods, which was not periodic and would switch from one type of motion to the other at seemingly random moments. We compared our results to Jeffery's theory for non-Brownian rods in a linear shear flow and to multi-particle collision dynamics (MPC) simulations. The experimental results showed the same type of behaviour as predicted by Jeffery's theory, but without periodicity, and particles were often seen to switch from one type of behaviour to another. The MPC simulations showed very similar results to those found in the experiment, indicating that Brownian motion can indeed explain the deviations from Jeffery theory.

Chapter 6 explores the effects of an external magnetic field and the use of a non-Newtonian fluid as a medium on the orientational behaviour of rods flowing through a Poiseuille flow. In the case of the magnetic field, we observed orientational motions similar to those found in chapter 5, but suppressed towards the plane perpendicular to the magnetic field. For the non-Newtonian fluid, particles were found to align with the direction of flow. In this case, the absence of any tumbling behaviour can be explained by the depletion interaction between rods and the wall. It was not clear, however, why the preferred orientation of the rods is to align with the flow direction. In order to get a better insight in this behaviour, we plan to perform simulations in the future, similar to those described in chapter 5.

Bibliography

[1] Wilson Poon. Colloids as big atoms. *Science*, 304(5672):830–831, 2004.

[2] P. N. Pusey and W. van Megen. Phase behaviour of concentrated suspensions of nearly hard colloidal spheres. *Nature*, 320:340–342, 1986.

[3] A. Vrij, E. A. Nieuwenhuis, H. M. Fijnaut, and W. G. M. Agterof. Application of modern concepts in liquid state theory to concentrated particle dispersions. *Faraday Discuss. Chem. Soc.*, 65:101–113, 1978.

[4] D. H Everett. *Basic Principles of Colloid Science*. The Royal Society of Chemistry, London, 1988.

[5] A. Einstein. Über die von der molekularkinetischen theorie der wärme geforderte bewegung von in ruhenden flüßigkeiten suspendierten teilchen. *Annalen der Physik*, 322(8):549–560, 1905.

[6] Albert Einstein. *Investigations on the Theory of the Brownian Movement*. Dover, New York, 1956. Edited with notes by R. Fürth, Translated by A. D. Cowper.

[7] Jean Perrin. Mouvement brownien et réalité moléculaire. *Annales de Chimie et de Physique*, 18:5–104, 1909.

[8] Jean Perrin. *Les Atomes*. Librairie Félix Alcan, Paris, 1913.

[9] Christina Graf, Dirk L. J. Vossen, Arnout Imhof, and Alfons van Blaaderen. A general method to coat colloidal particles with silica. *Langmuir*, 19(17):6693–6700, 2003.

[10] Daniela J. Kraft, Ran Ni, Frank Smallenburg, Michiel Hermes, Kisun Yoon, David A. Weitz, Alfons van Blaaderen, Jan Groenewold, Marjolein Dijkstra, and Willem K. Kegel. Surface roughness directed self-assembly of patchy particles into colloidal micelles. *Proceedings of the National Academy of Sciences*, 109(27):10787–10792, 2012.

[11] S. Asakura and F. Oosawa. On interaction between two bodies immersed in a solution of macromolecules. *The Journal of Chemical Physics*, 22(7):1255–1256, 1954.

[12] A. Vrij. Polymers at interfaces and the interactions in colloidal dispersions. *Pure and Applied Chemistry*, 48:471–483, 1976.

[13] A. van Blaaderen and A. Vrij. Synthesis and characterization of colloidal dispersions of fluorescent, monodisperse silica spheres. *Langmuir*, 8(12):2921–2931, 1992.

[14] Eugenia Kumacheva, Olga Kalinina, and Lothar Lilge. Three-dimensional arrays in polymer nanocomposites. *Advanced Materials*, 11(3):231–234, 1999.

[15] R. H. Pelton and P. Chibante. Preparation of aqueous latices with n-isopropylacrylamide. *Colloids and Surfaces*, 20(3):247–256, 1986.

[16] Eric B. Mock, Hank De Bruyn, Brian S. Hawkett, Robert G. Gilbert, and Charles F. Zukoski. Synthesis of anisotropic nanoparticles by seeded emulsion polymerization. *Langmuir*, 22(9):4037–4043, 2006.

[17] Zvonimir Dogic and Seth Fraden. *Soft Matter*, volume 2, chapter Phase Behavior of Rod-Like Viruses and Virus-Sphere Mixtures, pages 1–86. Wiley-VCH Verlag GmbH & Co. KGaA, 1st edition, 2007.

[18] Anke Kuijk, Alfons van Blaaderen, and Arnout Imhof. Synthesis of monodisperse, rodlike silica colloids with tunable aspect ratio. *Journal of the American Chemical Society*, 133(8):2346–2349, 2011.

[19] Yong Wang, Xiaowen Su, Panshuang Ding, Shan Lu, and Huaping Yu. Shape-controlled synthesis of hollow silica colloids. *Langmuir*, 29(37):11575–11581, 2013.

[20] Laura Rossi, Stefano Sacanna, William T. M. Irvine, Paul M. Chaikin, David J. Pine, and Albert P. Philipse. Cubic crystals from cubic colloids. *Soft Matter*, 7:4139–4142, 2011.

[21] Julius W. J. de Folter, Eline M. Hutter, Sonja I. R. Castillo, Kira E. Klop, Albert P. Philipse, and Willem K. Kegel. Particle shape anisotropy in pickering emulsions: Cubes and peanuts. *Langmuir*, 30(4):955–964, 2014.

[22] Daniela J. Kraft, Jan Hilhorst, Maria A. P. Heinen, Mathijs J. Hoogenraad, Bob Luigjes, and Willem K. Kegel. Patchy polymer colloids with tunable anisotropy dimensions. *The Journal of Physical Chemistry B*, 115(22):7175–7181, 2011.

[23] Andreas Walther and Axel H. E. Mller. Janus particles: Synthesis, self-assembly, physical properties, and applications. *Chemical Reviews*, 113(7):5194–5261, 2013.

[24] J. Christopher Love, Byron D. Gates, Daniel B. Wolfe, Kateri E. Paul, and George M. Whitesides. Fabrication and wetting properties of metallic half-shells with submicron diameters. *Nano Letters*, 2(8):891–894, 2002.

[25] S. Sacanna, W. T. M. Irvine, P. M. Chaikin, and D. J. Pine. Lock and key colloids. *Nature*, 464:575–578, 2010.

[26] P. G. de Gennes. *The physics of liquid crystals.* Clarendon Press, Oxford, 1974.

[27] Michael J. Stephen and Joseph P. Straley. Physics of liquid crystals. *Rev. Mod. Phys.*, 46:617–704, Oct 1974.

[28] S. Chandrasekhar. *Liquid Crystals*. Cambridge University Press, Cambridge, 2^{nd} edition, 1992.

[29] F. Reinitzer. Beiträge zur kenntnis des cholesterins. *Monatshefte für Chemie*, 9:421–441, 1888.

[30] O. Lehmann. Über fließende krystalle. *Zeitschrift für Physikalische Chemie*, 4:462–472, 1889.

[31] H. Zocher. Über freiwillige strukturbildung in solen. (eine neue art anisotrop flssiger medien.). *Zeitschrift für anorganische und allgemeine Chemie*, 147(1):91–110, 1925.

[32] A. S. Sonin. Inorganic lyotropic liquid crystals. *J. Mater. Chem.*, 8:2557–2574, 1998.

[33] J.-C. P. Gabriel and P. Davidson. New trends in colloidal liquid crystals based on mineral moieties. *Advanced Materials*, 12(1):9–20, 2000.

[34] Irving Langmuir. The role of attractive and repulsive forces in the formation of tactoids, thixotropic gels, protein crystals and coacervates. *The Journal of Chemical Physics*, 6(12):873–896, 1938.

[35] Felix M. van der Kooij, , and Henk N. W. Lekkerkerker. Formation of nematic liquid crystals in suspensions of hard colloidal platelets. *The Journal of Physical Chemistry B*, 102(40):7829–7832, 1998.

[36] P. A. Buining and H. N. W. Lekkerkerker. Isotropic-nematic phase separation of a dispersion of organophilic boehmite rods. *The Journal of Physical Chemistry*, 97(44):11510–11516, 1993.

[37] Seth Fraden. Phase transitions in colloidal suspensions of virus particles. In Marc Baus, Luis F. Rull, and Jean-Paul Ryckaert, editors, *Observation, Prediction and Simulation of Phase Transitions in Complex Fluids*. Springer Netherlands, Dordrecht, 1995.

[38] Françoise Livolant. Ordered phases of dna in vivo and in vitro. *Physica A: Statistical Mechanics and its Applications*, 176(1):117–137, 1991.

[39] Lars Onsager. The effects of shape on the interaction of colloidal particles. *Annals of the New York Academy of Sciences*, 51(4):627–659, 1949.

[40] G.J. Vroege and H. N. W. Lekkerkerker. Phase transitions in lyotropic colloidal and polymer liquid crystals. *Reports on Progress in Physics*, 55(8):1241, 1992.

[41] Joseph Edward Mayer and Maria Goeppert Mayer. *Statistical Mechanics*. Wiley, New York, 1940.

[42] Daan Frenkel. Onsager's spherocylinders revisited. *The Journal of Physical Chemistry*, 91(19):4912–4916, 1987.

[43] Theo Odijk. Theory of lyotropic polymer liquid crystals. *Macromolecules*, 19(9):2313–2329, 1986.

[44] C. W. Oseen. The theory of liquid crystals. *Transactions of the Faraday Society*, 29:883–899, 1933.

[45] F. C. Frank. I. liquid crystals. on the theory of liquid crystals. *Discussions of the Faraday Society*, 25:19–28, 1958.

[46] G. Barbero, A. Sparavigna, and A. Strigazzi. The structure of the distortion free-energy density in nematics: Second-order elasticity and surface terms. *Il Nuovo Cimento D*, 12(9):1259–1272, 1990.

[47] Victor G. Taratuta, Alan J. Hurd, and Robert B. Meyer. Light-scattering study of a polymer nematic liquid crystal. *Physical Review Letters*, 55:246–249, Jul 1985.

[48] Victor G. Taratuta, Franklin Lonberg, and Robert B. Meyer. Anisotropic mechanical properties of a polymer nematic liquid crystal. *Physical Review A*, 37:1831–1834, 1988.

[49] Sin-Doo Lee and Robert B. Meyer. Computations of the phase equilibrium, elastic constants, and viscosities of a hard-rod nematic liquid crystal. *The Journal of Chemical Physics*, 84(6):3443–3448, 1986.

[50] Alfred Saupe. Disclinations and properties of the directorfield in nematic and cholesteric liquid crystals. *Molecular Crystals and Liquid Crystals*, 21(3-4):211–238, 1973.

[51] S. Mkaddem and E. C. Gartland, Jr. Fine structure of defects in radial nematic droplets. *Physical Review E*, 62:6694–6705, 2000.

[52] H. Löwen. Twenty years of confined colloids: from confinement-induced freezing to giant breathing. *Journal of Physics: Condensed Matter*, 21(47):474203, 2009.

[53] K. Binder. Phase transitions in reduced geometry. *Annual Review of Physical Chemistry*, 43:33–59, 1992.

[54] C. Alba-Simionesco, B. Coasne, G. Dosseh, G. Dudziak, K. E. Gubbins, E. Radhakrishnan, and M. Sliwinska-Bartkowiak. Effects of confinement on freezing and melting. *Journal of Physics: Condensed Matter*, 18(6):R15–R68, 2006.

[55] A. Majumdar, C. J. P. Newton, J. M. Robbins, and M. Zyskin. Topology and bistability in liquid crystal devices. *Phys. Rev. E*, 75:051703, May 2007.

[56] A. J. Davidson, C. V. Brown, N. J. Mottram, S. Ladak, and C. R. Evans. Defect trajectories and domain-wall loop dynamics during two-frequency switching in a bistable azimuthal nematic device. *Phys. Rev. E*, 81:051712, May 2010.

[57] Margaret S. Cheung, Dmitri Klimov, and D. Thirumalai. Molecular crowding enhances native state stability and refolding rates of globular proteins. *Proceedings of the National Academy of Sciences of the United States of America*, 102(13):4753–4758, 2005.

[58] Ercan Kamber. *Statistical physics of crowding and confinement.* PhD thesis, Brandeis University, 2008.

[59] Tina L. Lamers and Beth L. Pruitt. The mems design process. In Reza Ghodssi and Pinyen Lin, editors, *MEMS Materials and Processes Handbook.* Springer, Boston, 2011.

[60] Patrick Tabeling. *Introduction to Microfluidics.* Oxford University Press, Oxford, 2005.

[61] A. Manz, N. Graber, and H. M. Widmer. Miniaturized total chemical analysis systems: A novel concept for chemical sensing. *Sensors and Actuators B: Chemical*, 1(1):244–248, 1990.

[62] Peter Wilding, Mann A. Shoffner, and Larry J. Kricka. Pcr in a silicon microstructure. *Clinical Chemistry*, 40(9):1815–1818, 1994.

[63] Jan C. T.l Eijke, Albert Prak, Simon Cowen, Derek H. Craston, and Andreas Manz. Micromachined heated chemical reactor for pre-column derivatisation. *Journal of Chromatography A*, 815(2):265–271, 1998.

[64] Lev D. Gelb, K. E. Gubbins, R. Radhakrishnan, and M Sliwinska-Bartkowiak. Phase separation in confined systems. *Reports on Progress in Physics*, 62(12):1573–1659, 1999.

[65] J. M. Kosterlitz and D. J. Thouless. Long range order and metastability in two dimensional solids and superfluids. (application of dislocation theory). *Journal of Physics C: Solid State Physics*, 5(11):L124, 1972.

[66] David R. Nelson and B. I. Halperin. Dislocation-mediated melting in two dimensions. *Phys. Rev. B*, 19:2457–2484, 1979.

[67] Etienne P. Bernard and Werner Krauth. Two-step melting in two dimensions: First-order liquid-hexatic transition. *Phys. Rev. Lett.*, 107:155704, Oct 2011.

[68] O. J. Dammone, I. Zacharoudiou, R. P. A. Dullens, J. M. Yeomans, M. P. Lettinga, and D. G. A. L. Aarts. Confinement induced splay-to-bend transition of colloidal rods. *Physical Review Letters*, 109:108303, 2012.

[69] Alexander H. Lewis, Ioana Garlea, Jose Alvarado, Oliver J. Dammone, Peter D. Howell, Apala Majumdar, Bela M. Mulder, M. P. Lettinga, Gijsje H. Koenderink, and Dirk G. A. L. Aarts. Colloidal liquid crystals in rectangular confinement: theory and experiment. *Soft Matter*, 10:7865–7873, 2014.

[70] Ioana C. Gârlea, Pieter Mulder, José Alvarado, Oliver Dammone, Dirk G. A. L. Aarts, M. Pavlik Lettinga, Gijsje H. Koenderink, and Bela M. Mulder. Finite particle size drives defect-mediated domain structures in strongly confined colloidal liquid crystals. *Nature Communications*, 7:12112, 2016.

[71] J. Klafter and J. M. Drake. *Molecular dynamics in restricted geometries.* Wiley, New York, 1989.

[72] H. Ogawa, T. Kanayac, K. Nishida, and G. Matsuba. Phase separation and dewetting in polymer blend thin films. *The European Physical Journal Special Topics*, 141(1):189–192, 2007.

[73] N. Ioannou, H. Liu, and Y. H. Zhang. Droplet dynamics in confinement. *Journal of Computational Science*, pages –, 2016.

[74] E. A. G. Jamie, R. P. A. Dullens, and D. G. A. L. Aarts. Fluidfluid demixing of off-critical colloidpolymer systems confined between parallel plates. *Journal of Physics: Condensed Matter*, 24(28):284120, 2012.

[75] Ronald F. Probstein. *Physicochemical Hydrodynamics: An Introduction*. John Wiley & Sons, Inc., Hoboken, second edition edition, 2005.

[76] G. B. Jeffery. The motion of ellipsoidal particles immersed in a viscous fluid. *Proceedings of the Royal Society of London A: Mathematical, Physical and Engineering Sciences*, 102(715):161–179, 1922.

[77] D. A. Marvin and H. Hoffmann-Berling. Physical and chemical properties of two new small bacteriophages. *Nature*, 197:517–518, 1963.

[78] Ying A. Wang, Xiong Yu, Stacy Overman, Masamichi Tsuboi, George J. Thomas Jr., and Edward H. Egelman. The structure of a filamentous bacteriophage. *Journal of Molecular Biology*, 361(2):209–215, 2006.

[79] Zvonimir Dogic and Seth Fraden. Ordered phases of filamentous viruses. *Current Opinion in Colloid & Interface Science*, 11(1):47–55, 2006.

[80] Eric Grelet, M Paul Lettinga, Markus Bier, René van Roij, and Paul van der Schoot. Dynamical and structural insights into the smectic phase of rod-like particles. *Journal of Physics: Condensed Matter*, 20(49):494213, 2008.

[81] Robert J. Hunter. *Foundations of Colloid Science*. Oxford University Press, Oxford, 2^{nd} edition, 2000.

[82] Y. Gao, B. Peng, R. P. A. Dullens, and D. G. A. L. Aarts. (to be published).

[83] Denis Bartolo, Guillaume Degré, Philippe Nghe, and Vincent Studer. Microfluidic stickers. *Lab Chip*, 8:274–279, 2008.

[84] Richard P. Feynman, Robert B. Leighton, and Matthew L. Sands. *The Feynman Lectures on Physics*, volume I. Addison-Wesley, Boston, definitive edition, 2006.

[85] Robert H Webb. Confocal optical microscopy. *Reports on Progress in Physics*, 59(3):427–471, 1996.

[86] Tony Wilson. *Confocal Microscopy*. Academic Press, London, 1990.

[87] Roel P. A. Dullens. *Structure and dynamics of colloidal hard spheres in real-space*. PhD thesis, Utrecht University, 2005.

[88] Max Born and Emil Wolf. *Principles of Optics*. Cambridge University Press, Cambridge, 7^{th} (expanded) edition, 1999.

[89] A. A. Verhoeff, I. A. Bakelaar, R. H. J. Otten, P. van der Schoot, and H. N. W. Lekkerkerker. Tactoids of plate-like particles: Size, shape, and director field. *Langmuir*, 27(1):116–125, 2011.

[90] Yong Geng, David Seč, Pedro L. Almeida, Oleg D. Lavrentovich, Slobodan Žumer, and Maria H. Godinho. Liquid crystal necklaces: cholesteric drops threaded by thin cellulose fibres. *Soft Matter*, 9:7928–7933, 2013.

[91] R. M. W. van Bijnen, R. H. J. Otten, and P. van der Schoot. Texture and shape of two-dimensional domains of nematic liquid crystals. *Physical Review E*, 86:051703, 2012.

[92] T. Brunet, O. Thiebaut, E. Charlet, H. Bock, J. Kelber, and E. Grelet. Anchoring transition in confined discotic columnar liquid crystal films. *Europhysics Letters*, 93:16004, 2011.

[93] Delaunay, B. Sur la sphère vide. a la mémoire de georges voronoi. *Bulletin de l'Académie des Sciences de l'URSS. Classe des sciences mathématiques et naturelles*, 7:793–800, 1934.

[94] M. de Berg, O. Cheong, M. van Kreveld, and M. Overmars. *Computational Geometry*. Springer-Verlag, Heidelberg, 3^{rd} edition, 2008.

[95] A. J. Davidson and N. J. Mottram. Conformal mapping techniques for the modelling of liquid crystal devices. *European Journal of Applied Mathematics*, 23:99–119, 2012.

[96] Jianxing Tang and Seth Fraden. Isotropic-cholesteric phase transition in colloidal suspensions of filamentous bacteriophage fd. *Liquid Crystals*, 19(4):459–467, 1995.

[97] Z. Dogic and S. Fraden. Cholesteric Phase in Virus Suspensions. *Langmuir*, 16:7820–7824, 2000.

[98] Mark J. Zakhary, Prerna Sharma, Andrew Ward, Sevim Yardimici, and Zvonimir Dogic. Geometrical edgeactants control interfacial bending rigidity of colloidal membranes. *Soft Matter*, 9:8306–8313, 2013.

[99] Eric Grelet. Hexagonal order in crystalline and columnar phases of hard rods. *Physical Review Letters*, 100:168301, 2008.

[100] D Guu, J. K. G. Dhont, G. A. Vliegenthart, and M. P. Lettinga. Depletion induced clustering in mixtures of colloidal spheres and fd-virus. *Journal of Physics: Condensed Matter*, 24(46):464101, 2012.

[101] F. Tombolato, A. Ferrarini, and E. Grelet. Chiral nematic phase of suspensions of rodlike viruses: Left-handed phase helicity from a right-handed molecular helix. *Physical Review Letters*, 96:258302, 2006.

[102] Edward Barry, Daniel Beller, and Zvonimir Dogic. A model liquid crystalline system based on rodlike viruses with variable chirality and persistence length. *Soft Matter*, 5:2563–2570, 2009.

[103] M. Paul Lettinga and Eric Grelet. Self-diffusion of rodlike viruses through smectic layers. *Physical Review Letters*, 99:197802, Nov 2007.

[104] R. Aliabadi, M. Moradi, and S. Varga. Orientational ordering of confined hard rods: The effect of shape anisotropy on surface ordering and capillary nematization. *Phys. Rev. E*, 92:032503, Sep 2015.

[105] Oliver J. Dammone, Ioannis Zacharoudiou, Roel P. A. Dullens, Julia M. Yeomans, M. P. Lettinga, and Dirk G. A. L. Aarts. Confinement induced splay-to-bend transition of colloidal rods. *Phys. Rev. Lett.*, 109:108303, Sep 2012.

[106] Matthew L. Blow, Sumesh P. Thampi, and Julia M. Yeomans. Biphasic, lyotropic, active nematics. *Phys. Rev. Lett.*, 113:248303, Dec 2014.

[107] Simone Dussi, Simone Belli, René van Roij, and Marjolein Dijkstra. Cholesterics of colloidal helices: Predicting the macroscopic pitch from the particle shape and thermodynamic state. *The Journal of Chemical Physics*, 142(7):074905, 2015.

[108] Thomas Geigenfeind, Sebastian Rosenzweig, Matthias Schmidt, and Daniel de las Heras. Confinement of two-dimensional rods in slit pores and square cavities. *The Journal of Chemical Physics*, 142(17):174701, 2015.

[109] Marina Soares e Silva, José Alvarado, Jeanette Nguyen, Nefeli Georgoulia, Bela M. Mulder, and Gijsje H. Koenderink. Self-organized patterns of actin filaments in cell-sized confinement. *Soft Matter*, 7:10631–10641, 2011.

[110] Alejandro D. Rey. Liquid crystal models of biological materials and processes. *Soft Matter*, 6:3402–3429, 2010.

[111] José Alvarado, Bela M. Mulder, and Gijsje H. Koenderink. Alignment of nematic and bundled semiflexible polymers in cell-sized confinement. *Soft Matter*, 10:2354–2364, 2014.

[112] Daniel T. Kulp and Judith Herzfeld. Crowding-induced organization of cytoskeletal elements. iii. spontaneous bundling and sorting of self-assembled filaments with different flexibilities. *Biophysical Chemistry*, 57(1):93–102, 1995. Macromolecular Crowding.

[113] Judith Herzfeld. Crowding-induced organization in cells: spontaneous alignment and sorting of filaments with physiological control points. *Journal of Molecular Recognition*, 17(5):376–381, 2004.

[114] Ping Sheng. Phase transition in surface-aligned nematic films. *Phys. Rev. Lett.*, 37:1059–1062, October 1976.

[115] A. Poniewierski and T. J. Sluckin. Theory of the Nematic-Isotropic Transition in a Restricted Geometry. *Liq. Cryst.*, 2(3):281–311, 1987.

[116] K. Kočevar, A. Borštnik, I. Muševič, and S. Žumer. Capillary condensation of a nematic liquid crystal observed by force spectroscopy. *Phys. Rev. Lett.*, 86:5914–5917, 2001.

[117] R. van Roij, M. Dijkstra, and R. Evans. Orientational wetting and capillary nematization of hard-rod fluids. *Europhys. Lett.*, 49(3):350–356, 2000.

[118] René van Roij, Marjolein Dijkstra, and Robert Evans. Interfaces, wetting, and capillary nematization of a hard-rod fluid: Theory for the zwanzig model. *J. Chem. Phys.*, 113(17):7689–7701, 2000.

[119] Ioana C. Gârlea and Bela M. Mulder. Defect structures mediate the isotropicnematic transition in strongly confined liquid crystals. *Soft Matter*, 11:608–614, 2015.

[120] V. A. Ivanov, A. S. Rodionova, J. A. Martemyanova, M. R. Stukan, M. Müller, W. Paul, and K. Binder. Wall-induced orientational order in athermal semidilute solutions of semiflexible polymers: Monte carlo simulations of a lattice model. *Journal of Chemical Physics*, 138:234903, 2013.

[121] Hendrik Reich and Matthias Schmidt. Capillary nematization of hard colloidal platelets confined between two parallel hard walls. *Journal of Physics: Condensed Matter*, 19(32):326103, 2007.

[122] Jeff Z.Y. Chen. Theory of wormlike polymer chains in confinement. *Progress in Polymer Science*, 5455:3–46, 2016.

[123] Shiwei Ye, Pingwen Zhang, and Jeff Z. Y. Chen. Surface-induced phase transitions of wormlike chains in slit confinement. *Soft Matter*, 12:2948–2959, 2016.

[124] Dmytro A. Luzhbin and Yeng-Long Chen. Shifting the isotropic-nematic transition in very strongly confined semiflexible polymer solutions. *Macromolecules*, 49(16):6139–6147, 2016.

[125] Thomas Troppenz, Anke Kuijk, Arnout Imhof, Alfons van Blaaderen, Marjolein Dijkstra, and René van Roij. Nematic ordering of polarizable colloidal rods in an external electric field: theory and experiment. *Phys. Chem. Chem. Phys.*, 17:22423–22430, 2015.

[126] Robert Zwanzig. First Order Phase Transition in a Gas of Long Thin Rods. *J. Chem. Phys.*, 39(7):1714–1721, 1963.

[127] S. A. Egorov, A. Milchev, P. Virnau, and K. Binder. Semiflexible polymers under good solvent conditions interacting with repulsive walls. *Journal of Chemical Physics*, 144:174902, 2016.

[128] A. Okagawa and S. G. Mason. The kinetics of flowing dispersions. vii. oscillatory behavior of rods and discs in shear flow. *Journal of Colloid and Interface Science*, 45(2):330–358, 1973.

[129] Y. Ivanov, T. G. M. van de Ven, and S. G. Mason. Damped oscillations in the viscosity of suspensions of rigid rods .1. monomodal suspensions. *Journal of Rheology*, 26:213–230, 1982.

[130] M. Zuzovsky, Z. Priel, and S.G. Mason. Memory impairment in flowing suspensions. iii. brownian rotation of spheroids. *Journal of Colloid and Interface Science*, 75(1):230–239, 1980.

[131] E. Anczurowski, R. G. Cox, and S. G. Mason. The kinetics of flowing dispersions: Iv. transient orientations of cylinders. *Journal of Colloid and Interface Science*, 23(4):547–562, 1967.

[132] Y. Ivanov and T. G. M. van de Ven. Damped oscillations in the viscosity of suspensions of rigid rods .2. bimodal and polydisperse suspensions. *Journal of Rheology*, 26:231–244, 1982.

[133] C. M. Cerda, R. T. Foister, and S. G. Mason. Rheooptical transients in sheared suspensions. 1. mono- and bimodal suspensions of spheroids. *The Journal of Physical Chemistry*, 85(8):1075–1086, 1981.

[134] A. Okagawa, R. G. Cox, and S. G. Mason. The kinetics of flowing dispersions. vi. transient orientation and rheological phenomena of rods and discs in shear flow. *Journal of Colloid and Interface Science*, 45(2):303–329, 1973.

[135] A. Karnis, H. L. Goldsmith, and S. G. Mason. The flow of suspensions through tubes: V. inertial effects. *Can. J. Chem. Engin.*, 44:181–193, 1966.

[136] A. Okagawa, R. G. Cox, and S. G. Mason. The kinetics of flowing dispersions. xii. some effects of nonuniform shear. *Journal of Colloid and Interface Science*, 71(1):11–17, 1979.

[137] J. Einarsson, A. Johansson, S. K. Mahato, Y. N. Mishra, J. R. Angilella, D. Hanstorp, and B. Mehlig. Periodic and aperiodic tumbling of microrods advected in a microchannel flow. *Acta Mechanica*, 224(10):2281–2289, 2013.

[138] E. J. Hinch and L. G. Leal. Rotation of small non-axisymmetric particles in a simple shear flow. *Journal of Fluid Mechanics*, 92:591–607, 6 1979.

[139] A. L. Yarin, O. Gottlieb, and I. V. Roisman. Chaotic rotation of triaxial ellipsoids in simple shear flow. *J. Fluid Mech.*, 340:83–100, 1997.

[140] J. Einarsson, F. Candelier, F. Lundell, J. R. Angilella, and B. Mehlig. Effect of weak fluid inertia upon jeffery orbits. *Phys. Rev. E*, 91:041002, Apr 2015.

[141] G. Gompper, T. Ihle, D. M. Kroll, and R. G. Winkler. *Multi-Particle Collision Dynamics: A Particle-Based Mesoscale Simulation Approach to the Hydrodynamics of Complex Fluids*, volume 221, pages 1–87. Springer, Berlin, Heidelberg, 2009.

[142] Raymond Kapral. *Multiparticle Collision Dynamics: Simulation of Complex Systems on Mesoscales*, pages 89–146. John Wiley & Sons, Inc., Hoboken, NJ, USA, 2008.

[143] Yongxiang Gao, Andrew Kaan Balin, Roel P. A. Dullens, Julia M. Yeomans, and Dirk G. A. L. Aarts. Thermal analog of gimbal lock in a colloidal ferromagnetic janus rod. *Phys. Rev. Lett.*, 115:248301, Dec 2015.

[144] F. García-Ochoa, V. E. Santos, J. A. Casas, and E. Gómez. Xanthan gum: production, recovery, and properties. *Biotechnology Advances*, 18(7):549–579, 2000.

[145] Ronald G. Larson. *The Structure and Rheology of Complex Fluids.* Oxford University press, New York, USA, 1999.

[146] Lucie Campagnolo, Milan Nikolić, Julien Perchoux, Yah Leng Lim, Karl Bertling, Karine Loubière, Laurent Prat, Aleksandar D. Rakić, and Thierry Bosch. Flow profile measurement in microchannel using the optical feedback interferometry sensing technique. *Microfluidics and Nanofluidics*, 14(1):113–119, 2013.

[147] Lichao Pan and Paulo E. Arratia. A high-shear, low reynolds number microfluidic rheometer. *Microfluidics and Nanofluidics*, 14(5):885–894, 2013.

[148] Malcolm M. Cross. Rheology of non-newtonian fluids: A new flow equation for pseudoplastic systems. *Journal of Colloid Science*, 20(5):417–437, 1965.

[149] Henk N. W. Lekkerkerker and Remco Tuinier. *Colloids and the Depletion Interaction.* Springer, Dordrecht, Netherlands, 2011.

List of publications

To date the following publications based upon work in this thesis have been submitted or are in preparation:

- Kira E. Klop, Chris L. Farmer, Roel P. A. Dullens and Dirk G. A. L. Aarts, (2015), *Direct calculation of distortion energies in colloidal liquid crystals from single-particle data*, Mol. Phys. 113 (17-18), 2693-2698, (Chapter 3)
- Kira E. Klop, Roel P. A. Dullens, M. Paul Lettinga, Sergei A. Egorov and Dirk G. A. L. Aarts, (2016), *Capillary nematization of colloidal rods in confinement*, submitted, (Chapter 4)
- Kira E. Klop, Andreas Zöttl, Roel P. A. Dullens, Julia M. Yeomans and Dirk G. A. L. Aarts, *Orientational behaviour of silica rods in a Poiseuille flow*, in preparation, (Chapter 5)
- Kira E. Klop, Andrew Kaan Balin, Yongxiang Gao, Roel P. A. Dullens, Julia M. Yeomans and Dirk G. A. L. Aarts, *Effects of a magnetic field on the behaviour of silica rods in a Poiseuille flow*, in preparation, (Chapter 6)

Other publications:

- Colin P. Reynolds, Kira E. Klop, François A. Lavergne, Sarah M. Morrow, Dirk G.A.L. Aarts, Roel P.A. Dullens (2015), *Deterministic Aggregation Kinetics of Superparamagnetic Colloidal Particles*, The Journal of Chemical Physics 143, 214903
- Julius W. J. de Folter, Eline M. Hutter, Sonja I. R. Castillo, Kira E. Klop, Albert P. Philipse, Willem K. Kegel (2014), *Particle Shape Anisotropy in Pickering Emulsions: Cubes and Peanuts*, Langmuir 30, 955-964

Acknowledgments

First and foremost, I would like to thank Dirk for all his guidance and support in the past years, and for giving me the opportunity to pursue this DPhil. I've really appreciated your relaxed style of supervising, and your enthusiasm when seeing experimental results has often motivated and encouraged me. You've been a great supervisor! I also want to thank both Roel and Julia for all the useful discussions we've had.Your input has been invaluable.

I would like to thank Oli and Min for helping me get started at the very beginning and teaching me all about microfluidics. A big thank you goes to Pavlik and Yongxiang for supplying me with the rods to do experiments with, and for all their advice. Pavlik's vast knowledge of colloidal rods has been particularly helpful. I would also like to express my thanks to Andreas and Andrew in the physics department, I've really enjoyed working with you both on the tumbling silica rods. Michael deserves credit for helping me out with some last-minute experiments at the very end, when I wasn't allowed in the lab myself.

Special thanks goes to Huzaifah for the many interesting lunch discussions, for always giving me a good excuse to solve Mathematica problems instead of writing and for all the cakes, chocolates and the peanut sauce. I'd also like to thank Huzaifah, Raam, Michael, Paola and Min for livening up the office over the years, and of course everyone else in the Aarts/Dullens groups for making the colloid group a great place to work and for all the tea-time breaks. Huzaifah and Raam; good luck with the writing up in the coming months, you're nearly there!

Finally, I would like to express my gratitude to my parents and in-laws for their endless support, without which this thesis would not have been possible, and to Radboud for all his encouragement and support throughout my DPhil. I could not have done it without you. Last but certainly not least, I want to thank Jasper for his unrestrained excitement and enthusiasm for just about anything new, which has been truly inspiring.